



TAMPEREEN TEKNILLINEN YLIOPISTO
TAMPERE UNIVERSITY OF TECHNOLOGY

EERO KOIVUSALO
EPITAXIAL III-V SEMICONDUCTOR NANOWIRES

Master of Science thesis

Examiners: D.Sc. Teemu Hakkarainen and D.Sc. Soile Suomalainen
Examiners and topic approved by
the Faculty Council of the Faculty of
Natural Sciences on 9th March 2016

ABSTRACT

EERO KOIVUSALO: Epitaxial III-V semiconductor nanowires

Tampere University of Technology

Master of Science Thesis, 82 pages

May 2016

Master of Science (Tech.) Degree Programme in Science and Engineering

Major: Engineering Physics

Examiners: Doctor of Science (Tech.) Teemu Hakkarainen and Doctor of Science (Tech.) Soile Suomalainen

Keywords: III-V semiconductors, GaAs, nanowires, molecular beam epitaxy, droplet epitaxy, photoluminescence, x-ray diffraction

Semiconductor nanowires (NWs) offer versatile possibilities among future electronic and photonic devices. This thesis contains a review of several NW growth methods and the properties of the NWs. The purpose of the practical part of this thesis is to present growth of self-catalyzed GaAs NWs on lithography-free oxide patterns with a strong emphasis on droplet epitaxy and analysis of the structural and optical properties of the NWs. Furthermore, growth of GaAs/AlGaAs/GaAs core-shell heterostructure NWs is presented along with a study of their photonic properties.

In terms of the epitaxial growth, focus is on the GaAs droplet epitaxy which is the initial step of the NW growth on lithography-free oxide patterns. Various different growth parameters and two different molecular beam epitaxy reactors were used in order to investigate their influence on the GaAs nanocrystal density and morphology. Unintentional Sb exposure was found to cause Si(111) surface roughening and repeatability problems in terms of the GaAs nanocrystal density.

High-resolution x-ray diffractometry was used to obtain reciprocal space maps of the self-catalyzed GaAs NWs grown on lithography-free oxide patterns formed by droplet epitaxy. Together with the micro-photoluminescence spectroscopy results they showed that the NWs consist mainly of ZB GaAs except for the WZ segments formed during the crystallization of the Ga catalyst droplets. The micro-photoluminescence also showed impurity related emission possibly due to substrate originated Si atoms.

Room temperature photoluminescence spectroscopy of the core-shell NWs showed the necessity of AlGaAs passivation as it increased the PL intensity from the NWs several orders of magnitude. Furthermore, thicknesses of the AlGaAs passivation shell and the GaAs cap protecting it from oxidizing were found to have a significant effect on sample aging. Micro-photoluminescence measurements conducted on a single GaAs/AlGaAs/GaAs core-shell NW showed longitudinal Fabry-Pérot modes. However, thicker NWs are required in order to obtain lasing.

A broad understanding was obtained concerning the characteristics of the NWs grown via self-catalyzed method on lithography-free oxide patterns. Simultaneously important experience was accumulated on the possibilities of the NW characterization methods at Optoelectronics Research Centre.

TIIVISTELMÄ

EERO KOIVUSALO: Epitaksiaaliset III-V puolijohdenanolangat

Tampereen teknillinen yliopisto

Diplomityö, 82 sivua

Toukokuu 2016

Teknis-luonnontieteellinen diplomi-insinöörin tutkinto-ohjelma

Pääaine: Teknillinen fysiikka

Tarkastaja: Tekniikan tohtori Teemu Hakkarainen, Tekniikan tohtori Soile Suomalainen

Avainsanat: III-V-puolijohteet, nanolangat, molekyyliisuihkuepitaksia, pisaraepitaksia, fotoluminesenssi, röntgendiffraktio

Puolijohdenanolangat tarjoavat monipuolisia mahdollisuuksia elektroniikan ja fotonikan kehityksessä. Tässä työssä esitellään useita nanolankojen valmistusmenetelmiä. Myös nanolankojen optisiin ominaisuuksiin perehdytään. Tämän työn tarkoituksena on kasvattaa epitaksiaalisia Ga-katalysoituja GaAs nanolankoja piisubstraatille ilman litografiaa valmistettuihin pioksidikuvioihin molekyyliisuihkuepitaksialla. Erityisesti pisaraepitaksiaa on kasvatusvaiheena painotettu nanolankojen kasvatusalustojen riittävyden varmistamiseksi. Nanolankojen tutkimus painottuu niiden rakenteellisten ja optisten ominaisuuksien karakterisointiin. Myös GaAs/AlGaAs/GaAs kuoriheterorakennanolanokojen fotonisia ominaisuuksia on tutkittu.

Pisaraepitaksialla kasvatettujen GaAs nanokristallien tiheyttä ja muotoa tutkittiin käyttämällä kasvatuksissa useita eri kasvatusparametreja sekä kahta molekyyliisuihkuepitaksiareaktoria. Tahattoman antimonialtistuksen todettiin aiheuttava Si(111)-pinnan karhentumista sekä toistettavuusongelmia nanokristallien tiheydessä.

Ga-katalysoitujen, ilman litografiaa valmistettuihin oksidikuvioihin kasvatettujen GaAs nanolankojen rakenteellisiä ominaisuuksia tutkittiin käänteishilakartoilla, jotka mitattiin käyttäen korkean erotuskyvyn röntgendiffraktiota. Yhdessä mikrofotoluminesenssimittausten kanssa käänteishilakartat näyttivät nanolankojen koostuvan sinkkivälkerakenteesta lukuun ottamatta katalyyttipisaroiden kiteytyksessä syntyntä wurtsiittirakennetta sisältävää kärkeään. Mikrofotoluminesenssimittauksissa havaittiin myös epäpuhtausemissio, joka mahdollisesti aiheutuu alustakiteestä peräisin olevasta Si epäpuhtaudesta.

Nanolankojen AlGaAs pintatilapassivoinnin hyödyllisyys osoitettiin kuoriheterorakennanolanokojen huoneen lämpötilan fotoluminesenssimittauksilla. AlGaAs-passivointikuoren ja sen oksidoitumista estävän GaAs-kuoren havaittiin vaikuttavan näytteiden ikääntymiseen huomattavasti. Lisäksi yksittäiseen kuoriheterorakennanolanokaan saatiin luotua Fabry-Pérot moodeja matalan lämpötilan mikrofotoluminesenssimittauksissa. Laseroitukynnyksen saavuttamiseksi tarvittaisiin kuitenkin paksumpia nanolankoja.

Ilman litografiaa valmistettuihin oksidikuvioihin kasvatettujen Ga-katalysoitujen nanolankojen rakenteellisista ja optisista ominaisuuksista saatiin työssä selkeä kuva. Samanaikaisesti saatiin tärkeää ja laajaa kokemusta nanolangoille sopivista karakterisointimenetelmistä Optoelektroniikan tutkimuskeskuksessa.

PREFACE

This work was conducted at the Optoelectronics Research Centre (ORC) which is a part of the Faculty of Science and Environmental Engineering of Tampere University of Technology.

This thesis was reviewed by D.Sc Soile Suomalainen and D.Sc Teemu Hakkarainen, who also supervised this work. I owe him great gratitude of many advices concerning this work. I also thank him for growing various nanowire samples before my time at ORC. These samples were essential for characterization performed in this work. I would also like to express my gratitude to D.Sc Pekka Savolainen, the director of ORC and Prof. Mircea Guina, the leader of the semiconductor technology group at ORC, for providing me the great opportunity to work in this fine environment.

I would also like to thank MSc Riku Koskinen for teaching me how to handle our beloved molecular beam epitaxy reactor, SS10-2, during her up- and down-time.

Furthermore, I would like to thank my lovely wife Laura for all her support and the linguistic advices she has given to me concerning this work. I also thank all my dear friends who have provided me the opportunity to occasionally be distracted from pondering this work and to return to the writing process with renewed perspective.

Tampere, 23.5.2016

Eero Koivusalo

CONTENTS

1.	INTRODUCTION	1
2.	III-V SEMICONDUCTOR NANOWIRES	3
2.1	III-V semiconductors and epitaxial growth.....	3
2.1.1	Crystal structure and defects	3
2.1.2	Band gap	5
2.1.3	Epitaxial growth.....	8
2.2	Nanowire fabrication techniques.....	10
2.2.1	Molecular beam epitaxy.....	10
2.2.2	Metal organic vapor phase epitaxy	11
2.2.3	Other bottom-up methods	12
2.2.4	Top-down methods	15
2.3	Nanowire growth modes	15
2.3.1	Vapor-liquid-solid growth.....	15
2.3.2	Vapor-solid-solid growth	17
2.3.3	Self-seeded growth.....	17
2.3.4	Catalyst free growth	19
2.3.5	Solution-liquid-solid growth.....	20
2.4	Effect of substrate and oxide layer on nanowire growth.....	21
2.4.1	Random pinholes in oxide layer on substrate	21
2.4.2	Selective area epitaxy.....	22
2.4.3	Droplet epitaxy based methods	23
2.4.4	Growth in lithography-free patterns in oxide layer.....	24
2.5	Nanowire heterostructures and doping.....	26
2.6	Optical properties of nanowires	28
2.6.1	Carrier recombination and lifetime	28
2.6.2	Absorption and cavity properties in nanowires.....	30
3.	METHODS	32
3.1	MBE growth.....	32
3.1.1	Droplet epitaxy of GaAs nanocrystals on Si.....	32
3.1.2	Growth of GaAs nanowires on Si	33
3.1.3	Growth of GaAs/AlGaAs heterostructure nanowires	34
3.2	Characterization	36
3.2.1	Atomic force microscopy.....	36
3.2.2	Scanning electron microscopy	38
3.2.3	High resolution x-ray diffraction	39
3.2.4	Photoluminescence spectroscopy.....	43
4.	RESULTS AND DISCUSSION	44
4.1	GaAs nanocrystals.....	44
4.2	Nanowires.....	52

4.2.1	X-ray diffraction	54
4.2.2	Room temperature photoluminescence	58
4.2.3	Micro-photoluminescence of bare GaAs nanowires	59
4.2.4	Micro-photoluminescence of GaAs/AlGaAs core-shell nanowires	64
5.	CONCLUSIONS	69
	REFERENCES	71

LIST OF ABBREVIATIONS AND SYMBOLS

AFM	Atomic force microscope
CBE	Chemical beam epitaxy
MBE	Molecular beam epitaxy
MOVPE	Metal organic vapor phase epitaxy
NW	Nanowire
PL	Photoluminescence
μ -PL	Micro-photoluminescence
CCD	Charge-coupled device
ORC	Optoelectronics Research Centre
RHEED	Reflection high-energy electron diffraction
RT-PL	Room temperature photoluminescence
SEM	Scanning electron microscope
TEM	Transmission electron microscope
VLS	Vapor-liquid-solid
WZ	Wurtzite crystalline structure
ZB	Zinc blende crystalline structure
UHV	Ultra-high vacuum
BEP	Beam equivalent pressure
CMOS	Complementary metal oxide semiconductor
VS	Vapor-solid
SLS	Solution-liquid-solid
SAE	Selective area epitaxy
XRD	X-ray diffraction
HR-XRD	High resolution x-ray diffraction
RMS	Root mean square
ML	Monolayer
a	Lattice constant
c	Second lattice constant in hexagonal structures
E_g	Band gap energy
T	Temperature
$a.u.$	Arbitrary unit
x	Composition of an element in an alloy
n_{group}	Group refractive index
$\Delta\nu_{FSR}$	Free spectral range
L	Length
L_{OP}	Optical length
λ_k	Wavelength of mode k
k	Index of a mode
Q_x	X-ray momentum transfer in x-direction
Q_y	X-ray momentum transfer in y-direction
d_{hkl}	Distance between consecutive lattice planes
(hkl)	Indices of a lattice plane
ω	Incident angle of x-rays
θ	Angle of diffracted x-rays
E_a	Activation energy
k_b	Boltzmann constant

1. INTRODUCTION

III-V semiconductor materials are widely utilized in the field of optoelectronics and photonics. They are used to manufacture high quality lasers, LEDs and solar cells, because they offer a possibility to tune the wavelength ranges of these devices by adjusting material compositions. These applications require excellent crystalline quality, which is obtained via epitaxial material growth where the overgrown material copies the crystalline structure of the substrate. Molecular beam epitaxy (MBE) is a technique, which enables the growth of the III-V materials with highest possible material and crystalline phase purity and enables tuning the elemental compositions and layer thicknesses with monolayer (ML) precision.

Complementary metal oxide semiconductors (CMOS) which are used in microchips and typical solar cells are based on silicon. Both of these components would benefit from integration of III-V semiconductors as electrically pumped emitters could be integrated on Si microchips for inter-chip communication [1; 2] and two-junction solar cells with extremely high conversion efficiency could be obtained by growing NWs on top of Si solar cell [3]. Si has also better heat transfer properties compared to typical III-V semiconductors, which could be utilized by integrating III-V devices on Si substrates. However, there is a lattice and thermal mismatch between silicon and the most typical III-V semiconductors, such as gallium arsenide (GaAs). This has been a major obstacle in direct integration of the III-V materials on Si. Nanowires (NW), which have diameters ranging from tens to few hundred nanometers, overcome this issue by relaxing the strain induced by the lattice mismatch in the first atomic layers of the structure. Several functioning NW devices have already been demonstrated: lasers [1; 2; 4], solar cells [5; 91] and LEDs [6; 7].

In this thesis, the NWs are first presented in a literature review of the NW fabrication techniques and methods. Also their structural and optical properties are presented. The emphasis is on MBE and III-V materials, especially GaAs. The primary objective of this thesis was to grow GaAs NWs on lithography-free patterns in silicon oxide layer [8] and characterize their structural and optical properties. Regarding epitaxial growth, a strong emphasis was put on droplet epitaxy, the first step of the NW growth on lithography-free oxide patterns. It is an important step of the growth process as it produces the templates used for the NW growth. Considering the NWs, the focus of this work is on their characterization. Their structural properties are studied via high-resolution X-ray diffractometry (HR-XRD) of bare GaAs NWs which are also used in optical characterization conducted as low temperature micro-photoluminescence spectroscopy (μ -PL)

measurements. Photonic properties of the GaAs/AlGaAs/GaAs core-shell NWs are also studied via μ -PL in order to obtain lasing.

This thesis consists of five chapters. In Chapter 2, the basics of III-V semiconductors and epitaxial growth are presented followed by a review of NW fabrication techniques, growth methods and the effect of substrate surface on the NW growth. Also the NW heterostructures and their optical properties are presented. The next chapter presents the methods used in this work. First, the droplet epitaxy procedure and the growth of bare and core-shell NWs are presented. The MBE section is followed by introduction to the characterization methods, atomic force microscopy (AFM), scanning electron microscopy (SEM), HR-XRD and photoluminescence spectroscopy. Chapter 4 presents the results of this work and their interpretation. In the last chapter the conclusions based on the results and future prospects of NW research at Optoelectronics Research Centre (ORC) are discussed.

2. III-V SEMICONDUCTOR NANOWIRES

The first sub-chapter of this chapter presents the general properties of III-V semiconductors with a motivation for NW growth. In the second sub-chapter techniques for NW fabrication are presented and in the third their growth modes. The fourth sub-chapter focuses on the substrate surface properties affecting NW growth. The fifth sub-chapter describes NW heterostructures and their growth. The last sub-chapter presents the optical properties of NWs. All chapters are written emphasis on III-V NWs even though some of the growth techniques and modes are also applicable on group-IV semiconductor or metal oxide NWs.

2.1 III-V semiconductors and epitaxial growth

III-V semiconductors are compound semiconductors containing equal amounts of group III and group V elements. They have excellent electrical and optical properties. Hence, they have many applications which often require good crystalline quality obtained by epitaxial fabrication techniques. This sub-chapter presents the basics of the crystalline structure and the band structure, which determines the electrical and optical properties of materials. Also the concept of epitaxial growth of III-V semiconductors is introduced.

2.1.1 Crystal structure and defects

All semiconductors and metals have a regular crystalline structure when they are in solid state. A unit cell is the basis of the crystalline structure and by repeating numerous unit cells the crystalline structure is formed for a single-crystalline material. Unit cells have atoms at least at their corners which is the case for simple cubic structures like NaCl. Hence, the size of the unit cell, called lattice constant describes the distance between consecutive atom layers. For some structures there are more than just two atomic layers in one unit cell. Two examples of typical unit cells are presented in Figure 1. [9]

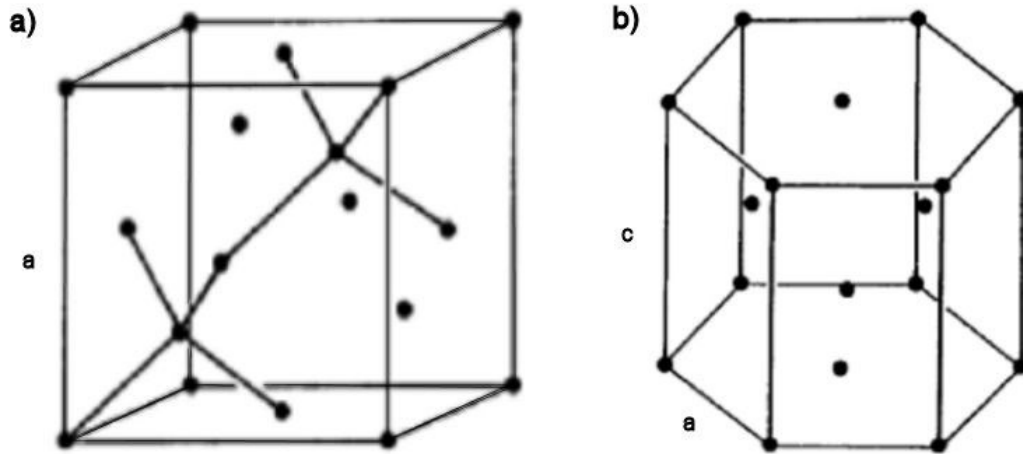


Figure 1. Diamond cubic a) and hexagonal close packed (HCP) b) unit cells presented with added lattice constants a and c . [9]

In compound semiconductors the value of the lattice constant obeys Vegard's law originally presented in [10]. Vegard's law is a linear equation of the elemental composition. For example the Vegard's law for $\text{Al}_x\text{Ga}_{1-x}\text{As}$, widely used III-V semiconductor, is

$$a = 5.6533 + 0.0078 \cdot x \text{ \AA}, \quad (1)$$

where a is the lattice constant and x is the fraction of aluminum in the material. [11]

Silicon and other elemental semiconductors have cubic diamond crystalline structure presented in Figure 1, whereas III-V semiconductors (disregarding III-nitrogen compounds such as GaN) have typically cubic zinc blende (ZB) structure. ZB structure is similar to diamond cubic but every atom is bonded to four atoms of the opposite type. [11] In (111) direction, which is the growth direction of NWs, the ZB structure may be presented as a sequence of three identical atomic bilayers named A, B and C. These bilayers are separated by their location in relation to other layers. In ZB these layers are ordered so that each layer is surrounded by two different layers, for instance ABCABC. However, when III-V semiconductors form NWs also hexagonal wurtzite (WZ) crystalline structure may exist. WZ structure is formed from similar bilayers as ZB structure but only two layers alternate, for instance ABABAB. [12] Both of these structures are presented in Figure 2.

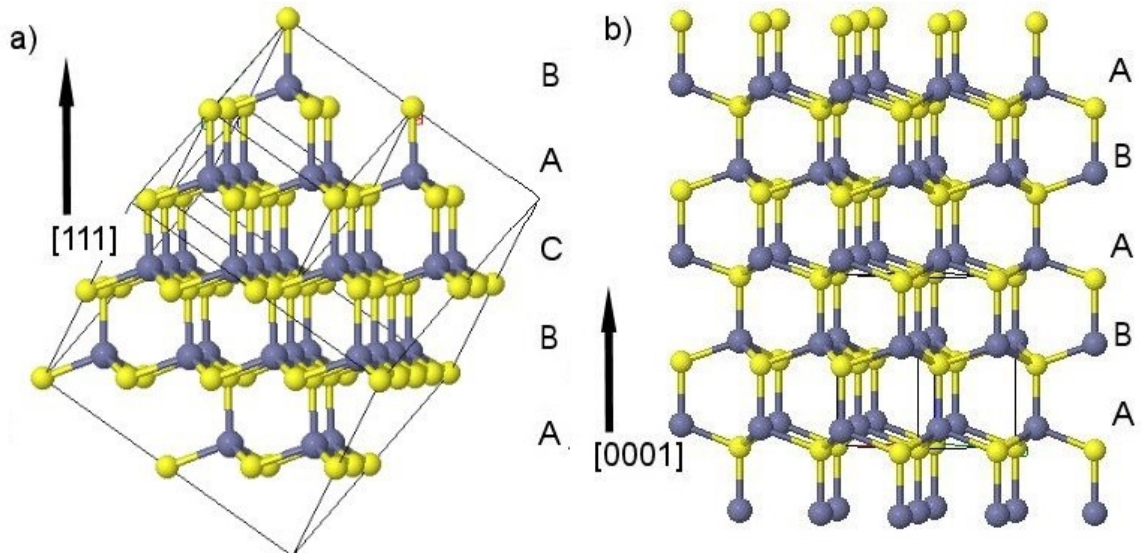


Figure 2. Zinc blende a) and wurtzite b) structures are presented with atomic bilayers A, B and C and arrows indicating NW growth directions. The smaller cube in a) defines the unit cell of zinc blende structure. [13]

The crystalline structure is not always perfect which is seen as dislocations. Dislocations are displacements in crystals. An excess or missing partial atomic plane forms an edge dislocation. The atomic planes may also partially slip relative to one another forming screw dislocations. [9] However, dislocations in real lattices are typically much more complicated and may consist of, for example, slip and edge partial dislocations [14]. Dislocations are often related to strain induced by lattice mismatch. Lattice mismatch is caused by a material interface within the crystalline structure where the materials on different sides of the interface have different lattice constants. This is typical situation for thin film growth where different material layers alternate in order to form functional structures. Strain in heterostructures varies also as a function temperature because different materials have different coefficients of heat expansion. This is called thermal mismatch. [15] Another lattice imperfection which is important when discussing NWs, is alternating WZ and ZB segments. An atomic layer thick WZ segment in ZB NW, and vice versa, is called a stacking fault. An example of a stacking fault in ZB structure is stacking sequence ABCABABC. [12] The stacking faults may also cause rotational twinning which is seen as 180° rotation around the NW growth axis. It creates a stacking sequence equivalent to ABCABCBACBA. This kind of changes in stacking sequence can be distinguished in transmission electron microscope (TEM) images used to study crystalline structure of NWs. [16]

2.1.2 Band gap

In the field of optoelectronics strong light-matter interaction is essential. For instance solar cells must absorb strongly and for lasing and LEDs stimulated and spontaneous emission is required. In order to obtain interaction with light, the carriers, namely electrons and holes, must be able to change their energy states rapidly. The carrier transi-

tions between the energy states are caused by either absorbing or emitting a photon. Such transitions in semiconductors occur between two separate energy bands, valence and conduction band. The energy separation between the valence and the conduction bands is called band gap. The electron states of the atoms form these energy bands as the lattice structure of the solid builds up. For interaction with light it is beneficial that the band gap is direct. Direct band gap means that the highest energy of valence band and lowest energy of conduction band are located in the same point in k-space. This means that the carrier conserves its momentum in the transition over the band gap. Silicon and germanium which are main building blocks of semiconductor industry as cheap elements suitable for microprocessors have indirect band gap. III-V compound semiconductors are alloys formed out of elemental group III metal namely aluminum, gallium or indium and of group V element such as nitrogen, phosphorous, arsenic, antimony or bismuth. These materials have direct band gaps in wide energy range. The band structure of III-V semiconductors may be engineered by combining three or more elements forming compounds like AlGaAs. Hence, their usage in optoelectronics is essential. The band gap energy, unlike the lattice constant, is nonlinear as a function of elemental composition. Typically simple quadratic relation is used for ternary compound $A_xB_{1-x}V$

$$E_g(A_xB_{1-x}) = (1-x)E_g(A) + xE_g(B) - x(1-x)C, \quad (2)$$

where E_g is the band gap energy, x is the fraction of element A and C is a bowing parameter. [17] Graphical illustration of relation between lattice constant and band gap is presented in Figure 3.

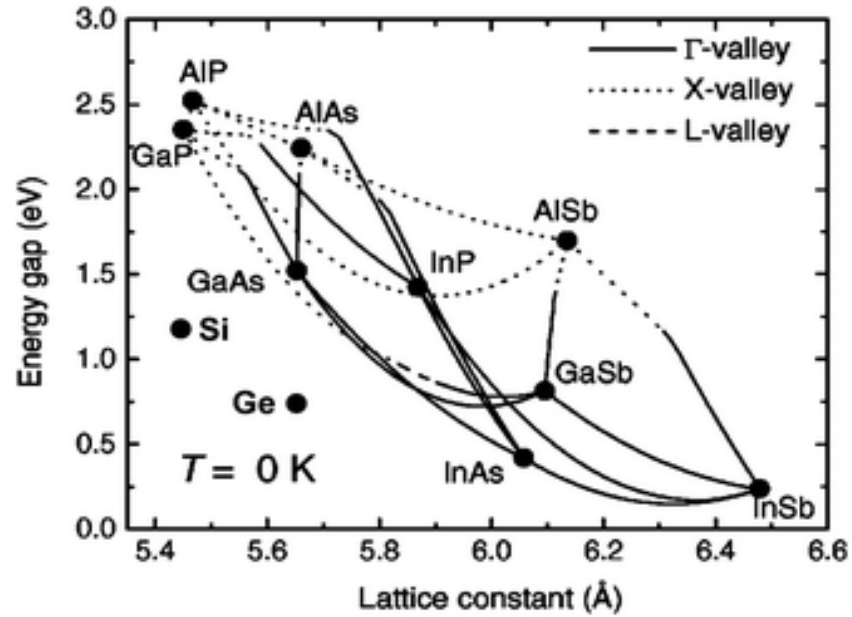


Figure 3. Band gap of III-V semiconductors is presented as a function of composition and lattice constant. Γ -valley marked with solid line represents direct band gap. [18]

Intentional incorporation of impurity atoms, for example from groups II, IV or VI, in the III-V lattice is called doping. Doping creates additional states in the band gap near the conductivity band (n-type doping) or the valence band (p-type doping). N-type dopants are called donors and p-type dopants are known as acceptors. In room temperature the thermal energy kT of electrons is adequate to excite them from donor levels to conduction band or from valence band to acceptor levels. Hence, free electrons (n-type) or holes (p-type) are created and conductivity of the semiconductor increases.

Doping is most commonly exploited by creating a p-n junction which is a doping interface where other side is p- and other n-type. Energy diagrams of a p-n junction under zero bias and a forward bias are presented in Figure 4. In zero bias excess electrons in p-type side (minor carriers) diffuse to the n-type side leaving behind a positive net charge. Holes in the n-side of the junction behave similarly creating a net negative charge on the n-side of the junction. These net charges repel the majority carriers in each side of the junction creating a depletion region which prevents diffusion of the majority carrier across the junction. Depletion region is presented by W_D in Figure 4 a). In forward bias, the p-side of the junction is connected to the positive terminal decreasing the potential barrier and enabling the current flow. In case of direct band gap material this can be exploited by forming light emitting diodes (LEDs) or diode lasers. The electric current flowing through the junction creates a population of minority carriers in each side of the junction. These minority carriers then recombine radiatively emitting photons within their diffusion lengths L_n and L_p in Figure 4 b). [19] An opposite effect occurs in solar cells where photons excite carriers on both sides of the p-n junction and the p-n junction separates the electron-hole pair. When the p- and n-sides of the cell are connected to an electric circuit, electric current is obtained. [20] However, to increase emission efficiency, it is beneficial to bind the carriers in an area smaller than the diffusion length of the carriers because the recombination rate is dependent on the carrier concentrations. This is obtained by forming a well of a smaller band gap material in the middle of the p-n junction to create a heterojunction presented in Figure 4 c). When this well is narrow enough to cause carrier quantum confinement, it is referred to as a quantum well and the band structure is altered even further as the possible states for carriers are quantized. [19]

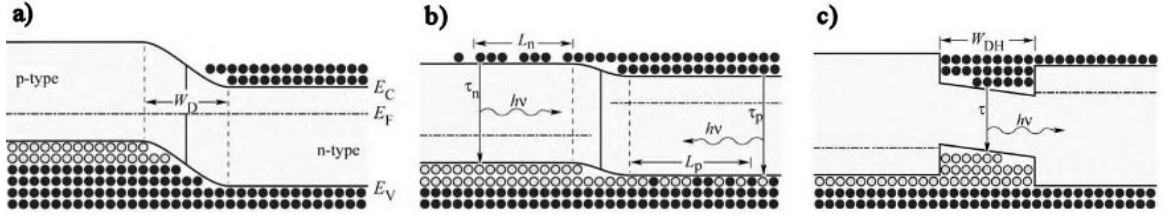


Figure 4. An energy diagram of a pn-junction is presented with a zero bias in a) and a forward bias in b). The solid circles are electrons and open circles are holes. In b) carriers recombine radiatively within their diffusion lengths L_n and L_p . In c) a p-n heterojunction under forward bias binds the carriers into a narrow well where they recombine. [19]

Doping also affects the value of the band gap as the intrinsic bands are modified. However, the intrinsic band is not affected if the dopant concentration is adequately low. As the doping density increases, the intrinsic band gap changes so that the emission linewidth obtained from radiative carrier recombination is initially broadened and with even higher doping levels it is reduced. [21; 22]

Also temperature affects the value of the band gap. The band gap energy is reduced as temperature increases. The band gap energy E_g follows the empirical Varshni function

$$E_g = E(0) - \alpha \cdot \frac{T^2}{T + \beta} \text{ eV}, \quad (3)$$

where $E(0)$ is the band gap energy in 0 K, T is the temperature and α and β are constants. [17]

2.1.3 Epitaxial growth

The III-V materials are epitaxially grown on substrates with high crystalline quality. The growth conditions are such that the atoms adsorbed on the substrate surface have enough thermal energy to diffuse to an energetically favorable location. In typical epitaxial thin film or bulk material growth the deposited material copies the crystalline structure of the underlying material. This kind of relation between the substrate and the deposited material is termed epitaxial. Also, the deposited material is referred to as the epitaxial material. In a heteroepitaxial case, where the substrate and the epitaxial material are different, the lattice constants may be mismatched, as presented in Figure 5. In order to copy the crystalline structure, the epitaxial material must build up so that it has laterally equal lattice constant as the substrate. The adaption of the lattice constant induces strain in the lattice. Strained epitaxial growth and strain relaxation via dislocation are presented in Figure 2 a)-c).

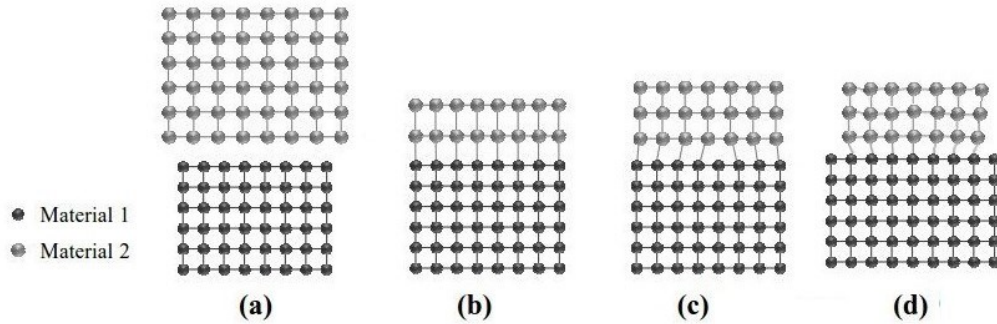


Figure 5. Lattice mismatched epitaxial growth with two separate lattices having different lattice constants a) may lead to strained epitaxial layers in case of small lattice mismatch or thin layers b). In c) the strain is relaxed via dislocation. Lateral strain relaxation can be obtained in thin NW structure without dislocations (d). Modified from [81] with permission of the author.

The lattice mismatch between Si and GaAs is 4%. [11] This means that no single crystalline bulk structure of GaAs can be epitaxially grown on Si without the structure relaxation via dislocations. Dislocations quench the optical properties of the material and, hence, make the relaxed crystalline structure useless for most optoelectronic applications. In epitaxial III-V semiconductor structures the substrate is the most material consuming part. Therefore, it would significantly reduce the cost per device if III-V compounds could be integrated on relatively cheap Si substrates. Also in application point-of-view, integrating emitters on complementary metal oxide semiconductor (CMOS) microcircuits or silicon-on-oxide (SOI) photonics platform is extremely tempting. The problem of lattice mismatch may be solved by growing GaAs, or other III-V semiconductors, in a one-dimensional manner forming NWs. [23] The NW structure allows the growth without dislocations as the strain is relaxed at the NW sidewalls. Strain relaxation at NW sidewalls is presented in Figure 5 d). For example a GaAs NW with radius of 30 nm and infinite length can be grown without any plastic strain relaxation via misfit dislocations in the lattice structure. [24] However, if the NW radius is increased above this critical value, relaxation occurs but it is still reduced in the first layers of the NW. This enables the growth of III-V NWs with typical diameters of about 100 nm on Si substrates. [23] Lateral strain relaxation and dislocations reduced to first atomic layers of NW redefine epitaxial relation. The NWs are epitaxial if the substrate facet determines the orientation of the crystal structure even though the crystal structure is not copied. For example, NWs with hexagonal WZ structure on Si with cubic diamond structure are epitaxial if the substrate determines their growth direction. Hence, vertical III-V NWs are epitaxial. Also tilted NWs can be epitaxial if the substrate crystal orientation determines their direction. [25]

2.2 Nanowire fabrication techniques

Techniques for growing NWs are categorized to bottom-up and top-down methods [26]. Bottom-up techniques are based on growing the NWs by adding material on the substrate. The material for the NWs is added either in the form of vapor or solution. Vapor-phase techniques typically used in NW growth are Molecular Beam Epitaxy (MBE) and Metal Organic Vapor Phase Epitaxy (MOVPE). Other typical bottom-up methods are solution based methods.[27] Top-down techniques are either lithography based techniques such as optical-, electron beam- and other novel lithography techniques [26], or etching [28]. This chapter discusses the above mentioned NW fabrication techniques.

2.2.1 Molecular beam epitaxy

Molecular beam epitaxy is a physical growth technique well suited for manufacturing complex epitaxial semiconductor structures. MBE growth takes place under an ultra-high vacuum (UHV) environment where the pressure can vary from 10^{-10} mbar, which is a typical value for an empty growth chamber, to 10^{-6} mbar, which is a value that pressure may reach during the growth process. UHV environment minimizes the amount of impurities in the samples and enables the material deposition in the form of elemental beams. This is enabled by increasing the mean free path of the atoms to tens of meters up to kilometers in the operating pressures. Material deposition in the form of molecular beams in vacuum enables growing extremely sharp, atomic layer thick interfaces. Also modifying the doping concentrations continuously or abruptly is possible. Group III materials are introduced from heated crucibles called effusion cells. The temperature of the effusion cells determines the amount of material in the flux, which can be turned on and off with mechanical shutters. Crackers with needle valves are used for group V materials such as As, Sb and P. With low cracker temperatures quaternary molecules are introduced, whereas a hotter cracker breaks them into dimers such as As_2 . Plasma sources are used for N, whereas Bi is provided from similar effusion cells as group III materials. [15; 29]

The main growth parameters of the MBE growth process are substrate temperature and material fluxes. The former affects the diffusion lengths of the atoms on the substrate surface and the probability of atoms to adsorb on to the substrate or to evaporate. The latter is controlled by changing the temperatures of the effusion cells and openings of the cracker needle valves. Material fluxes determine the growth rate and the composition of ternary and quaternary alloys. Normal two-dimensional growth occurs under excess group V material flux as the amount of group III material determines the growth rate. However, growing nanocrystals and NWs requires more precise control of the III/V flux ratio. For example in the case of Ga catalyzed GaAs NWs, the growth rate is determined by the As flux. [15; 29]

In MBE, the units for measuring the growth rate and the amount of material introduced on the substrate are rather diverse. The material flux is measured with an ionization gauge in the growth chamber and hence its values are given in nanoamperes (nA) to the reactor operator. However, the true two-dimensional growth rate can be given in units of micrometers per hour ($\mu\text{m/h}$), nanometers per minute (nm/min), nanometers per second (nm/s) or monolayers per second (ML/s). All these units describe thickness of the grown layer within a certain period of time. Growth rate in ML/s can be determined directly from reflection high-energy electron diffraction (RHEED) intensity oscillations. [15] It is an especially convenient unit when the amount of deposited material is small. For instance, in droplet epitaxy the amount of provided group III element can be less than one ML. In these situations ML refers to amount of group III element in order to grow one 2D-layer of III-V compound. [30] When changing the unit system from MLs to thicknesses the amount of MLs per crystalline unit cell must be taken to account. For example the lattice constant of ZB GaAs is 5.65325 \AA [11] which is the thickness of two MLs stacked in [100] directions. In other words, one GaAs ML is the spacing of (200) crystal planes. It is also noteworthy that ML thickness is different for other crystal directions. For example [111] is the growth direction of ZB NWs but the amount of deposited material is still determined based on MLs in [100] direction as the growth rates are typically calibrated based on growth on (100) surface. [31] The deposition rate of the group V element is often determined by beam equivalent pressure (BEP). Unit for BEP can be any unit of pressure but Torr is typically used in literature. BEPs vary from reactor to another since they are proportional to flux meter readings that are not typically calibrated for group V fluxes. Hence, the BEP cannot be used to describe the actual flux of group V atoms or molecules per unit of time unless the flux measurement is carefully calibrated. Typically V/III ratio of the BEPs is used to give information of the group V flux. [29]

2.2.2 Metal organic vapor phase epitaxy

In MOVPE vapor phase organic and hydride chemical precursors mixed with hydrogen as a carrier gas deliver the semiconductor reactants to the substrate. Unlike MBE, it is a chemical deposition technique. MOVPE is also referred to as metal organic chemical vapor deposition (MOCVD) or organometallic chemical vapor deposition (OMCVD) although in detail MOCVD and OMCVD do not require epitaxial relationship between the substrate and the deposited material. The MOVPE process occurs in a reaction chamber where the substrate is heated to the desired growth temperature. Then, the chemical precursors mixed with an inert carrier gas are allowed to flow to the reaction chamber in pre-ordered concentrations. The heat from the reaction frees the metal and semiconductor atoms from the precursor molecules. The atoms adsorb to the substrate surface leading to more complicated surface kinetics than in MBE because gas phase reactions [32] and viscous gas flow [29] take place on the substrate surface. Traditionally, MOVPE is preferred over MBE in industrial production of many III-V semiconduc-

tor devices due to faster growth rates and UHV-free growth conditions whereas MBE is used when high purity and accuracy interfaces are needed. [33] Even though MBE technique has significantly increased its throughput capability, the growth rates have not increased and hence MOVPE is generally still the leading manufacturing technique of thicker epitaxial structures whereas MBE has otherwise established its position in large scale manufacturing. [34] From NW point of view, there are some indications that MBE grown self-seeded GaAs NWs with an AlGaAs passivation layer have longer carrier lifetimes and hence better optical properties than MOVPE grown NWs. [35; 36] However, the results are not completely comparable because passivating shell thicknesses in MOVPE and MBE grown wires differ which may affect the carrier lifetimes in the NWs. [35; 36] Similar results have been found for Au catalyzed NWs. [37]

2.2.3 Other bottom-up methods

There are various solution based methods for growing NWs. NWs may be grown straight in a flask without a substrate [38], with a substrate [39], in a reactor on a substrate [40] or in microfluidic chips on substrates [41]. Of these techniques, the flask based method is presented as it generalizes the properties of solution based methods without excessive complexity. Figure 6 illustrates solution based NW fabrication techniques and NWs produced by them. Solution based NWs are also referred as quantum wires as they are typically very thin. Various materials including silicon [38], II-VI compounds such as CdSe [39] and III-V materials [42] can be grown by solution based methods.

Chemical beam epitaxy (CBE) combines techniques used in MBE and MOVPE. CBE reactors have similar vacuum conditions to MBE but the material is provided in the form of chemical precursors similar to the ones used in MOVPE. CBE is conducted in ordinary MBE reactors with gas sources. [43] Systems with MBE effusion cells for group III elements and gas sources with crackers for group V elements are referred as gas source MBE [44]. Some of the precursor gases are cracked to elemental beams before introducing them into the growth chamber. [29] Earliest Au induced GaAs NWs were position controlled and grown by CBE. [45] The NW growth rates in CBE are quite similar to MBE. For example CBE allows growth of NWs composed of AlAs, which typically can be used only as a shell layer in heterostructure NWs when grown by other methods. [43].

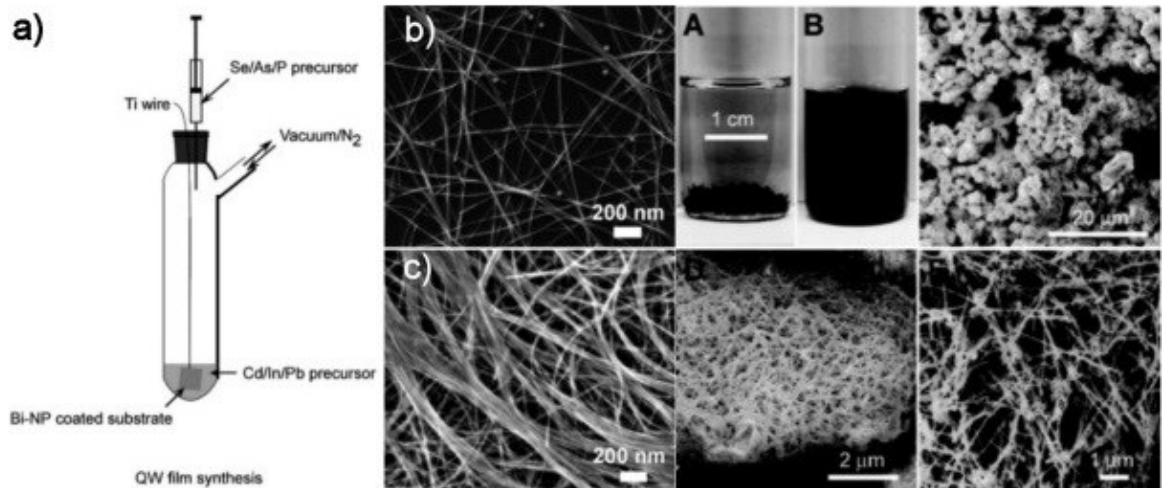


Figure 6. Flask based technique for CdSe quantum wire growth on a substrate is presented in a). Corresponding quantum wires grown with different catalyst particle concentration are presented in b) and c). [39] A to E present silicon NWs grown in a flask without a substrate [38].

Aerosol assisted chemical vapor deposition (AACVD) is a MOVPE-related technique where precursors are provided to the substrate in the form of aerosol particles. The material deposition occurs in low to atmospheric pressure or even in open atmosphere. A review on AACVD technique can be found in [46]. By this technique metal oxide nanoneedles have been directly integrated on gas sensors. These nanoneedles are not epitaxial as their growth direction is at its best quasi-aligned as presented in Figure 7. They have also very broad width and length distributions. [47]

Hydride vapor phase epitaxy (HVPE) is a MOVPE-related technique which uses hydride precursors. It is used in the growth of III-V NWs with extremely fast, over 100 $\mu\text{m}/\text{h}$ growth rates. Exceptionally long ($>50 \mu\text{m}$) NWs can be grown with this technique. [48] Also extreme phase purity and narrow geometry can be obtained for zincblende GaAs. However, these wires are not completely straight even though the bending may be caused by charge accumulation during SEM imaging. [49] HVPE of NWs requires usage of catalyst droplets [48]. The resulting wires are presented in Figure 7.

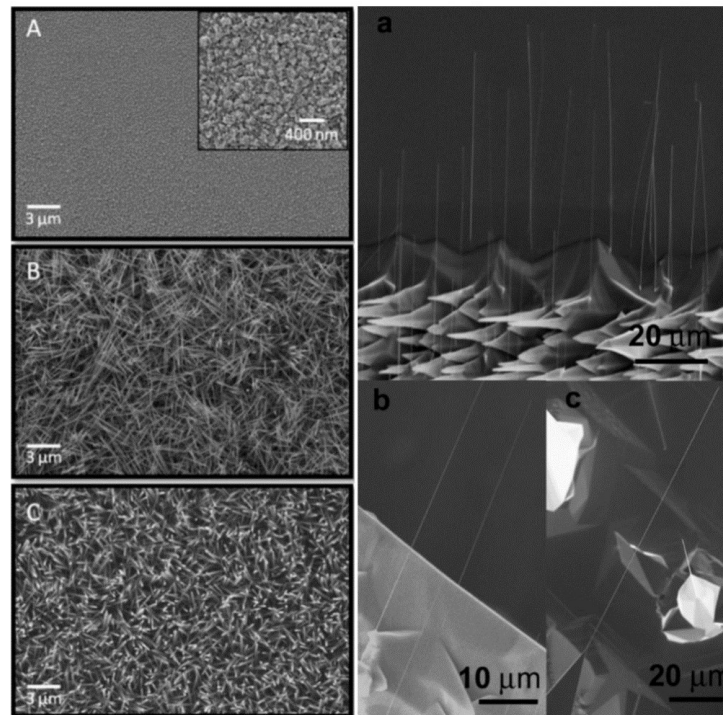


Figure 7. AACVD grown tungsten oxide NWs on silicon oxide layer on gas detector are presented in A to C [47]. Extremely long and thin GaAs NWs grown on GaAs(100) substrate by HVPE are presented in a to c. The NWs are located on top of oriented scales formed in the beginning of the NW growth. [50]

Aerotaxy is a NW growth method where NWs grow in Au-catalyzed mode as Au nanoparticles in aerosol phase flow through a gas stream with precursor molecules. The growth rates are 20 to 1000 times faster than for NW growth on single crystalline substrates and the growth is continuous instead of batchwise. Hence aerotaxy as well as solution based methods are potential ways to manufacture large amounts of NWs when epitaxial relation between the NWs and the substrate is not required. [51] The principle of the aerotaxy method and SEM images of aerotaxy-grown NWs are presented in Figure 8.

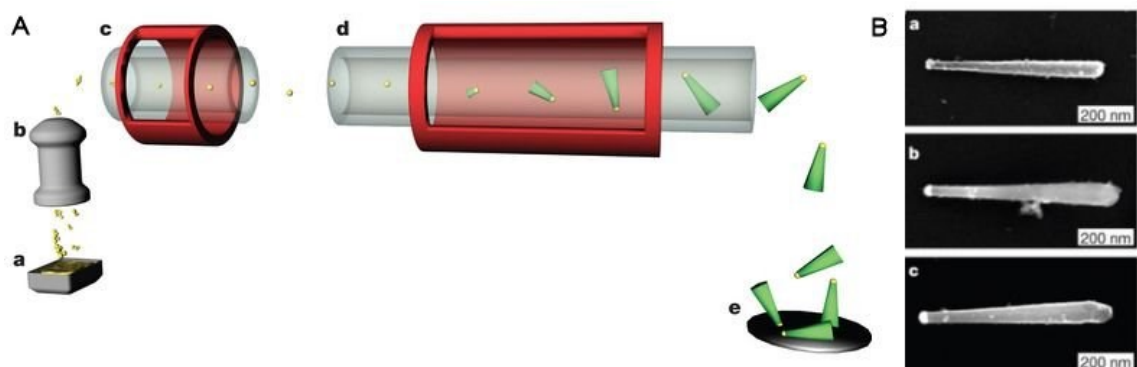


Figure 8. Principle of aerotaxy growth method A and strongly tapered NWs grown with different sized Au nanoparticles B [51].

2.2.4 Top-down methods

NWs may also be produced by top-down techniques, which are mainly based on lithography. Traditional optical lithography is diffraction limited so scaling down the feature size is problematic. This problem is solved by using electron beam lithography and other techniques, such as nanoimprint, scanning probe and ion beam lithography. These are preferential techniques in manufacturing horizontal NWs on substrate surface but may also be used in manufacturing vertical NWs. The NW material is typically silicon. [26] Vertical top-down NWs can also be formed by metal catalyst etching. This can be obtained by producing catalyst nanoparticles for example silver on Si substrate and immersing the substrate to a solution that etches the material under the catalyst nanoparticles but leaves the catalyst free surfaces intact. This method might be suitable for manufacturing silicon antireflection coatings on silicon solar cells. [28] Since the top-down methods for vertical NWs require a bulk structure as a starting point they do not have the same material usage reducing property as bottom-up techniques. Top-down vertical NWs are more applicable for integrated circuits and field effect transistors than for III-V optoelectronic devices. Hence they are not discussed further within the scope of this thesis. [26]

2.3 Nanowire growth modes

The requirement for NW growth in MBE is a physical nucleation center where ad-atoms may diffuse along the substrate surface and the side facets of the NW or impinge straight from the molecular beams. All the growth modes presented in this chapter are based on similar diffusion processes although they have differences in the nature of the nucleation centers. [23] Growth modes presented in this chapter, disregarding the solution-liquid-solid mode, are applicable for NWs grown by MBE and MOVPE techniques.

2.3.1 Vapor-liquid-solid growth

The most common growth mode of semiconductor NWs is vapor-liquid-solid (VLS) mode, to which all other growth modes are typically compared to in literature. It was presented as early as 1964 [52]. In VLS mode, a liquid metallic nanoparticle acts as a seed for the NW growth. This nanoparticle may be gold or other metal that is not included in the bulk semiconductor, such as aluminum, nickel or titanium. Literature refers to this growth mode usually as metal-catalyzed or metal-induced growth. [23] Whether the nanoparticle is gold or other metal, it must be able to form supersaturated alloys with the group III element of the NWs. This means that it must melt in lower temperatures than the NW growth temperature, around <600 °C for Au assisted NW growth. [32; 53]

VLS growth of NWs begins by formation of these nanoparticles. Different gold particle deposition methods include annealing thin films, lithography, adsorption of colloidal particles from liquid phase and particles generated from aerosol phase. [54] The NW growth in the VLS mode is driven by thermodynamics. Supersaturation means that there is more solute in the solution or, for gaseous phase, that there is higher partial vapor pressure than equilibrium conditions enable. The supersaturation of the nanoparticle is a mandatory prerequisite for the crystallization of the NW material. In order to initiate the NW growth, the group III material diffusion and straight impingement must supersaturate the catalyst particle. This causes an incubation time before the NW growth is initiated. After the supersaturation is achieved the NW material begins to crystallize at the interface between the droplet and the substrate. Adsorption and adatom diffusion along the substrate surface and the NW side facets maintain the droplet supersaturation. This is only possible when even higher supersaturation surrounds the droplet. In other words rate of sidewall diffusion and direct impingement to the droplet must be greater than desorption and parasitic nucleation. Figure 9 presents these effects. [32; 53] The catalyst particle also acts as a catalyst for the decomposition of the chemical precursors when they are used. A review of VLS grown NWs can be found at [55].

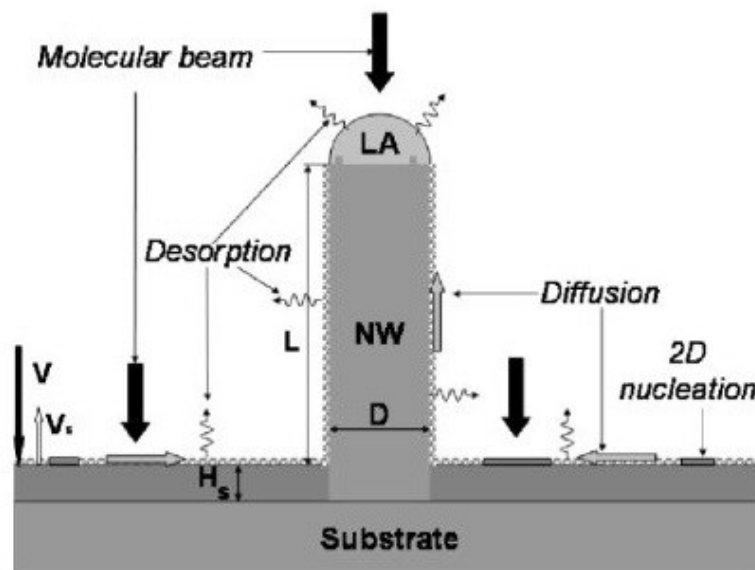


Figure 9. Schematic model of vapor-liquid-solid growth of NWs presents the material kinetics during the NW growth. [53]

In addition to this ideal NW growth model describing only axial growth, growth takes place also in NW sidewalls and in some cases on the substrate. The growth on side facets is called radial growth. It is caused by vapor-solid (VS) growth of side facets which is presented in chapter 2.3.4. Radial growth causes increase of the NW diameter or tapering as the growth proceeds. Growth on the substrate leads to parasitic island growth. These effects are schematically presented in Figure 10. NW growth conditions are usually optimized to minimize these effects. Radial growth is controlled by growth temperature and V/III ratio. In MOVPE also *in situ* etching of the side facets is possible in or-

der to compensate for the radial growth [56]. Parasitic growth can be significantly reduced by using oxide covered Si substrates [57] rather than oxide-free substrates [58]. Effect of the substrate surfaces is described in detail in section 2.4. Also the V/III ratio and the substrate temperature affect the amount of parasitic growth. [57]

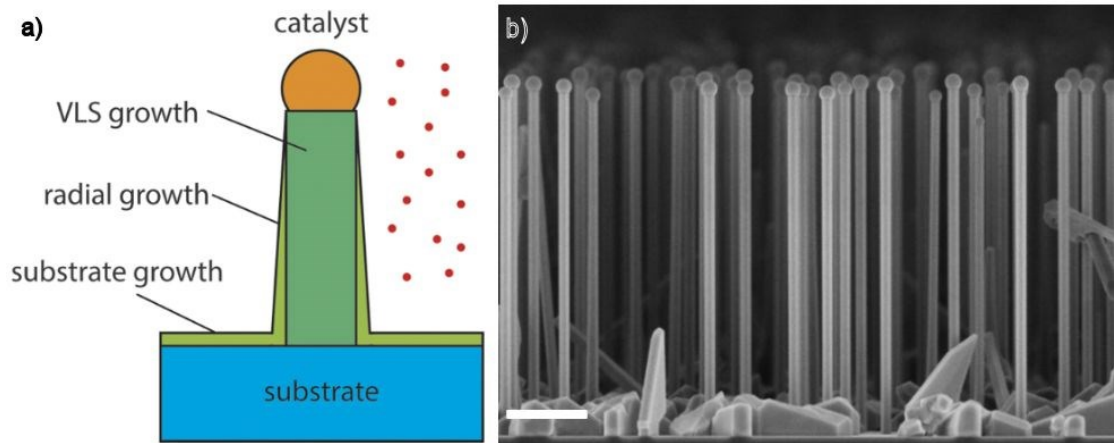


Figure 10. Schematic model of VLS growth with radial and parasitic substrate growth is presented in a) [55]. A SEM image of self-seeded GaAs NWs with some crystalline parasitic growth on the substrate surface is presented in b). The scale bar is $1\mu\text{m}$.

2.3.2 Vapor-solid-solid growth

The NW growth is also possible also with a solid state nanoparticle. This is obtained by reducing the growth temperature. Transition from VLS mode to this vapor-solid-solid (VSS) occurs in lower temperature than the melting point of the catalyst material. VSS growth mode is approximately one order of magnitude slower than VLS mode. Manufacturing of axial heterostructures with sharp interfaces is also possible in the VSS growth mode due to low solubility of the semiconductor material into the catalyst particle. The reduced growth temperature also enables the integration of NWs with standard CMOS manufacturing processes. [27]

2.3.3 Self-seeded growth

The discussion in this chapter is limited to self-seeded growth of GaAs NWs as they are the most relevant within the scope of this Thesis.

According to some references the usage of gold as the catalyst nanoparticle is beneficial over other metals in order to obtain single crystalline and well oriented NWs [54]. However, others claim that gold is harmful in terms of good quality crystalline structure compared to internal metal induced growth presented in this chapter [59]. In addition to high quality crystalline structure required for optoelectronic devices the electrical and optical properties of NWs must be precisely controlled. During external metal induced growth some atoms of the seed particle are incorporated into the NW. Au impurity at-

oms reduced the free mean paths of conducting electrons and scattering losses in Au catalyzed VLS grown GaAs NWs. [60] Au has also a negative effect on the n-type doping of GaAs NWs [61]. In addition the Au atoms incorporated into the NWs reducing the minority carrier lifetime by two orders of magnitude compared to NWs without Au-atoms. [35] However gold induced NWs with reasonable carrier lifetimes can be obtained as long as the crystalline quality of the NWs is high [37]. Also the intensity of photoluminescence of Au-catalyzed NWs ceases at temperatures higher than 120 K which implies the existence of nonradiative centers within the NWs. [62] From the application point of view, the most serious adverse effect of Au is the Au diffusion into the silicon substrate, where it forms deep level carrier traps [63;64]. Which makes the usage of gold induced NWs in optoelectronic devices and their integration on silicon questionable if not impossible. In order to solve these problems, the self-catalyzed (also self-induced, self-seeded, internal metal catalyzed, VLS, autocatalytic and catalyst free) growth mode has been developed [65].

The self-catalyzed growth mode takes advantage of an internal metal droplet, in case of GaAs gallium. External metal- and self-catalyzed growth modes are quite similar in terms of the growth kinetics. In both cases the liquid nanoparticle is the way for material diffusion into the NW and its size determines the thickness of the NW. [23] The parameters controlling the droplet size are the substrate temperature and the V/III flux ratio. As the substrate temperature or the group III flux increases also the droplet size increases. [66] The growth temperature must be near the temperature where the droplet is in liquid phase but it crystallizes under group V flux. This temperature is called congruent temperature. For GaAs it is 630 °C and for InAs 430 °C. [31] On Si(111) substrates the self-catalyzed GaAs NWs have been grown in temperatures from 560°C [59] to 660 °C [67]. Because the NW diameter depends on the droplet size it may increase during the growth if conditions are such that excess group III element is provided. On the other hand, if the group III partial pressure is too low the nanoparticle is consumed eventually preventing the NW growth. However, the local chemical potential seems to affect the gallium diffusion and hence variations in arsenic flux do not necessarily induce tapered NWs. [68]

In ordinary two-dimensional MBE growth the growth rate is controlled by the amount of group III element and excess group V element is provided. In the NW growth the situation is opposite and the amount of group III element provided on the substrate is not the main parameter affecting axial growth rate of the NW. The group V partial pressure controls the growth rate which is linearly dependent on it. If the group V element has too low partial pressure its' desorption from the group III droplet reaches equilibrium with adsorption and the NW growth is prevented. Thus it is important to be able to precisely control the V/III-ratio during the self-catalyzed growth also in the growth rate point of view. [69; 70; 71] Controversially to the model presented in [70], also the substrate temperature and the group III flux affect the growth rate. Increase of temperature

decelerates the growth [66; 71] and increase of Ga flux accelerates the growth. The latter does not obey any clear trend and the effect is not clearly explained [66]. The temperature dependence is at least partially related to local V/III ratio which is affected by the temperature dependence of gallium diffusion length. Increase of temperature increases the gallium diffusion length and hence V/III ratio decreases. [67]

As the NW grows the distance from lower part of the NW to the droplet increases and the Ga diffusion rate of additional material to the droplet decreases. This effect is predicted to stop the NW growth when the length reaches 40 μm which is significantly longer than typical NW lengths. [70] The Ga diffusion is a limiting factor of NW length because direct impingement of Ga into the droplets is negligible. However this limits only MBE grown NWs as in MOVPE material absorbs also on the sidewalls of the NW [53]. Also models predicting theoretical infinite growth are presented [32]. Arsenic is not a limiting factor of NW length as it is provided to the catalyst droplet via straight impingement and from secondary arsenic source provided by evaporation from substrate surface and NW sidewalls. [67; 68; 71].

The crystalline structure of the self-catalyzed GaAs NWs on Si(111) substrate is typically zincblende unlike Au catalyzed NWs that have wurtzite structure. This is due to lower surface potential of Ga droplets compared to that of Au droplets. A model of the catalyst droplet and its surface energies explaining the absence of wurtzite stacking faults in Ga induced growth is given in [59]. Controversially to this theoretical model, stacking faults with wurtzite phase do exist in self-catalyzed GaAs NWs [72]. Their occurrence is especially probable near the NW tips if the catalyst droplets are crystallized by shutting group III flux as the final step of the NW growth. This is explained by the changing size of the Ga catalyst droplet and the increasing group V partial pressure which affects the chemical potential. [59] However, the stacking faults at the NW tip may be avoided by a procedure of stopping Ga flux briefly before final growth and cooling the sample slowly under arsenic flux. [73]

2.3.4 Catalyst free growth

NW growth is also possible without a catalytic nanoparticle [74]. This type of growth mode is referred as metal-free, noncatalytic, catalyst-free [23] or vapor-solid (VS) [75]. It is important to note that also the self-catalyzed growth is sometimes referred as catalyst-free. For III-As compounds the catalyst-free growth occurs under As-rich conditions which prevent the formation of the group III catalyst nanoparticle. It is driven by different growth rates for different facets of the crystal. Hence the preferred facet for the growth is the physical nucleation center that induces the NW growth. Disadvantages of this growth mode for the III-V semiconductor NWs are high density of planar defects and slower growth rate compared to the VLS and the self-catalyzed modes. On the other hand, it enables growth of sharp axial heterostructures. Typically InAs NWs grow in catalyst-free mode but with As/Ga ratio larger than one also GaAs may be grown with-

out the Ga catalyst particle. [76] InAs NWs can be grown by this method with extremely high (120) V/III ratios. In contrast to the self-catalyzed growth mode, the growth rate is controlled by the substrate temperature and the group III flux. The catalyst free growth of InAs NWs begins in In rich conditions, possibly in presence of liquid indium droplets. After short growth time < 2 min the droplet is consumed and the V/III ratio stabilizes. [75]

2.3.5 Solution-liquid-solid growth

NW growth may occur also in solution phase. The solution-liquid-solid (SLS) method is strongly analogous to VLS growth mode. The solution based NWs grow in the presence of a catalytic nanoparticle which is typically gold or bismuth. These nanoparticles are either injected in the solution where the growth occurs [38] or deposited on a substrate [39].

The chemical precursors present in the solution phase diffuse into the catalyst particles where they dissociate and release elemental NW materials. As the NW material supersaturates the catalyst particle, the NW growth begins. The NW growth is maintained by continuous availability of precursors in the solution. The growth rate can be limited by precursor diffusion along NW sidewalls or by direct impingement to the catalyst particle. Detailed model of SLS growth is presented in additional material of [41]. The growth mode is schematically presented in Figure 11. In addition to SLS mode, also different solution based growth mechanisms exist such as supercritical fluid-liquid-solid [77] and supercritical fluid-solid [40]. They are not further presented within the scope of this thesis.

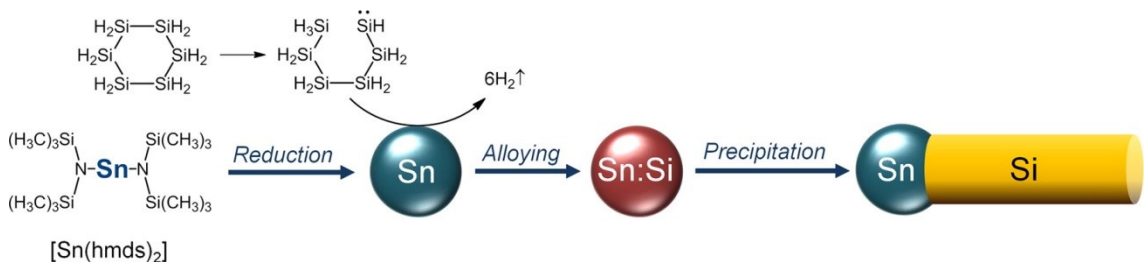


Figure 11. A tin nanoparticle catalyzes the decomposition of cyclohexasilane forming tin-silicon alloy providing material for NW growth as the silicon concentration saturates. [78]

SLS NWs are typically very thin, having even sub-10 nm radii. Hence, quantum confinement affects the allowed electron states in the NWs and they are also referred to as quantum wires. [39] They are typically not vertical but either tangled meshes forming non-epitaxial films [38; 39], horizontal with respect to the substrate or pointing at arbitrary directions [41]. This morphological difference and the thinness of SLS wires are the most important properties separating them from epitaxial vapor phase grown NWs. The NWs grown by the solution based methods have several disadvantages compared to

wires grown in the vapor phase. The amount of the chemical precursors in the used solution varies uncontrollably as the material is absorbed to the growing NWs. All precursors participate in the reaction simultaneously in the flask based method unlike in the vapor phase methods. This reduces the amount of radial heterostructures obtainable via solution based methods. In addition, the growth rate is in micrometers per minute – range which makes *in-situ* monitoring and quantitative analysis of the growth mechanism impossible. A flow-based SLS method is developed in order to diminish some of these problems. [41] SLS growth mode has also some advantages over vapor phase methods. They include precise control over NW size and morphology. In addition the solutions used in SLS growth include surface-coordinating ligands that passivate the surface of the NW by forming coordination bonds with the dangling bonds on NW surface. The crystalline quality of the SLS grown NWs is equivalent to VLS grown. [41] The scalability of the process makes it cost effective [39] although, processes required to straighten and organize the NWs grown in tangled meshes are the factor that reduces upscaling the liquid phase growth of NWs [26].

2.4 Effect of substrate and oxide layer on nanowire growth

The substrate surface has a tremendous effect on the NW growth. In this chapter different surfaces enabling NW growth are presented focusing on Si substrates and self-catalyzed III-V NWs. These include growth in random pinholes in silicon dioxide SiO₂ [70], selective area epitaxy (SAE) [79; 80], growth after droplet epitaxy of nanocrystals formed of the same composition as the NW [57; 72] and finally, self-catalyzed growth on lithography-free patterns in silicon oxide layer, which is the technique used in the NW growths conducted in this thesis [81]. Figure 13 at the end of this chapter illustrates characteristics of the effect of substrate and oxide layer on NW growth for the techniques presented in this chapter.

2.4.1 Random pinholes in oxide layer on substrate

NW growth in random pinholes in SiO_x occurs on a substrate covered in porous SiO_x mask which has thickness under 30 nm or on a native oxide on Si substrates. Sputtering or other oxide deposition technique is used with GaAs substrates for GaAs NWs. Oxide layer prevents Ga wetting of the surface and hence enables droplet formation [31]. The nature of the oxide layer has a significant effect on yield of successful NWs also in growth occurring on Si substrates. [82] No surface preparation is required when the native oxide layer of the Si substrate is used. Hence, it is the most commonly used surface when NWs are grown in the random pinholes in the oxide layer on Si substrate. [59] However, the characteristics of the native oxide vary between substrate manufacturers and batches affecting the NW growth significantly [82].

The NW growth mode is self-catalyzed in the growth in random pinholes in oxide layer on the substrate. When the oxide layer is thin enough, 30 nm for sputtered oxide on GaAs substrate [65] to less than 2 nm for thermal oxide on Si substrates [82], the NWs have epitaxial relation with the substrate. Ga deposited on SiO_x covered substrate further etches the pinholes, which must reach the Si/SiO_x interface in order to obtain epitaxial NWs. As the holes reach appropriate dimensions droplet nucleation begins. Hence, the oxide roughness must be comparable with the oxide thickness in order to obtain NW growth. [82] The nucleation process increases the incubation time for the NW growth in random pinholes. The incubation time varies for different catalyst droplets leading to wide length and diameter distributions. The SiO_x mask also increases diffusion length of Ga on GaAs so its usage is beneficial in order to obtain increased migration into the Ga droplets functioning as nucleation centers and higher growth rates. [65; 66; 70] Compared to the droplet deposition based methods on substrates with no oxide layer presented in chapters 2.4.3. and 2.4.5. growth in random pinholes has few disadvantages. First, finding suitable temperature range for the droplet deposition is rather difficult and the range is narrow. This reduces the achievable NW density as the droplet density is a strongly affected by the droplet deposition temperature. [59] A significant disadvantage from the application point of view is the wide length and diameter distributions presented in [66; 83]. Also optimizing the NW growth direction is problematic. As the oxide thickness grows over 30 nm no epitaxial relation between the substrate and the NWs occur and the growth directions become arbitrary. [65] The main parameter affecting the NW orientation on Si(111) substrates covered by native oxide is the V/III ratio at the substrate surface. Temperature locally affects this ratio significantly inducing variations even at different locations on the substrate. [67] Also the composition and the roughness of the oxide layer affect the yield of successful NWs significantly [82]. There is an optimal temperature for each V/III ratio where the yield of vertical NWs is highest. The temperature must be such that V/III ratio is high at the group III droplet and it is typically found at high end of growth temperatures near 660 °C [67] or 640 °C [82] depending on the source.

2.4.2 Selective area epitaxy

In selective area epitaxy (SAE) the NW growth occurs on an ordered pattern of openings formed on a silicon dioxide mask. Typically Si(111) substrate is used for study of III-V NW growth. The openings may be formed by various lithographical methods, for instance electron beam lithography [80] or nanoimprint lithography [84]. The mask manufacturing also requires etching. The openings offer a preferential nucleation site for self-catalyzed [80] or catalyst-free [85] NW growth. The GaAs NW growth mode is typically self-catalyzed in MBE and catalyst-free in MOVPE [86]. Another way to produce position controlled NWs is forming an array of nano-droplets, for example Au, on the substrates. The droplets function as the catalyst particles for the NW growth. This leads to Au-catalyzed VLS growth which is not preferred. [80]

In SAE, the diameter of the NWs is almost independent of the size of the openings. [87] Even though the opening size does not affect the NW diameter, a pedestal is formed when wider openings are used. The pedestal is formed as the Ga droplet adapts to the mask opening size in the beginning of the growth. Later, the droplet size reduces as it reaches steady state which is determined by the V/III ratio. [86] Also tapered NWs may be formed as the radial growth fills the openings in the oxide layer. Tapering can be reduced by increasing the growth temperature as it enhances the sidewall diffusion. Even though the NW diameter changes as a function of time or pedestals may be formed, the diameter distributions obtained via SAE are narrow compared to the growth in random pinholes. [84] The distance between the openings affects the diameter and the length of the NWs. As the distance increases also the NW dimensions increase until certain constant level is achieved. This constant limit represent diffusion limited growth regime where adjacent NWs are separated by more than twice the material diffusion length on the substrate. Increasing distance between NWs also induces twin defects by increasing effective As/Ga ratio. Therefore, the optimal NW growth conditions depend on the separation of the openings. [86]

SAE is a controlled way to study the kinetics of the NW growth. For instance the diffusion length of the group III atoms on SiO₂ may be found by varying the distance between openings. It is also a way to achieve position controlled NW growth with constant density. These kind of homogeneous structures have optical properties that can be predicted more precisely. [79] Also the narrow diameter and length distributions enhance the homogeneity of NW arrays grown by SAE. NW densities obtained by SAE vary as a function of the pitch between adjacent NWs. Pitches may vary from 200 to 2000 nm. These pitches correspond to densities from $1.1 \cdot 10^9 \text{ cm}^{-2}$ to $2.7 \cdot 10^7 \text{ cm}^{-2}$. This is relatively wide density range and it might be extended by increasing or reducing the pitches. Vertical NW growth direction is obtained by optimizing the arsenic partial pressure. [84] The major disadvantage of selective area growth is the complexity of the sample preparation. [80]

2.4.3 Droplet epitaxy based methods

The first step of growing NWs by depositing nanocrystals of NW material on the Si substrate without oxide layer is droplet epitaxy. [72] Droplet epitaxy occurs under different growth conditions than ordinary two-dimensional growth. The droplets are formed under group III flux only. During this droplet deposition phase the substrate temperature must be such that the lateral material diffusion from the droplets is prevented but the diffusion length is adequate for material diffusion into the droplets. Two main parameters affecting the droplet density are the substrate temperature and the group III flux the prior having greater effect. [30] The Ga droplet density on Si(111) substrate varies as a function of the Ga deposition temperature from 10^6 cm^{-2} to over 10^9 cm^{-2} as the deposition temperature varies from 500 to 300 C°, respectively. [57] Expanding

this range is possible, at least for GaAs substrates, up to 10^{11} cm^{-2} range. The ad-atom diffusion on the substrate surface is a thermally activated process. Hence, the droplet density has an exponential dependence on the substrate temperature which can be expressed by a linear Arrhenius plot. Flux variation from bulk growth rate of 0.01 to 1 $\mu\text{m/h}$ varies the droplet density from 10^8 cm^{-2} to 10^{10} cm^{-2} on GaAs substrate at 300 $^{\circ}\text{C}$ growth temperature. The functional behavior of the droplet density flux dependence is monomial so it is linear on log-log scale. [30]

After the droplet deposition group V flux is provided in order to crystallize the droplets. [30] Practically all droplets are crystallized so the droplet density determines also the nanocrystal density. The crystallization of the droplets is typically conducted in a lower temperature (150 $^{\circ}\text{C}$) than the droplet positioning. After the nanocrystal positioning the substrate may be oxidized in air. This reduces the amount of parasitic growth during the NW growth but exposes the substrates to possible contamination from air. [57; 72], The NWs are subsequently grown on top of the nanocrystals grown by droplet epitaxy. The growth mode is self-catalyzed for GaAs NWs. The NW growth is initiated by simultaneously opening Ga shutter and As needle valve. The substrate temperature and the V/III ratio must be optimized in order to obtain high yield of successful NWs. In [57] optimal growth temperature was 580 $^{\circ}\text{C}$. The optimal V/III ratio was different for NWs with different diameters. It was 3 for NWs with 120 nm diameter and 1 for NWs with 40 nm diameter. Thinner NWs were obtained by using a template with smaller GaAs nanocrystals and higher number density. [57]

Also InAs NWs have been grown on oxide-free surfaces. Even though no separate InAs nanocrystal growth step subsequent to NW growth is presented, this growth technique is droplet epitaxy based since the growth mode was initially self-catalyzed and after a short nucleation period transition to the catalyst-free growth mode occurred. Hence, the NW density was controlled by In droplet density which behaved qualitatively similarly to the Ga droplet densities presented above. However, the In flux dependence is stronger compared to that of Ga. [75] The NWs grown by nanocrystal deposition method have a base structure wider than the NW itself. The NW diameter is approximately half of the base diameter. The transition region between the base and NW itself does not contain defects or stacking faults. [57] NWs grown on oxide-free surfaces are vertical, and hence epitaxial, independently of the V/III ratio and the growth temperature. [57; 72; 88]

2.4.4 Growth in lithography-free patterns in oxide layer

NW growth in lithography-free oxide patterns exploits the benefits of the previously presented techniques. Schematic model of this technique is presented in Figure 12.

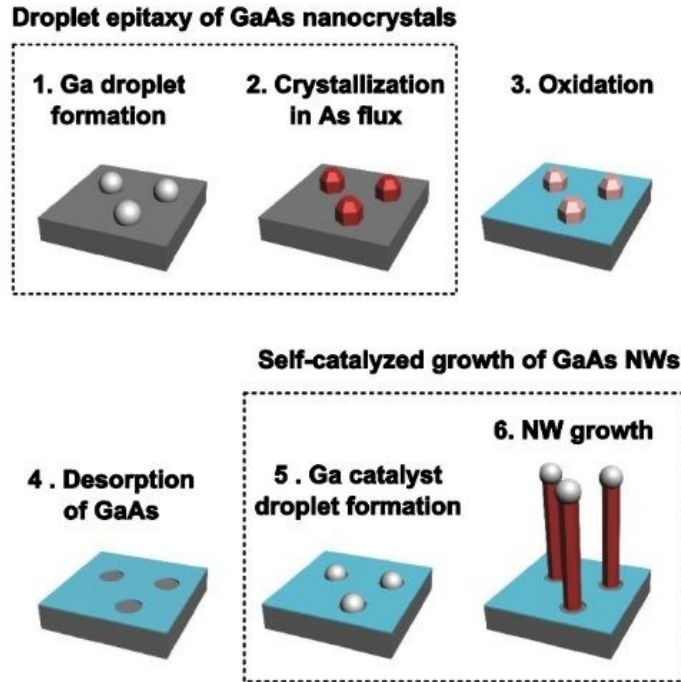


Figure 12. Steps of the NW growth in lithography-free oxide patterns. [81]

The first step of NW growth in lithography-free oxide patterns is the Ga droplet epitaxy presented in chapter 2.4.3. The native oxide on the substrate surface is removed before substrate introduction into the MBE reactor. The droplet epitaxy enables precise control of the nanocrystal density and diameter. The Si(111) substrate temperature and the Ga flux control the density of the Ga droplets and the amount of deposited Ga determines their size. Ga droplets are crystallized at their deposition temperature (480 °C to 570 °C) by closing the Ga shutter and exposing them to arsenic flux for 10 min. After the formation of GaAs nanocrystals the substrates are removed from the vacuum and oxidized in air for 18 h. This forms an oxide layer covering the substrate and the nanocrystals. The next step is annealing the substrates in the MBE chamber at 660 °C for 30 min. This evaporates the oxidized GaAs nanocrystals but not the SiO₂ layer, thus leaving a pattern of openings in the oxide layer. This hole-pattern is then used as a template for the self-catalyzed NW growth similarly to the SAE templates. The catalyst droplets are formed by depositing Ga on 640 °C with 0.3 ML/s growth rate for 60 s. The droplet size is limited by the opening size and every opening is populated. The NW growth is initiated by supplying also As₂ with V/III flux ratio of 8.5. [81] This technique combines the simple pre-treatment of growth on SiO_x layer with precise controlling of NW density and diameter of droplet based methods and small length and diameter variations obtained by SAE growth. [81]

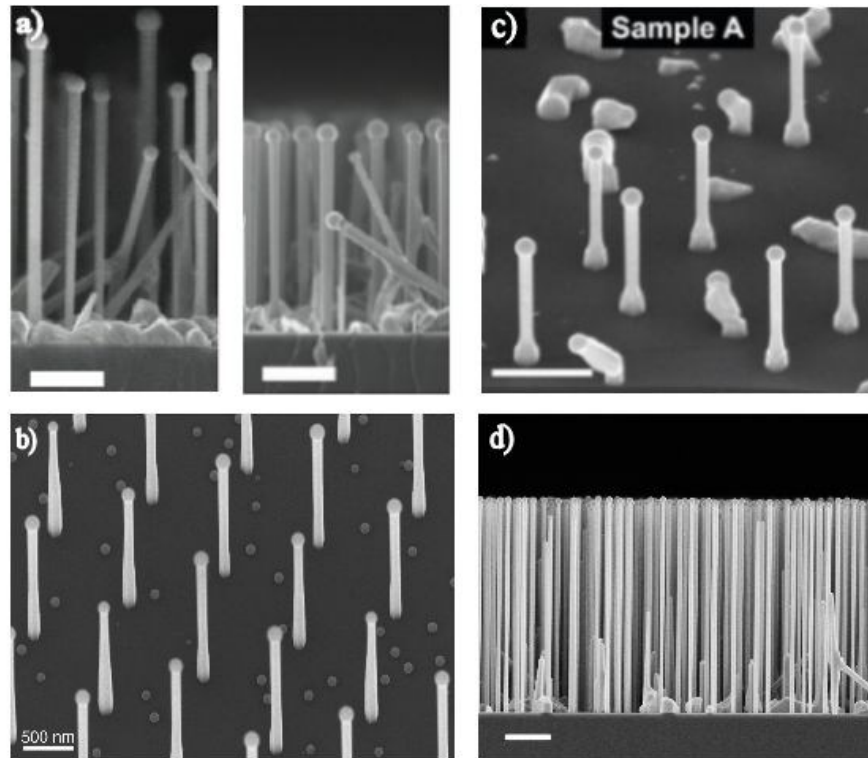


Figure 13. SEM-images of self-catalyzed GaAs NWs grown on Si(111) substrates but on different templates are presented. In a) two sets of NWs grown in random pinholes in a native oxide layer is presented. In addition to wide length and width distributions also a large amount of parasitic growth can be seen. [66] b) presents SAE [84] and c) droplet epitaxy based method [57]. The pedestals can be seen in b) and c). In d) NWs grown in lithography-free oxide patterns with narrow length and width distributions are presented.

2.5 Nanowire heterostructures and doping

Two types of heterostructures can be integrated in the NWs. They are illustrated in Figure 14. Axial heterostructures have different compositions or varying doping profiles along the NW axis. They have been used for lasers [89] and solar cells [5]. Core-shell or radial heterostructures are formed so that there is at least one compositional or doping interface along the NW side facets. [23] They are also referred as prismatic heterostructures [31]. Core-shell structures are used to improve the optical properties of the NWs [8; 62], or to create radial quantum wells used in LEDs [6] and lasers [89].

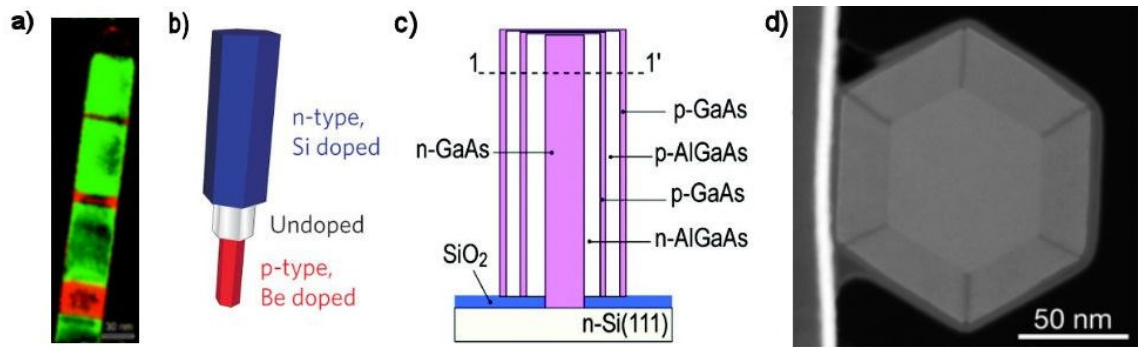


Figure 14. a) presents a TEM image of VLS InAs (green) NW with InP (red) axial heterostructures forming potential barriers for electrons [90]. In b) a radial doping heterostructure used in solar cells is presented schematically [91]. A core-multishell NW used as a LED structure is presented schematically in c) [6]. A cross-sectional high-angle annular scanning transmission electron microscope (HAADF-STEM) image of a GaAs/AlGaAs/GaAs core-shell NW is presented in d) [92].

Axial heterostructures enable growth of highly mismatched heterostructures such as GaAs/InAs with a lattice mismatch of 7 %. Axial heterostructures may be grown either via gold induced VLS or self-catalyzed growth modes. Sharp axial group III interfaces are difficult to obtain in VLS mode, due to the high solubility of the group III element to the external catalyst droplet in VLS mode. [23] Group III axial heterostructures have been grown also from ternary alloys such as $\text{In}_x\text{Ga}_{1-x}\text{As}/\text{GaAs}$ in the self-catalyzed growth mode. The optical properties of the NW can be tuned by gradually varying the material composition along the NW axis. [93] However, group III elements solute into Ga in high concentrations making fabrication of sharp heterointerfaces problematic. The group V solubility in Ga and In is low enabling growth of sharp GaAs/GaP [94] and InAs/InP [90] axial interfaces. [94] Also high quality axial AlN/AlGaIn/GaN heterostructures have been grown by MBE. However $\text{Al}_x\text{Ga}_{1-x}\text{N}$ and AlN NWs exhibit finite radial growth rate during NW growth which forms a slightly asymmetric shell structure around the NWs. [95] Controlling the NW diameter while growing axial heterointerfaces has also been found to be difficult for GaAs/ $\text{In}_x\text{Ga}_{1-x}\text{As}$ material system as the alloying metal solutes into the catalyst droplet increasing its size. For this material system, optimizing the growth temperature is also problematic in order to maintain adequate diffusion length for gallium but not to vaporize indium. [96]

Core-shell heterostructures enable growth of radial quantum wells in VLS [97; 98;99] or in self-catalyzed mode [100]. AlGaAs/GaAs [99] and InGaAs/GaAs core-shell structures have been grown on GaAs substrates in VLS mode [98; 101] InGaAs/GaAs core-shell structures have also been grown on Si substrate in self-catalyzed mode [7]. For instance GaAs shell over InGaAs core is grown in VLS mode simply by shutting the indium flux and continuing the growth under gallium flux. This produces core-shell structures with tapered pencil like tips of pure GaAs. [101] In order to obtain core-shell structures in self-catalyzed growth mode the axial growth is terminated by interrupting the group III flux. During the interruption group V flux crystallizes the group III droplet

preventing self-catalyzed growth. After this the growth is continued using higher V/III-ratio and lower growth temperature, which suppress the adatom migration along the NW and promote the growth on the $\{110\}$ facets of the NW sidewalls. [92; 100; 102] The radial growth rate is smaller than that of normal 2D growth. This is caused by the reactor geometry designed for planar growth on surfaces parallel to the substrate. For cell tilt angle of 33° the sidewall growth rate is roughly 20 % of the planar growth rate. [92] Because most of the III-V semiconductor applications exploit some kind of quantum well or other heterostructures, being able to grow core-shell structures is very important from application point of view. [100] In addition, surface passivation is required for AlGaAs and InGaAs alloys. Passivation prevents the aluminum and indium from oxidizing. It is typically done by growing a GaAs cap on the structure. In case of NWs this cap is a shell structure grown radially around the NWs. Core-shell structures also enable confining free carriers in the NW core. For example, GaAs must be passivated with a shell structure having a larger band gap, typically AlGaAs, in order to prevent fast nonradiative surface recombination which is presented in the next chapter.[103] In core-shell structures the Al or In composition may be smaller compared to thin film growth. This is due to shorter diffusion length of aluminum than that of gallium and the diffusion length dependent NW growth rate. [102] In case of indium this is caused by evaporation as the growth temperature of InAs [75] NWs is 200°C lower than that of GaAs [66]. However in optimized conditions the varying composition can be avoided at least for GaAs/AlGaAs structures [92].

2.6 Optical properties of nanowires

Owing to the intended use as building blocks for optoelectronic devices, the optical properties of NWs have been quite extensively studied. In this chapter the general optical properties of III-V semiconductors are presented via carrier dynamics. Effects concerning NWs are emphasized. Also other optical properties present in NWs such as large absorption cross-section and wave guiding are presented.

2.6.1 Carrier recombination and lifetime

Radiative and nonradiative carrier recombination processes and diffusion are typically studied with photoluminescence spectroscopy (PL). In PL, an excitation laser is used to excite electrons from the valence band to the conduction band. Simultaneously, holes are generated in the valence band. The photoexcited electrons and holes rapidly thermalize to the lowest possible conduction band states and highest possible valence band states, respectively, which are located at the Γ -point of the band structure. The electrons and holes may recombine radiatively and emit a photon having energy equal to the band gap energy. The electron may also recombine nonradiatively via thermal relaxation. Another way for nonradiative recombination is the Auger recombination, where an electron and a hole recombine while transferring the energy obtained from the recombina-

tion to a third carrier. It must be taken to account at high carrier concentrations which are obtained using higher excitation intensities in PL. Typically, power, time or temperature dependent measurements are used for investigating carrier dynamics. [22] NWs are also studied using spatially resolved or micro-photoluminescence (μ -PL), which enables investigation of single NWs and even emission arising from different parts of a single NW [93; 98; 104].

The ratio between radiative and nonradiative recombination is an important figure of merit that describes the optical properties of materials. Nonradiative recombination occurs at impurity sites where contaminants form excess states in the band gap. Dangling bonds at material surfaces form surface states which lead to nonradiative recombination. The surface recombination is especially important in NWs due to their large surface to volume ratio. The surface states may be passivated with a larger band gap material which prevents the carrier diffusion into the surface states. For example GaAs, that exhibits extremely fast surface recombination, is typically passivated by AlGaAs. [22] The AlGaAs passivation enhances the PL intensity of GaAs NWs with a factor of 10^3 or even more [92]. Even though the shell enhances the PL intensity, it induces strain into the NW core. Due to the strain the shell thickness should be kept well under 50 nm [103]. Also chemically produced monolayer thick nitride layer may be used to effectively passivate the surface states in GaAs NWs [104]. Typically recombination rate is faster for nonradiative than for radiative processes. For this reason long carrier lifetimes indicate low impurity concentration and successful surface passivation. [35] Due to different recombination rates for different transitions, two time constants for carrier recombination may be found. [81] The excitation power dependent PL measurements are used to qualitatively study the impurity densities. When impurity emission saturates with low excitation powers the impurity density is typically low. [22]

In low temperatures excited carriers form excitons. They are hydrogen like quasiparticles composed of an electron-hole pair bound together by Coulombic force. Their recombination energy is slightly smaller than that of the ordinary band gap, and the energy difference is the exciton binding energy. Excitons can be free or bound. The bound excitons are localized in a state with lower potential caused either by an impurity, a quantum well or a quantum dot grown to tune the band gap energy. Excitonic and shallow radiative impurity state recombination, caused for example by carbon impurities [105], quench while temperature increases as carriers are thermally excited out of these states. As temperature further increases the emission peaks widen because the carrier distribution in the conduction band follows the Boltzmann distribution. [22] Also the ratio of radiative recombination weakens as the carrier diffusion length increases enabling their migration into nonradiative states. [106]

In NWs, WZ segments along the axis of a ZB NW affect the carrier recombination energies. The band gap energy of WZ GaAs is still under debate values ranging from 20 meV below to 100 meV over the band gap of ZB GaAs. Recent values can be found in

[107]. Stacking faults and other small WZ segments form narrow axial quantum wells with a broad width distribution. This induces a significant broadening in the emission spectrum of NWs with stacking faults. Also spatially indirect transitions occur due to the type-2 band alignment between the ZB and WZ phases: an electron on the ZB conduction band may recombine with a hole on the WZ valence band emitting significantly longer wavelengths than intrinsic WZ or ZB recombination. This effect and the resulting PL spectra as a function of location along NW axis are presented in Figure 15. [16; 107]

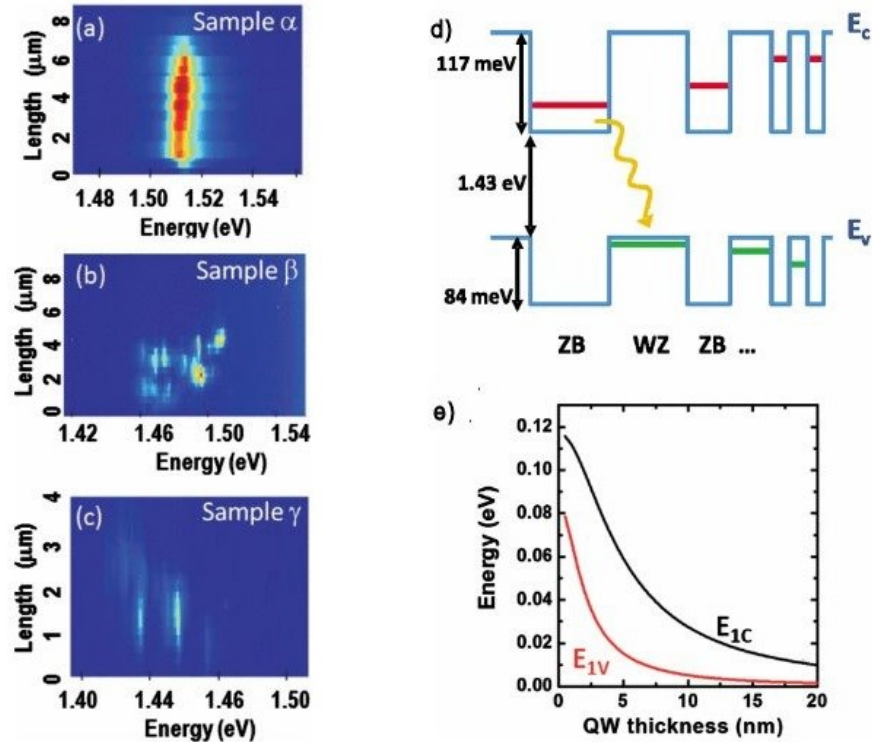


Figure 15. Spatially resolved confocal PL spectra with increasing amount of WZ segments are presented in a) to c) respectively. d) and e) present the possible ZB-WZ transition and variation of band energy as a function of quantum well width. [16]

2.6.2 Absorption and cavity properties in nanowires

NWs exhibit significantly different absorption properties compared to bulk materials. Absorption of vertical GaAs NWs is very efficient. Theoretically the power absorbed by the NWs is at least ten times larger than the illumination power at the area they physically occupy. This applies to wavelengths between 300 and 900 nm and NWs with diameter between 50 and 150 nm. Their absorption cross-section is hence wider than their physical size. This applies also with wider NWs having diameters up to 400 nm. As the absorption cross-section is significantly larger than the actual NW size the pitch between the wires may be widened simultaneously gaining more absorption for a single NW. The NW works as a cavity for light and the intensity becomes almost constant along the NW axis. These properties may be exploited in solar cells by integrating a

core-shell p-n junction in to NWs. The homogeneous intensity distribution induces a homogeneous free carrier concentration along the wire axis making the NWs potential building blocks for solar cells. [80] Vertical NW array has a significantly higher external quantum efficiency compared to horizontal NWs when considering solar cell applications. Simultaneously vertical NWs have smaller footprint increasing the potential wire density. NW solar cells have been realized, for example, using GaAs with radial p-i-n junction [91] and InP NWs with axial p-i-n junction [5]. However, the best theoretical conversion efficiency of 42.3 % is obtained for GaAs_{0.77}P_{0.23} NWs grown on top of a planar Si solar cell. The GaAs_{0.77}P_{0.23} NWs have a 1.7 eV band gap and a radial p-i-n junction as a functional layer of the solar cell. [3] Single NW solar cells with corresponding structure have also been realized [108].

Besides the large absorption cross-section NWs also have good waveguiding properties which keep light trapped inside the NW. GaAs NWs in air work as waveguides and can function as a Fabry-Perot cavity. A single vertical NW can support the fundamental HE₁₁ mode. [109] These cavity properties have led also to formation of GaAs-AlGaAs NW lasers [1] which have been already realized as monolithically integrated on Si substrates [2]. The thickness of the NWs significantly affects their confinement factor which describes the fraction of the supported laser mode confined inside the gain material. Thicker NWs offer better confinement and hence the GaAs/AlGaAs NWs supporting laser modes have been 340 nm [1] and up to 470 nm [2] thick. Also NWs with embedded quantum dot chains grown as axial heterostructures have been used as laser structures [110]. In addition to III-V materials, also II-VI NW lasers have been extensively studied [89].

NWs have also interesting polarization dependent properties. A purely classical electromagnetic theory shows that absorption and emission in NWs is polarization dependent so that light polarized parallel to the NW experiences an absorption and emission maximum. However, this analysis is only valid when the dielectric constant of the NW is high, around 10, the free carrier diffusion length in the NWs is shorter than the NW diameter and the distance between the NWs is significantly larger than the NW diameter. [111] The dielectric constants of III-V semiconductors are in the required range except for AlN and GaN having values around 5. [11] Also the requirements for the NW diameter and the distance between the NWs are usually fulfilled. The latter often due to the fact that single NWs removed from the substrates are used for the polarization dependent PL measurements. However, the polarization effects are more complicated as the NW consists of segments with different crystalline structure. For example, low temperature measurements have shown that in GaAs NWs with various WZ segments emission with polarization perpendicular to the NW axis is stronger. This is caused by the spatially indirect transition between ZB conduction band and WZ valence band. [107]

3. METHODS

This chapter presents the methods used in this thesis. First, the MBE reactor and the growth of GaAs nanocrystals, the GaAs NWs and the GaAs/AlGaAs/GaAs core-shell NW heterostructures are presented. After that, the characterization methods, atomic force microscopy (AFM), scanning electron microscopy (SEM), X-ray diffraction and photoluminescence spectroscopy including the experimental setup are presented along the analysis methods.

3.1 MBE growth

All samples grown within this thesis were grown in VG Semicon V80 (referred as 10-2) and V90 molecular beam epitaxy reactors. The 10-2 reactor, used for all NW and most of the droplet epitaxy growths, consists of three different vacuum chambers, fast entry lock, preparation chamber and growth chamber. The growth chamber is equipped with two gallium, one indium, aluminum and bismuth effusion cells and arsenic and antimony crackers with needle valves. For doping it has a gallium telluride effusion cell and a silicon and beryllium dual dopant cell. The material fluxes are measured with an ionization gauge and calibrated to correspond to the growth rates by growing distributed Bragg reflector (DBR) samples with a cavity. Afterwards the reflectivity of the cavity sample is measured and compared to modelled structure giving the real layer thicknesses of the grown sample. A pyrometer and a thermocouple are used to monitor the substrate temperature.

3.1.1 Droplet epitaxy of GaAs nanocrystals on Si

NW growth procedure began with the growth of GaAs nanocrystals according to NW growth in lithography-free oxide patterns presented in chapter 2.4.4 The first objective of the droplet epitaxy growths was to optimize the droplet density to low 10^8 cm^{-2} - range. The first growths were conducted on p-type Si(111) substrates. Later n-type substrates were used. Before introduction to the loading chamber the substrates were treated in 5 % aqueous HF solution for 10 s, rinsed with deionized water and blow dried with nitrogen. HF treatment removes the native oxide layer and creates a hydrogen terminated surface indicated by strong hydrophobicity [112]. H-termination prevents oxidation during the wafer loading procedure so the Si substrates are oxide free. Also different pre-treatment processes were tested namely Piranha, referred also as SPM in literature, and RCA 1. [112] Substrates protected with thermally grown oxide layer were

also used after etching the oxide completely away with HF solution. Details of the samples and their pre-growth treatments are presented in Table 2 in chapter 4.1.

After the cleaning processes the substrates were immediately moved to the entry lock of the reactor to prevent oxidation. They were annealed at 275 °C in the preparation chamber of the reactor in order to remove water. In the growth chamber the samples were further heated because annealing in temperatures over 490 °C removes the hydrogen from the substrate surface [113]. The annealing temperature was set between 650 and 850 °C as measured by a thermocouple. The pyrometer readings and hence the real temperatures are about 100-110 °C lower than the set point values so that for higher set point values the error is larger. For example set point temperature of 750 °C corresponds to pyrometer reading around 640 °C depending on the sample holder. The samples were held in the heat treatment temperature for 10 minutes before reducing the temperature to 545 °C which was the temperature used for gallium droplet formation. Also temperatures of 520 °C and 570 °C were tested in 10-2 reactor and 480 °C, 505 °C and 550 °C in the V90 reactor. The gallium flux corresponded to two dimensional growth rate of 0.1 ML/s. The shutter was held open so that the Ga coverage θ corresponded to 0.19 nm (0.7 ML) planar growth of GaAs on a GaAs(100) substrate. Also smaller gallium amount (0.09 nm or 0.3 ML) was tested. Immediately after closing the gallium shutter the droplets were crystallized in the growth temperature in an arsenic flux corresponding to V/III ratio of 23.5 for 0.1 ML/s growth rate. The droplets were exposed to the As flux for ten minutes and the As valve was kept open during the cooling process until the thermocouple temperature reached 500 °C.

The effect of various pre-growth treatments, different substrate types and pre-growth annealing temperatures on the droplet density was tested. Furthermore, nanocrystals were growths were performed in two different MBE systems in order to test the influence of possible trace elements. Most of the nanocrystal samples were grown in the 10-2 reactor which is a 10-port VG V80 MBE system equipped with As and Sb cracker sources, and Ga, In, Al and Bi effusion cells, and GaTe, Si and Be dopant sources. The other system used for the droplet epitaxy is a VG V90 system, which does not have Sb, GaTe or Bi sources, but has been extensively used for growths with phosphorus.

3.1.2 Growth of GaAs nanowires on Si

A single NW sample was grown within the course of this thesis. This sample is referred as sample 4 in x-ray diffraction analysis. It was grown on GaAs nanocrystal sample 2 which was oxidized in air and annealed *in-situ* before growth so the NW growth occurred on lithography-free patterns in silicon oxide. [8] The GaAs nanocrystal density of the template was $6.28 \times 10^8 \text{ cm}^{-2}$. The DE sample was annealed in 655 °C (750 °C set temperature as measured by a thermocouple) for 30 min in order to evaporate the GaAs nanocrystals and form holes in the SiO_x mask. A 1 min Ga wetting in 640 °C followed the annealing. The Ga deposition rate corresponded to 0.29 ML/s (300 nm/h) two-

dimensional GaAs growth on GaAs(100) substrate. The NW growth was initiated in the same temperature by opening the As cracker needle valve so that V/III ratio was 8.7. After 60 min the growth was stopped by closing simultaneously the Ga shutter and As cracker before reducing the substrate temperature. This was done to preserve the Ga droplets in the NW tips.

Three NW samples (samples 1-3) used for XRD, growth rate determination and photoluminescence were previously grown similarly on a template with GaAs nanocrystal density $1.6 \times 10^8 \text{ cm}^{-2}$. In the NW samples 1-3 the NW growth times were 5, 20 and 40 min, respectively, and the Ga droplets were crystallized by exposing the samples to As flux during the cooling process.

3.1.3 Growth of GaAs/AlGaAs heterostructure nanowires

Two core-shell NW samples (B and C) consisting of a GaAs core, inner AlGaAs and outer GaAs passivation shells were grown in order to study their optical properties. The radial growth of the NW shells occurs under higher V/III ratio and lower growth temperature which reduces the adatom migration length. Because of the reduced migration length, the growth rate of the shell structure is determined by the rate of straight adatom impingement to the NW sidewalls, which is governed by the growth chamber geometry. As the NW sidewalls are in 90° angle with respect to the substrate surface, the straight adatom impingement rate differs from regular 2D growth. The flux impinging NW sidewalls can be determined from a geometrical consideration. From Figure 16 b) it can be seen that area where the material flux hits the NW sidewall (A_{sw}) and the area where the flux would hit a corresponding planar surface (A_{2D}) obey a relation

$$\tan \alpha = \frac{A_{2D}}{A_{sw}}, \quad (4)$$

where α is the tilt angle of material sources. As the material flux is inversely proportional to the area where it hits, the flux that hits the NW sidewalls f_{sw} is given by

$$f_{sw} = f_{2D} \tan \alpha, \quad (5)$$

where f_{2D} is the flux on a planar substrate and α is the angle of the material source. In 10-port VG Semicon V80 reactor used for NW growths the angle was measured to be between 35 and 36 degrees. Due to the sample rotation during the growth, one side of the NW is always shadowed which further decreases the average flux hitting the NW sidewalls and the radial growth rate. This effect is taken into account by time averaging the flux during rotation.

$$\langle f_{sw} \rangle = f_{sw} \frac{\int_0^\pi \sin \theta \, d\theta}{2\pi} = \frac{1}{\pi} f_{2D} \tan \alpha. \quad (6)$$

As the 2D growth rate is calibrated to correspond to certain group III material flux, the NW sidewall growth rate can be obtained from equation 6 by replacing the fluxes with growth rates. [92] Based on this consideration the axial growth rate is 22.7 % of the nominal 2D growth rate for a 10 port V80 reactor.

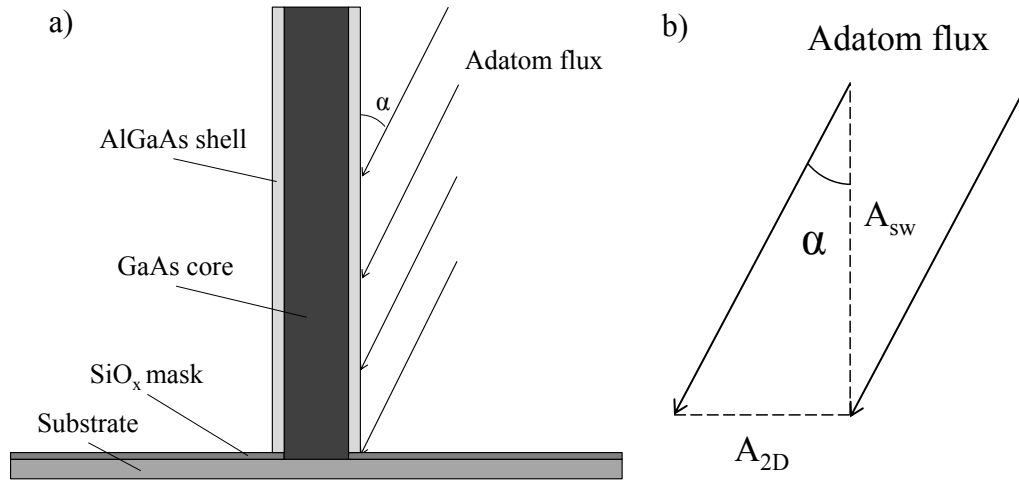


Figure 16. Geometry of NW shell growth is presented in a). Angle α is the incidence angle of the adatom flux to the NW. Angle α is also the tilt angle of the material sources in the MBE reactor. In b) the areas, where the adatom flux hits during 2D growth A_{2D} and sidewall growth A_{sw} are presented.

The cores of the core-shell NWs were grown in lithography-free oxide patterns described in chapter 2.4.4. The density of GaAs nanocrystals forming the holes for the NW nucleation in the SiO_x mask on the template was $1.6 \times 10^8 \text{ cm}^{-2}$. The growth of these structures started by growing the GaAs core as described in the chapter 3.1.2. The core growth duration was 60 min. The axial growth of the core was then terminated by shutting the Ga flux for 10 min under As flux. After the droplet consumption the temperature was reduced from 640 °C to 540 °C. The As flux was increased for the shell growth to correspond V/III flux ratio of 19.0. The shell composition was Al_{0.33}Ga_{0.67}As and the nominal AlGaAs growth rate was 450 nm/h (0.44 ML/s). The GaAs shell was grown by shutting the Al shutter and continuing the growth in the same conditions. The As valve was kept open during the cooling process until the thermocouple temperature reached 300 °C. The shell thicknesses of the two core-shell samples are presented in Table 1. Reference sample without the shell structure is sample 4 presented in the previous chapter of this thesis. It was used to compare the optical properties of the core-shell NWs with similarly grown sample of bare GaAs NWs.

Table 1. Nominal and real thicknesses of the GaAs/AlGaAs core-shell heterostructure NWs are presented with the densities of GaAs crystals in the templates.

Sample	GaAs nano-crystal density of the template ($\cdot 10^8 \text{ cm}^{-2}$)	Nominal thickness of AlGaAs shell (nm)	Nominal thickness of GaAs cap (nm)	Thickness of AlGaAs shell (nm)	Thickness of GaAs cap (nm)
A	1.62	125	25	25	5
B	1.62	50	25	10	5
4	6.28	0	0	0	0

3.2 Characterization

The first two characterization methods presented in this chapter, namely atomic force microscopy (AFM) and scanning electron microscopy (SEM) were mainly used to study the GaAs nanocrystals between the sample growths in order to obtain information for planning the next growths. SEM was also used to characterize the NW properties. X-ray diffraction and photoluminescence spectroscopy were used to characterize the material and optical properties of the NW samples grown before and within the course of this thesis.

3.2.1 Atomic force microscopy

An atomic force microscope (AFM) is a scanning probe microscope that has extremely sharp ($<1 \text{ \AA}$) vertical resolution. Hence, it is used to study surface morphology and roughness. It is also capable of measuring insulating surfaces unlike scanning tunneling microscope (STM) which is used to study not only surface morphology but also the electrical properties of the surface. The operation principle of the AFM is presented in Figure 17. It is based on measuring a force between a very thin tip and the sample surface. The tip is attached to a small cantilever, which is moved with a piezo stack to scan the sample. [114] In this thesis the AFM is used in tapping mode, where the cantilever is oscillated near its resonant frequency above the sample. As the tip moves toward the sample, it is deflected. This affects the resonance of the tip which is measured using a laser beam reflected from the cantilever. The laser beam is detected with a quadrant photodiode where it moves from the upper to lower half as the cantilever oscillates. [115]

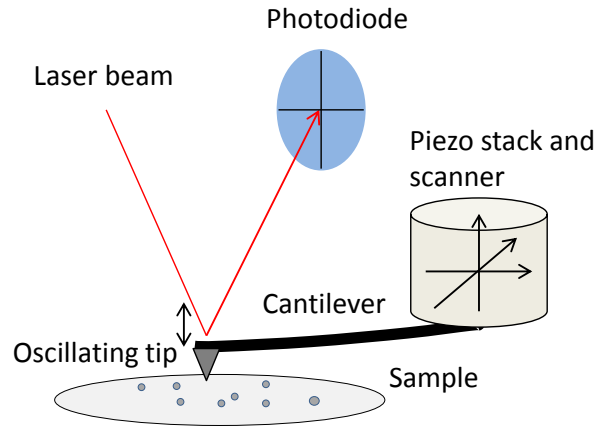


Figure 17. The working operation principle of an AFM in tapping mode which is used in this thesis.

Digital Instruments Veeco Metrology group's Dimension 3100 AFM was used to study substrate surface roughness in order to determine its influence on the droplet density. The microscope was used in the tapping mode. The AFM pictures were analyzed using WSxM software [116].

Three different measurement sets were conducted for surface roughness study. First a set of p-type Si(111) substrates with native oxide, etched with 5 % aqueous HF for different times from 0 s to 10 s, was studied in order to find a correlation between the HF etch time and the surface roughness. A second measurement set consisted of four droplet epitaxy samples grown with different pre-growth annealing temperatures in order to find correlation between the annealing temperature and the surface roughness. Another significant objective was to find relation between the nanocrystal density and the surface roughness. The third set for roughness analysis samples consisted of n-type Si(111) substrates with a 30 nm thermal oxide layer etched in 5 % aqueous HF for various times from 65 s to 130 s.

Furthermore, one droplet epitaxy sample grown on n-type substrate with thermal oxide etched in 5 % aqueous HF for 85 s had two populations of GaAs nanocrystals (sample 19 in table 2). It was also studied with the AFM. The population of the large droplets had density in the desirable range whereas the population of smaller droplets was very dense. An AFM study was conducted to study the possibility that the smaller mounds might be SiO_x instead of GaAs. This was done by etching a piece of this sample in aqueous HF 5% for 85 s and another piece in $\text{HCl}:\text{H}_2\text{O}_2:\text{H}_2\text{O}$ (1:1:1) for 10 s so that the possible SiO_x mounds would have been removed from the first sample and the GaAs nanocrystals from the latter.

Also a droplet epitaxy sample grown in the V90 reactor was scanned in order to compare its surface roughness to the ones measured from samples grown in the 10-2 reactor. This was done in order to study the effect of Sb on the Si(111) surface roughness as the

presence of Sb is known to cause mass transport on 7×7 reconstructed Si(111) surfaces forming 0,3 nm high Si islands and pits. [117] The islands and pits might be adequately large to affect the RSMs obtained from the AFM images.

3.2.2 Scanning electron microscopy

Scanning electron microscope (SEM) uses a focused electron beam to probe the sample surface. The electron beam is created in a heated filament, and accelerated and collimated by electric fields. The beam is scanned over the sample by using scan coils that produce a magnetic field which controls the beam. The electron beam requires vacuum conditions in order to stay collimated. As the electron beam hits the sample, two kinds of electrons are created. These are backscattered and secondary electrons. The backscattered electrons are generated from the scanning electron beam by elastic scattering. The backscattering probability increases with the atomic number of the atoms within the sample. Hence, the backscattered electrons provide sharp elemental composition contrast. The secondary electrons are created by the scanning electron beam, backscattered electrons and other secondary electrons that have enough energy to free electrons from the outermost atomic shells of the sample material and even the structure of the microscope. The secondary electrons created by the scanning electron beam before and after backscattering near the sample surface have sharp contrast on surface details. They are detected with an in-lens detector used for imaging in this thesis [118]. It is located inside the objective lens of the electron gun and hence detects electrons which are created directly on the beam path. As the objective lens of the SEM gathers the electrons to the in-lens detector the distance between sample and objective must be small, less than 5mm but typically 3 mm is used. The SEM used for imaging in this thesis is Carl Zeiss Ultra-55. [118]

SEM images were taken to characterize the GaAs nanocrystal samples. Nanocrystal densities were determined from the SEM images. ImageJ software was used to determine the area in each SEM image based on the pixel size given in information bar of each SEM image. WSxM 5.0 Develop 1.1 software [116] was used to determine the amount of GaAs nanocrystals in the image. The WSxM software is designed for characterizing of scanning probe microscope images but can also qualitatively analyze depth information from grayscale SEM images in Tiff format as it interprets the color scale of the images as height. [116]

Also NW samples were characterized using SEM. All samples were imaged for qualitative analysis of amount of successful NWs, their morphology and parasitic growth. The XRD samples 1-3 grown 5, 20 and 40 min were imaged in 90° angle to calculate the axial and radial growth rates of the NWs and incubation time before of the NW growth.

3.2.3 High resolution x-ray diffraction

X-ray diffraction (XRD) is based on elastic scattering of x-rays. X-rays penetrate the studied crystal lattice and are scattered by atoms at different lattice planes. The scattering angles are treated a lattice plane family at a time. For example, the GaAs(100) lattice planes produce high scattering intensity in a certain angle. When the x-rays scatter from consecutive lattice planes they have to travel different distances inside the studied material. If this difference in the optical paths of the x-rays is a multiple of the x-ray wavelength, the x-rays are in the same phase as they exit the material. This condition produces constructive interference. This is called Bragg reflection and it is schematically illustrated in Figure 18, and mathematically in Equation (7) called Bragg's law. The distance between consecutive lattice planes d_{hkl} can be determined from Bragg's law

$$2d_{hkl} \sin(\theta_B) = n\lambda, \quad (7)$$

where θ_b is the angle of Bragg reflection, λ the x-ray wavelength and n an integer. [119]

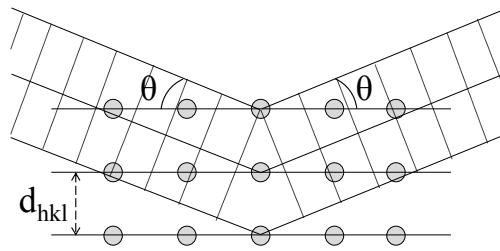


Figure 18. The phase shift between x-rays diffracted from different lattice planes separated by d_{hkl} equals a multiple of wavelengths. Hence constructive interference is observed at the diffraction angle θ . The dashed lines represent wavefronts.

High-resolution x-ray diffraction (HR-XRD) used in this thesis is also based on the Bragg reflection. The differences between HR-XRD and regular XRD are technical. For instance, in Philips PANanalytical X'Pert PRO x-ray diffraction system, which is used in this thesis, a four-crystal germanium single crystalline monochromator produces highly monochromatic x-rays. It produces x-rays from Cu- $K\alpha_1$ -line emission at 1.540593 Å wavelength. Also the angular resolution of the goniometer controlling sample movements is high, 0.0001°. [120]

The XRD spectra measured in this work are lower resolution open detector and high resolution triple-axis omega-2theta (ω -2 θ) scans. In the triple-axis measurement a slit is placed in front of the detector. The open detector scans provide higher intensity whereas the triple-axis measurement enables high angular resolution. The alignment of the x-ray source, the sample and the detector is presented in Figure 19. The angle ω is the angle between the incident beam and the sample. 2 θ is the angle between the incident beam and the detector. In an asymmetric scan the sample is tilted an amount indicated by the

offset and hence the scattering angle is not symmetric with respect to the substrate normal. If the *offset* is zero the scan is called symmetric. Relation

$$\omega = \frac{2\theta}{2} + \textit{offset} \quad (8)$$

links the angles. Triple-axis ω - 2θ scan enables scanning of multiple adjacent Bragg diffraction peaks with high resolution. Hence WZ and ZB reflections can be separated more accurately from the XRD-spectra obtained this way. [119]

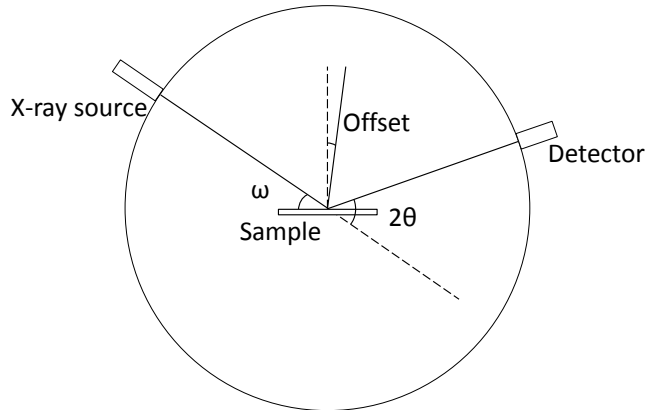


Figure 19. The x-ray source and detector are mounted on a perimeter of a goniometer circle. The sample is mounted on a rotating cradle in the middle of the circle. During ω - 2θ scan the detector moves along the circles perimeter with twice the angular velocity of the sample rotation.

Presenting the Bragg diffraction as a momentum transfer of the x-rays is convenient in order to understand the reciprocal space maps (RSMs), which are used to further study the crystalline structure of the NWs. This representation is illustrated in Figure 20. The incident beam wave vector k_{inc} determines the Ewald sphere so that k_{inc} originates in the center of the sphere and its length determines the sphere radius. Also the diffracted beam wave vector k_{diff} is set end to the perimeter of the Ewald sphere. The momentum transfer between these two wave vectors is described by vector $\mathbf{Q} = \mathbf{Q}_y + \mathbf{Q}_x$. The momentum transfer in direction of the sample normal is denoted by Q_y and parallel to the sample by Q_x . The \mathbf{Q} vector is originated in the origin of reciprocal space of the studied material. Diffraction occurs when it hits a reciprocal lattice point \mathbf{h} as illustrated in Figure 20.

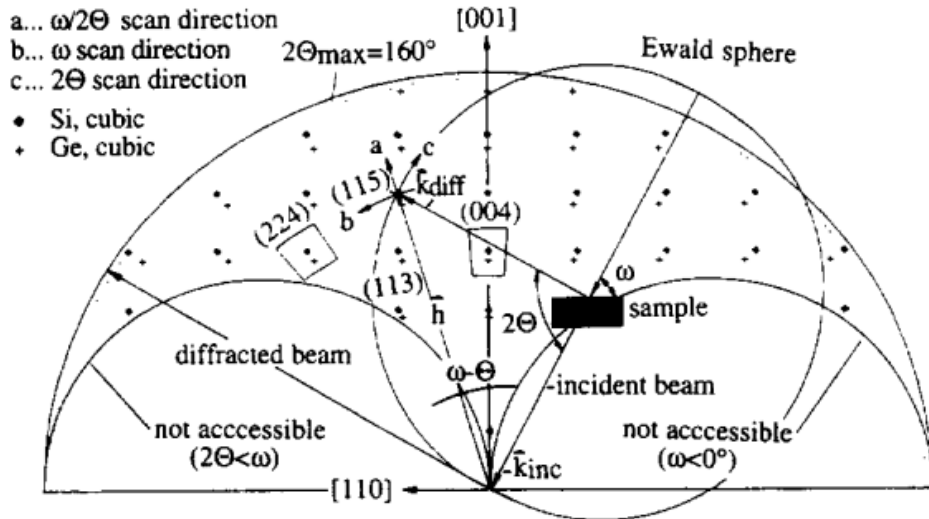


Figure 20. Reciprocal lattice points of a relaxed Si/Ge crystal on (001) direction are combined with the (Q_x, Q_y) plane. The range of visible reciprocal lattice points is determined by the radius of the Ewald sphere. The two lower semicircles are not accessible due to incident or diffracted beam ending up to a transmission region. The ω - 2θ , ω and 2θ scans are illustrated by a, b and c respectively. [121]

An ω or rocking curve scan is obtained by scanning ω while holding 2θ as a constant. This creates an arc with origin at $(Q_x, Q_y) = (0, 0)$ and radius $|\mathbf{Q}|$. An arc of Ewald sphere can be scanned by changing 2θ . The combination of these two is an ω - 2θ scan which is used in this thesis. It scans a straight line pointing away from the origin of the reciprocal space. In an asymmetric ω - 2θ scan the *offset* determines the scan direction in the reciprocal space. In the ω - 2θ scanning procedure, 2θ changes $2\Delta\omega$ when ω changes $\Delta\omega$. Hence, the *offset* remains constant. A scan along the Q_y axis is a symmetric ω - 2θ scan obtained using zero *offset*. All these scans are presented in Figure 20. The ω and ω - 2θ scans are presented in the RSM of Figure 21.

A RSM is created by conducting various ω - 2θ scans with different *offset* values. A RSM of a Si(111) reciprocal lattice point is illustrated in Figure 21. An area of RSM is illustrated as small regions around (004) and (224) reciprocal lattice points in Figure 20. RSMs enable studying of the x-ray momentum transfer in the direction of the sample surface and the surface normal using the same graph. Hence, avoiding distortions in obtained lattice constant values caused by wrong *offset* value is possible using RSMs. [119]

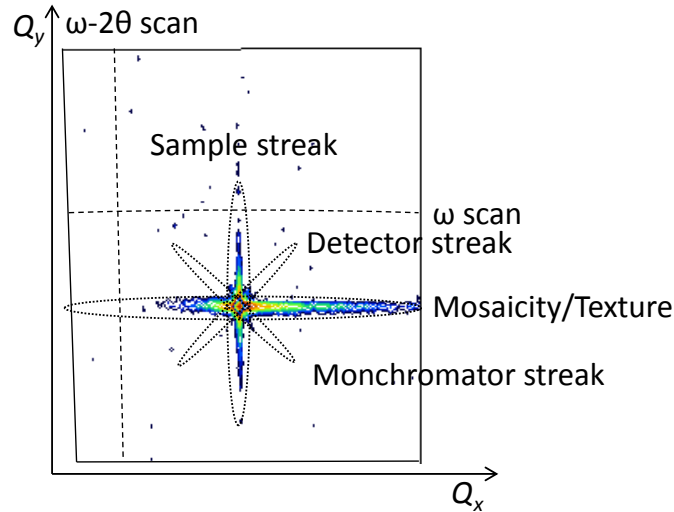


Figure 21. Reciprocal map of Si(111) reflection with dashed lines marking $\omega-2\theta$ and ω scans. Notice that the $\omega-2\theta$ scan is not parallel to Q_y axis and the ω scan is a curve, not a straight line. The shape of the Bragg peak consists of mosaicity and sample, detector and monochromator streaks marked with ovals.

The Bragg peaks measured in this work [Si(111), ZB GaAs(111) and WZ GaAs(0002)] are parallel to the Si(111) direction of the substrate. Hence symmetric $\omega-2\theta$ scans should be adequate to analyze the ZB and WZ GaAs lattice parameters. However, the parallelism may be broken by substrate bending or directional imperfection, sample alignment, mounting or mosaicity of the NWs. Mosaicity means small (\leq few 0.1°) variations in the directions of the lattice planes. Larger variations are referred as texture. In case of NWs it means that the NWs are slightly tilted in different directions. Hence, the in-plane component of the momentum transfer is denoted by Q_x is also important. [119]

Equation

$$Q_y = R[\sin \omega + \sin(2\theta - \omega)] = \frac{\lambda}{2d_{hkl}}, \quad (9)$$

where R is the radius of Ewald sphere (0.5) and λ is the x-ray wavelength, is used to transform the instrumental ω and 2θ into Q_y . This equation is used in X'pert Epitaxy software used to analyze the RSMs. Usually, $R=k/\lambda$ form, where k is some constant is used [119] Also, the distance between consecutive lattice planes d_{hkl} in the direction of the sample normal is obtained from equation 9.

NW samples 1-4 were characterized using open detector and triple-axis $\omega-2\theta$ scans and RSMs. NW samples 1-3 had crystallized Ga droplets whereas the droplets of sample 4 were preserved during the growth. The droplet crystallization is supposed to create ZB-WZ stacking faults as the V/III ratio varies. Hence, visible WZ reflection is expected to be seen in samples 1-3 but not in sample 4 [122; 123].

Also the WZ GaAs lattice constant c is determined. The distance between the WZ(0002) lattice planes d_{hkl} is obtained from Equations 7 and 9 using measured XRD spectra or

RSMs. In the hexagonal structure the lattice constants a and c are obtained from equation

$$\frac{1}{d_{hkl}^2} = \frac{4}{3} \left(\frac{h^2 + hk + k^2}{a^2} \right) + \frac{l^2}{c^2}, \quad (10)$$

where d_{hkl} is the distance between lattice planes and $(hkil)$ is converted into (hkl) using

$$i = -(h + k). \quad (11)$$

Equation 11 is obtained from the symmetry of the $(000l)$ -planes of the hexagonal structure. For cubic structures the lattice constant a is obtained using equation [119]

$$\frac{1}{d_{hkl}^2} = \frac{h^2 + k^2 + l^2}{a^2}. \quad (12)$$

3.2.4 Photoluminescence spectroscopy

The basic theory of photoluminescence (PL) spectroscopy is presented in Chapter 2.6. Two PL measurement setups were used within the course of this thesis. A commercial Accent RPM2000 PL mapper was used for room temperature PL measurements. A micro-photoluminescence (μ -PL) setup was used for temperature and power dependent PL measurements. Also the photonic properties of core-shell NWs were investigated using the μ -PL setup.

In the μ -PL setup the sample was cooled with a liquid helium cryostat in vacuum. A heater controlled the sample temperature. The PL emission was detected using a Peltier cooled 2D CCD detector. The 2D detector enables creating spectral images. The PL light enters the monochromator through a narrow (100 μ m) slit. The axis along the slit is the y-axis of the spectral image. In the monochromator the light is reflected by a grating which disperses it into a spectrum. This spectrum hits the 2D detector forming the x-axis of the spectral image. In order to locate NWs on the sample the monochromator slit can be widened and the grating replaced by a mirror. This creates a 2D image of the sample surface. A xyz-piezo stage controls the sample location in x-y direction and the focus in z-direction.

The power and temperature dependent μ -PL measurements were conducted using as-grown samples 1-4 with standing NWs still attached to the Si(111) substrates. Growth of these samples is presented in chapter 3.1.2. Spectra from individual NWs was obtained by cropping small areas in y-direction of the detector. NWs were excited using 640 nm pulsed (80 MHz) laser excitation. Maximum output power of the laser was 9.5 mW. The excitation laser spot diameter was 20 μ m. One spot of each sample with several NWs cropped in y-direction was measured. 300 μ W excitation power was used for the temperature dependent measurements.

4. RESULTS AND DISCUSSION

This chapter presents the results of this thesis. First sub-chapter presents the growth of the GaAs nanocrystals along with characterization using AFM and SEM. After this, the growth of the NWs is presented. The NW characterization is divided into four sub-sections. The HR-XRD analysis is discussed in the first sub-section presenting the open detector and the triple-axis scans alongside with the RSMs. The room temperature PL measurements of the bare and the core-shell NWs are then discussed. The μ -PL measurements of the bare GaAs NWS and the GaAs/AlGaAs core-shell NWs are presented in the last two sub-sections.

4.1 GaAs nanocrystals

The GaAs droplet epitaxy samples grown within the course of this thesis are presented in Table 2 in chronologic order along with the growth parameters. These include the substrate type, the pre-growth treatments, the *in situ* annealing temperature and the Ga deposition temperature. Samples 1-19 are grown in the 10-2 reactor and samples 20-22 are grown in the V90 MBE reactor. The nanocrystal densities of the samples grown in the 10-2 and V90 reactors are presented graphically in Figures 22 and 26, respectively. The sample holders were chemically cleaned before growth of sample 5. Samples 19, 21 and 22 have two nanocrystal populations and the given density is the density of the larger nanocrystals.

Table 2. Droplet epitaxy samples grown within the scope of this thesis. The substrates used for the growth were either p- or n-type doped, and some of them had a protecting thermal grown oxide (TO), which was removed prior to growth. Furthermore, the pre-growth chemical treatment, pre-growth annealing and Ga deposition temperatures, GaAs coverage (θ) in nanometers of corresponding planar growth and GaAs nanocrystal density are given for each sample. The samples with nanocrystal densities in desirable range are bolded and the first growths of the day are italicized. Samples 1-19 are grown in the 10-2 reactor and samples 20-22 in the V90 reactor.

Sample number	Substrate type	Reactor	Pre-growth chemical treatment	Annealing T (°C)	Ga deposition T (°C)	θ (nm)	Droplet density ($\cdot 10^8 \text{ cm}^{-2}$)
1	p	10-2	10s HF dip	640	545	0.19	28.3
2	p	10-2	10s HF dip	665	545	0.19	6.28
3	p	10-2	10s HF dip	600	545	0.19	52.5
4	p	10-2	10s HF dip	545	545	0.19	61.1
5	<i>p</i>	<i>10-2</i>	<i>5 s HF dip</i>	<i>640</i>	<i>545</i>	<i>0.19</i>	<i>10.9</i>
6	p	10-2	10s HF dip	640	545	0.19	29.4
7	p	10-2	10s HF dip	640	545	0.19	23.3
8	p, TO	10-2	85 s + 5 s HF dip	640	545	0.19	1.53
9	p	10-2	Piranha + RCA1	640	545	0.19	13.2
10	p	10-2	RCA1	640	545	0.19	19.5
11	p, TO	10-2	85 s + 5 s HF dip	640	570	0.19	1.50
12	p, TO	10-2	85 s + 5 s HF dip	640	520	0.19	35.1
13	p, TO	10-2	85 s + 5 s HF dip	640	545	0.09	28.3
14	p	10-2	10s HF dip	700	545	0.19	2.77
15	p	10-2	10s HF dip	715	545	0.19	18.4
16	p, TO	10-2	85 s + 5 s HF dip	715	545	0.19	28.4
17	n	10-2	10s HF dip	700	545	0.19	17.2
18	n	10-2	10s HF dip	715	545	0.19	6.85
19	n, TO	10-2	85 s + 5 s HF dip	700	545	0.19	0.409
20	p	V90	10s HF dip	671	552	0.19	0.219
21	p	V90	10s HF dip	685	505	0.19	0.734
22	p	V90	10s HF dip	672	480	0.19	1.398

Initially the surface roughness was suspected to be the reason for the high nanocrystal densities of samples 1-4 because the pre-growth heat treatment temperature had an effect on the density as seen in the trend line marked in Figure 22. The high temperature annealing is known to alter the Si surface reconstruction which may lead to smoothening of initially rough surface. [113]

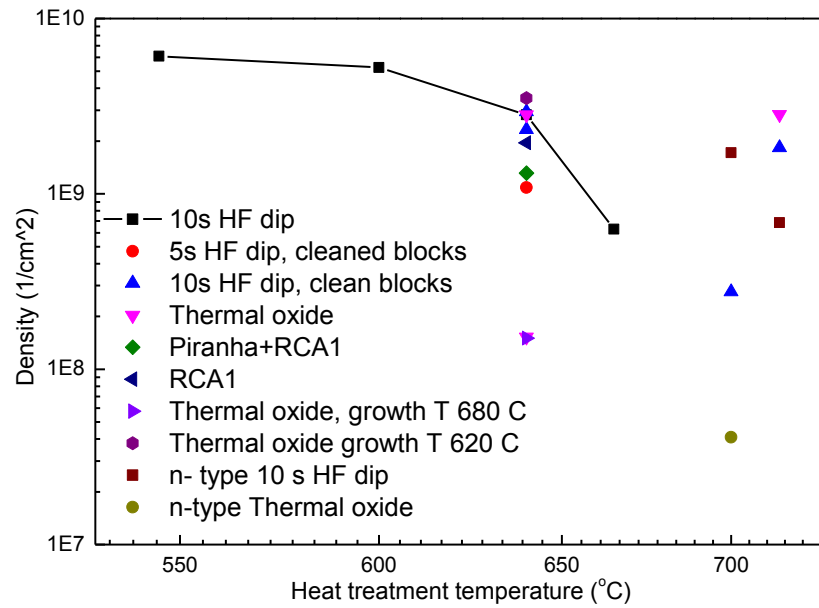


Figure 22. Droplet densities of the samples grown in the 10-2 reactor are presented as a function of pre-growth annealing temperature. The first growth series is connected with a line to illustrate the effect of the annealing temperature. These samples were grown on same kind of substrates in similar conditions. Also the pre-growth treatment and the substrate type are presented.

Because the effect of the heat treatment temperature affected the nanocrystal densities, the surface roughness of p-type Si(111) substrates was studied as a function of the HF (5%) etch duration using AFM. The results are shown in Figure 23. As seen in Figure 23 the results are scattered and roughness shows no dependence of the HF etch duration. The exceptionally low value of roughness for 2 s HF dip is due to low resolution image caused by resonance disturbance from control unit of the AFM. Furthermore, the resonance probably partially dulled the AFM tip inducing lower resolution images for longer etch times. Therefore, no correlation between the HF etch duration and the root mean square (RMS) roughness of the p-type Si(111) surface could be detected with the AFM.

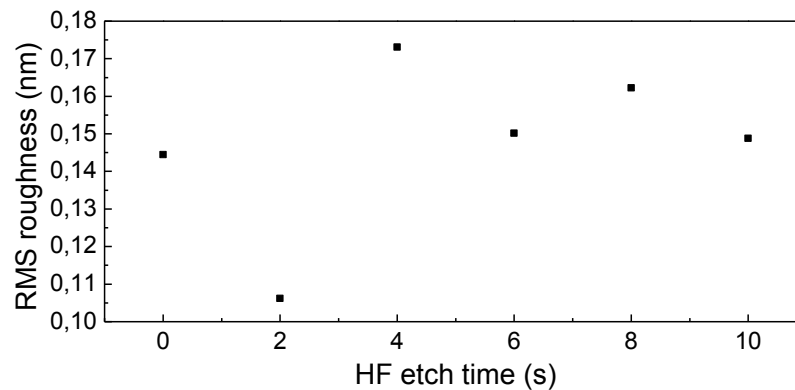


Figure 23. RMS roughness of p-doped Si(111) surface presented as a function of the HF (5%) etch duration.

As the HF dip duration did not affect the surface roughness the DE samples 1-4 were measured with the AFM in order to see the effect of the pre-growth annealing temperature on the surface roughness. Later sample 20 grown in the V90 reactor was measured similarly in order to study the effect of possible Sb contamination in the 10-2 reactor considered later in this chapter. The evidence of relation between the annealing temperature and the surface roughness was small but detectable as presented in Figure 24 a). Also the droplet density showed clear dependence of the RMS roughness as illustrated in Figure 24 b). Based on this result higher pre-growth annealing temperatures were favored in the latter growths starting from sample 14.

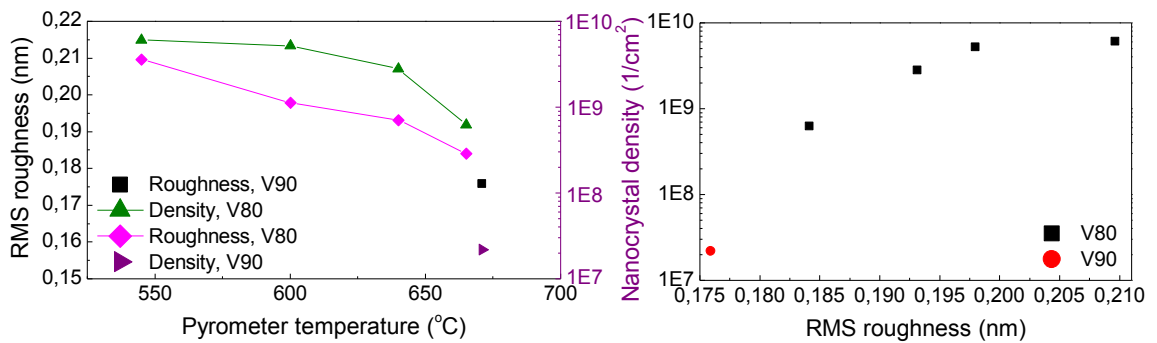


Figure 24. Surface RMS roughness and GaAs nanocrystal densities of samples 1-4 and 20 are presented as a function of heat treatment temperature in a). In b) the dependence between the surface roughness and nanocrystal density is illustrated.

In addition to annealing temperatures also different Si(111) surface and pre-growth treatments were tested with a growth series of samples 8-10. Sample 8 had nanocrystal density in the targeted range. It was grown on n-type Si(111) substrate covered in thermal grown oxide and etched in 5 % aqueous HF for 85 s in cleanroom and 5 s just before loading to the reactor. The two other surface treatment methods, piranha and RCA1 cleaning [112] conducted on p-type Si(111) substrates with no thermal oxide did not reduce the nanocrystal density. Hence, they were not further studied and an AFM study of HF etch times' effect on the Si(111) surface covered in thermal grown oxide was conducted. The measurements of the n-type Si(111) substrates with a 30 nm thermal oxide etched for 65 s to 130 s in 5 % aqueous HF solution showed no relationship between the surface roughness and the HF treatment duration as presented in Figure 25. The RMS roughnesses were typically under 0.2 nm and there were no objects to use for focusing the AFM. Hence, the resolution of the images varied significantly. Analysis with WSxM software [116] showed that lower resolution images led to higher values of roughness. Still it can be concluded that different HF etch times do not cause large surface roughness variations. However, the surface roughnesses were higher compared to the ones obtained for the p-type substrates with no thermal oxide (Figure 23). This is either caused by the slightly dulled tip used to measure the p-type substrates or surface roughening caused by the thermal grown oxide.

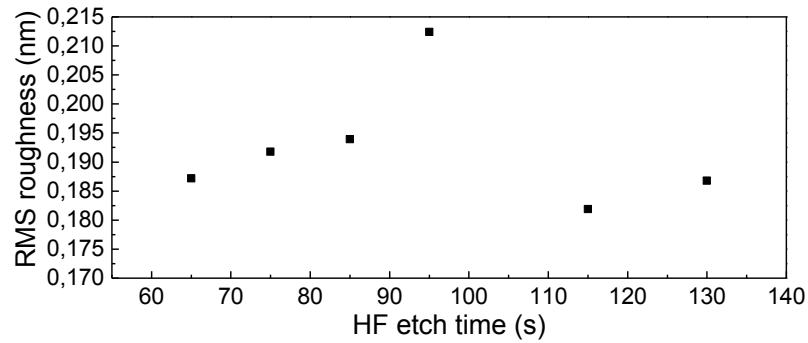


Figure 25. Roughness of *n*-type Si(111) substrates with 30 nm thermal oxide presented as a function of HF (5%) etch time.

When more samples were grown a remarkable trend within the days' growth series was found. All of the samples from 10-2 reactor with desirable nanocrystal density (the bolded samples in table 2) have been grown as first growths of the day, in the same sample holder except for sample 18. It should be noted that sample 5 is not comparable to the other samples because of the short 5 s HF etch time. The hydrophilicity of the substrate after HF etch suggested that the native oxide had not been completely removed. Hence, it can also be stated that all of the samples grown as the first growths of the day had nanocrystal density in the desirable range as long as the pre-growth chemical treatment had succeeded in removing the oxide from the substrate surface. In some cases, the first samples of the day were degassed overnight in 275 °C in the preparation chamber of the reactor. However, this is not the case for all of them and no data of sample loading or degassing times in the preparation chamber times exists. However, some of the substrates were loaded in the morning just before growths excluding the possibility of slow evaporation of some crucial impurity.

A possible explanation for superiority of the first samples of the day is the arsenic background pressure left from the crystallization of the first sample. The growth chamber was typically in pressure range of 10^{-9} or 10^{-10} mbar in the morning and in 10^{-8} mbar range while loading the second and third samples of the day. As_4 is known to form a stable and passive Si(111)As: 1x1 surface with no dangling bonds in temperatures corresponding to the idle temperature of the 10-2 reactor's manipulator. Removing of the As monolayer from the Si(111) surfaces requires annealing in temperatures over 700 °C. [124] This temperature may differ from 10-2 and V90 reactors' pyrometers with over 20 °C because they use GaAs emissivity value whereas pyrometers used for publications concerning Si surfaces probably use Si emissivity. If the background pressure has been adequate As source for formation of the monolayer it most likely has been present in all of the growths. However, the presence of the passivation layer cannot be confirmed and its' effect on the droplet epitaxy process is not known. Also phosphorus is known to act similarly to As on the Si(111) surface [125]. Based on [129] the presence of N passivation layer increases the Ga droplet densities significantly. If As and P have similar effect on Ga droplet epitaxy the surface passivation is a plausible cause for the unsuc-

cessful second and third growths of the day. If the As or P coverage would emerge from the sample holder and the manipulator its' effect would be seen in all of the growths, also in the V90 reactor. Based on this the possible As source is the background pressure, not contamination of the sample holders and the manipulator. In addition the sample holder cleaning before sample 5 did not have a clear effect on the nanocrystal densities.

As shown in Figure 26, the GaAs nanocrystal densities of the samples grown in the V90 reactor depend exponentially on the Ga deposition temperature which is expected due to the thermally activated Ga adatom diffusion [30]. This predicts good repeatability which was further confirmed in growths that are not included in this thesis. Different sample holders (also 3x2" sample holders), various pre-growth annealing and Ga deposition temperatures were tested in these growths. The droplet densities obtained in were consistent with the results presented in the Figure 26. Furthermore, nanocrystal densities showed no dependence on the sequence of growths of the day. These observations make the effect of the As background pressure very questionable.

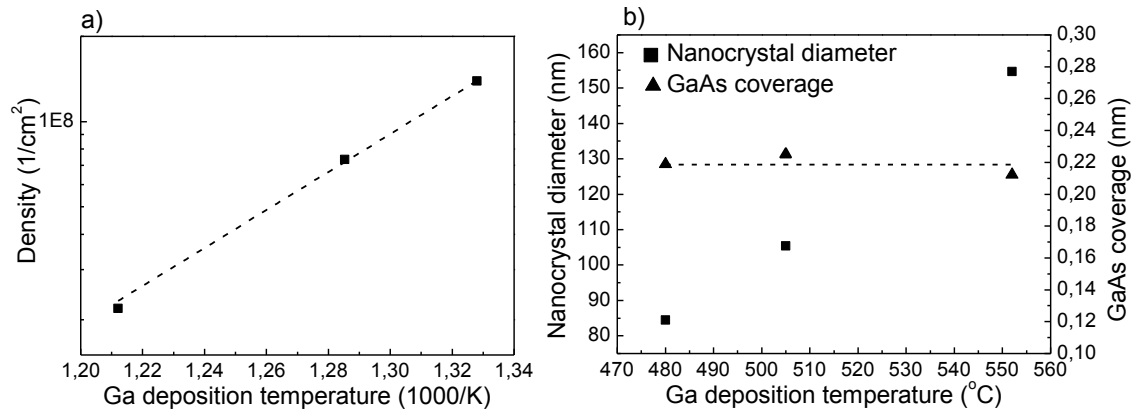


Figure 26. a) Arrhenius plot of GaAs nanocrystal densities as a function of Ga deposition temperature for samples 20-22 grown in the V90 reactor. The dashed line is an exponential fit of the data. b) The dependence of nanocrystal diameter and estimated GaAs coverage on the Ga deposition temperature.

The nanocrystal density follows an exponential law

$$\rho(T) \propto e^{\frac{E_a}{k_B T}}, \quad (13)$$

where E_a is thermal activation energy, k_B is the Boltzmann constant $8,617 \cdot 10^{-5}$ eV/K and T is the Ga deposition temperature. [126] The activation energy obtained from the fit on the droplet densities in the samples 20-22 is 1.3 eV, whereas the activation energy for Si(100) surface used in [126] is only 0.22 eV. Even though the different surfaces are not straightforwardly comparable, the larger activation energy explains why our droplet epitaxy process requires higher temperatures than in [57]. The activation energy might be related to the effect of group V presence on the substrate surface during the Ga droplet deposition. Even though the droplet densities are significantly reduced by growth in

the V90 reactor they are still higher than in [126]. This improvement in the nanocrystal density and its' exponential dependence on the Ga deposition temperature suggests that the Sb contamination in the 10-2 reactor has indeed been detrimental to the droplet epitaxy procedure. This is further confirmed by the surfactant effect of Sb. The presence of Sb is known to induce growth of smaller and denser quantum dots on GaAs surfaces. It also suppresses three-dimensional growth on Si surfaces. [127] The latter is explained by the motion of Si(111) surface that forms bi-layer thick Si islands and pits under the presence of Sb. [117] Initially sample holders and manipulator were suspected to form the source of Sb in the 10-2 reactor. However, the effect of Sb would also be seen in the first growths of the day if the contamination source was the manipulator. Also, the cleaning of sample holders before sample 5 did not affect the nanocrystal densities. After the growths in the V90 reactor the major source of the Sb contamination in the 10-2 reactor during the growths was found to be the Sb cracker itself. In addition to Sb needle valve the Sb flux can be blocked by a manual shutter which was not used during the growths because no apparent Sb leakage had been noticed before. However, closing the Sb shutter was found to reduce the base pressure of the growth chamber up to 9 % when all the cells were in their idle temperatures indicating a minor Sb leak into the growth chamber. The effect of Sb is further supported by the substrate smoothening observed in the AFM measurements (Figure 24). As the pre-growth annealing temperature is increased smoother surfaces and lower nanocrystal densities are obtained. Furthermore, a discontinuity in this trend is found between the samples grown in the 10-2 and V90 reactors. The surface of the sample grown in V90 reactor was found to be significantly smoother than the ones grown in 10-2 reactor. This is expected as the presence of Sb on Si(111) surface is known to induce Si mass transport and surface roughening. [117]

In addition to the nanocrystal densities also their diameters were studied from the SEM images of samples grown in the V90 reactor. The nanocrystal diameters show almost linear dependence on the Ga deposition temperature as seen in Figure 26 b). As the nanocrystal density decreases their size increases. Their volume was estimated by approximating the nanocrystals as hemispheres. By multiplying the estimated nanocrystal volume with their density an estimation of GaAs coverage θ is obtained [Figure 26 b)]. The obtained GaAs coverage corresponds to 0.22 nm of 2D GaAs growth on GaAs(100) surface. The value of GaAs coverage is close to the nominal coverage 0.19 nm. This means that the Ga amount in the nanocrystals remains constant in different temperatures and no Ga desorption occurs in the temperature range used for Ga deposition.

The effect of the nanocrystal crystallization temperature should be also considered. Our nanocrystals are crystallized in Ga deposition temperature whereas in [57; 72; 126] they are crystallized in 150 °C. The reduced nanocrystal densities in the samples grown in the V90 reactor show, that the crystallization temperature is not the factor causing the inconsistency in the nanocrystal densities in the samples grown in the 10-2 reactor. However, it might still affect the densities as the samples grown in the V90 reactor ex-

hibit higher densities as presented in [57; 72; 126]. The crystallization temperature might also be the reason for the bimodal nanocrystal size distributions found in samples 19, 21 and 22 [Figures y+3 and k b)]. All samples with bimodal size distributions have small nanocrystal densities. However, not all samples with small densities (sample 20) have bimodal size distribution. The low crystallization temperature could prevent the formation of the bimodal size distribution by preventing the Ga diffusion between droplets during the crystallization. Another plausible reason for the bimodal size distributions is the effect of As or P on the Si(111) surface. Additional AFM studies were conducted for sample 19 with bimodal size distribution. One piece of the sample was etched in HCl:H₂O₂:H₂O in order to remove GaAs and other in HF 5% in order to exclude the possibility that smaller mounds were SiO_x instead of GaAs. Flattened and contrast modified AFM image of the sample 19 after etch in HF 5% for 10 s is presented in Figure 27. It shows that the smaller mounds are preserved and hence the possibility that they consist of SiO_x is excluded. The HCl:H₂O₂:H₂O etch removed all mounds from the substrate showing that they are GaAs. Also the hexagonal shape and triangular top facet of the larger crystal can also be.

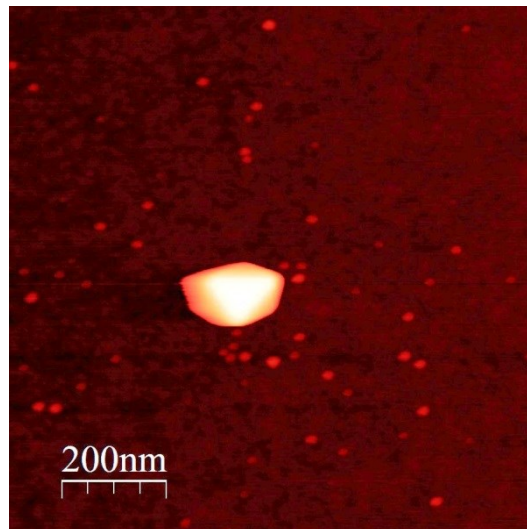


Figure 27. An AFM image of DE sample 19 etched in 5 % HF solution for 85 s shows two nanocrystal populations. The contrast of the image is modified.

The shape of the nanocrystals was studied using the SEM images. The nanocrystals in high density samples are typically oval [Figure 28 c)], whereas the nanocrystals in samples with appropriate densities [Figure 27 and Figure 28 a) and b)] have typically more symmetric hexagonal crystals. Initially high crystallization temperature compared to [57; 72; 126] was considered a possible explanation for the different nanocrystal shapes. The smallest density where most nanocrystals seem to be oval is $6.85 \cdot 10^8 \text{ cm}^{-2}$ of sample 18. However, oval shaped nanocrystals are also present in less dense samples as seen in Figure 28 c). The small nanocrystal size is a plausible cause for the oval shape of the nanocrystals as larger nanocrystals are typically hexagonal, whereas smaller nanocrystals are elongated hexagons and the smallest nanocrystals found in samples

with bimodal size distribution are triangular [Figure 28 b)]. The nanocrystal size is known to affect the faceting of the crystals and hence possibly their shape [128]. The effect of nanocrystal size was tested by growing a sample with small density of small nanocrystals in the V90 reactor by depositing significantly smaller amount of Ga on the substrate before crystallization. This sample is not presented in this thesis but the nanocrystals are elongated hexagons indicating that the shape of the nanocrystals is size dependent.

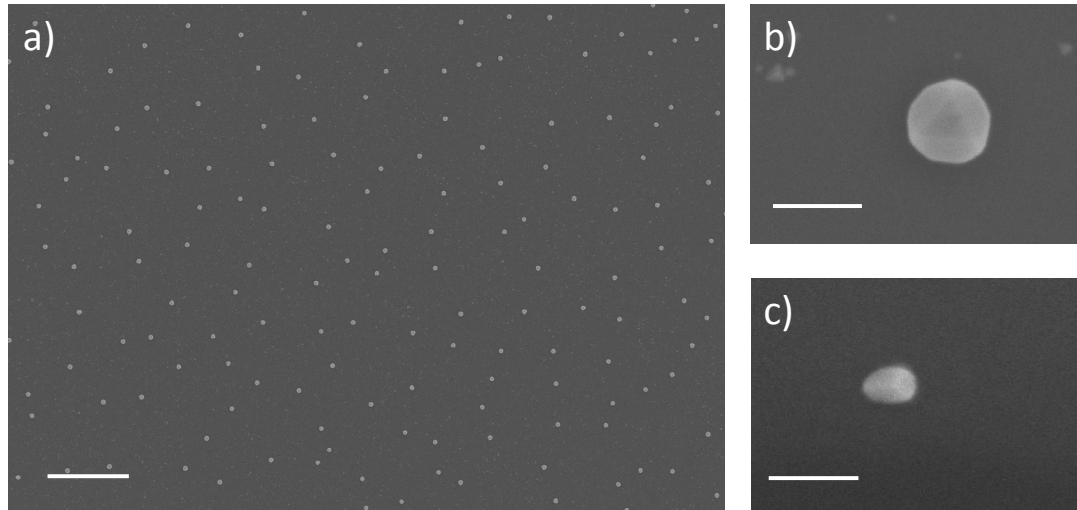


Figure 28. Typical SEM image in a) is a typical image in determination of droplet densities. Images of single nanocrystals in b) and c) illustrate the symmetric and oval shapes of the nanocrystals. Also the bimodal size distributions can be seen in a) and b). Images a) and b) are from sample 21 and c) from sample 14. Scale bars are in a) 2 μm and 100 nm in b) and c) 20 nm.

4.2 Nanowires

Top-view and tilted SEM images of the NW sample 4, for which the growth duration was 60 min, are presented in Figure 29. The average length of the NWs was 4.36 μm and width 140 nm as determined from the SEM images. The NWs are vertical and grown with high yield as qualitatively seen on the SEM images. Although, some tilted NWs are observed. The heights and widths of the NWs seem to be homogeneous which is expected in the NW growth on lithography free oxide patterns on Si(111) surface [8]. On the bare Si surface also some parasitic growth is observed. Its amount is similar to growths on Si(111) surface covered in native oxide [69; 83] and small compared to droplet epitaxy based growth method on a Si(111) substrate with no oxide layer [69; 72].

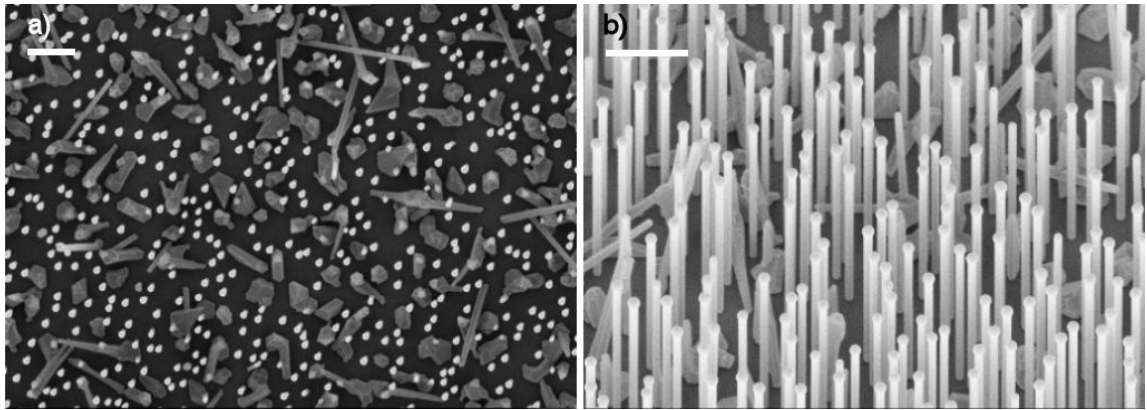


Figure 29. A top-view a) and 30 °C tilted b) SEM images of the NW sample grown for this thesis (XRD sample 4). The scale bars correspond to 1 μm .

The axial and radial growth rates of NWs were determined from the data in Figure 30 presenting cross-sectional SEM images of NW samples 1-3, for which the growth duration was 5 min, 20 min and 40 min respectively. No Ga droplets are observed on the ends of the NWs because they were consumed by exposing the NWs to As flux after the NW growth. The axial growth rate was 5.34 $\mu\text{m}/\text{h}$ (89.0 nm/min) and the radial growth rate 2.2 nm/min. The incubation time before the NW growth beginning was 68 s. The growth rate differs from the sample 4 that had growth rate 4.36 $\mu\text{m}/\text{h}$. The samples 1-3 were grown on 1/6 of a 2" droplet epitaxy template whereas sample 4 was grown on a whole 2" template. This causes slight differences in the temperature distribution along the sample which might affect the NW growth rate. However, slightly different As flux is a more probable cause for smaller growth rate of sample 4 because the group V flux is the parameter affecting most on the NW growth rate and the reactor's ion gauge used for flux measurements was not completely reliable during the time of the growth of the sample 4. [66; 71] Also the droplet crystallization lengthens the NWs causing higher growth rate values for samples 1-3.

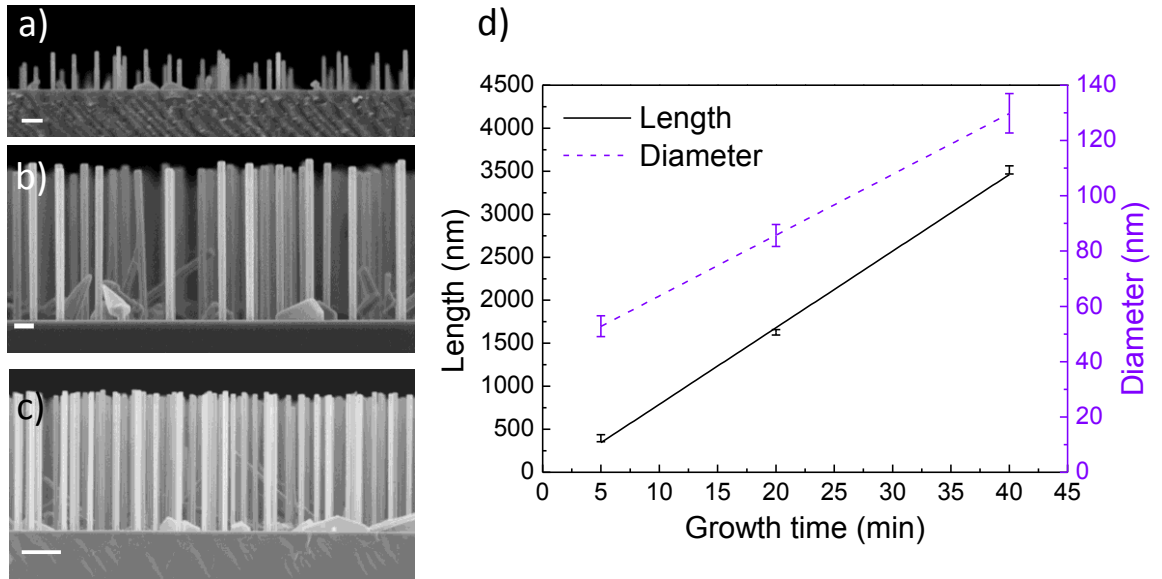


Figure 30. Cross-sectional SEM images of NWs grown for 5 min, 20 min and 40 min are presented in a) to c) respectively. The scale bars correspond to 200 nm in a) and b) and 1 μm in c). Average values of NW length and diameter are obtained from 20 to 50 NWs using cross sectional SEM images. The data is presented as a function of the growth duration in d) with standard deviation and linear fits.

4.2.1 X-ray diffraction

Theoretical diffraction angles for Si(111) surface and for ZB(111) and WZ(0002) GaAs are calculated using equations 7, 10 and 12 and presented in table 3. Si and ZB GaAs lattice constants are taken from [11]. The WZ GaAs lattice constant c varied significantly depending on a source and the manner it had been obtained. Maximum and minimum values that were found are 6.67845 \AA [130] and 6.407 \AA [131], respectively. These values are obtained using different computational methods. According to more recent studies where NW XRD has been measured the WZ lattice constant is found to be greater than the ZB lattice constant [122; 123].

Table 3. Calculated x-ray diffraction angles in NW growth direction for Si(111), ZB and WZ GaAs for maximum and minimum lattice constant values.

Material	Si	ZB GaAs	WZ GaAs max. c	WZ GaAs min. c
Lattice constant (\AA)	5,431	5,65325	6,67845	6,4070
h k l	1 1 1	1 1 1	0 0 2	0 0 2
d_{hkl}	3.13559	3.26391	3.33923	3.20350
Diffraction angle ω -2 θ (deg)	14.22098	13.65084	13.33718	13.913376

The lower resolution open detector XRD ω -2 θ curves of samples 1 to 4 are presented alongside with an open detector RSM of sample 4 in Figure 31. The ZB and WZ diffractions can be clearly separated in the curves of samples 1, 2 and 3. Based on this data

the GaAs peaks seem to shift with respect to the Si reflection. Also the Si reflection is broadened in the spectra of samples 2 and 3. This is probably caused by the significant peak broadening seen in RSM in Figure 31 b), where extremely broad detector streak is seen in the Si(111) reflection. If the curves are optimized to different ω values the distance between the broad GaAs peak and Si(111) peak changes.

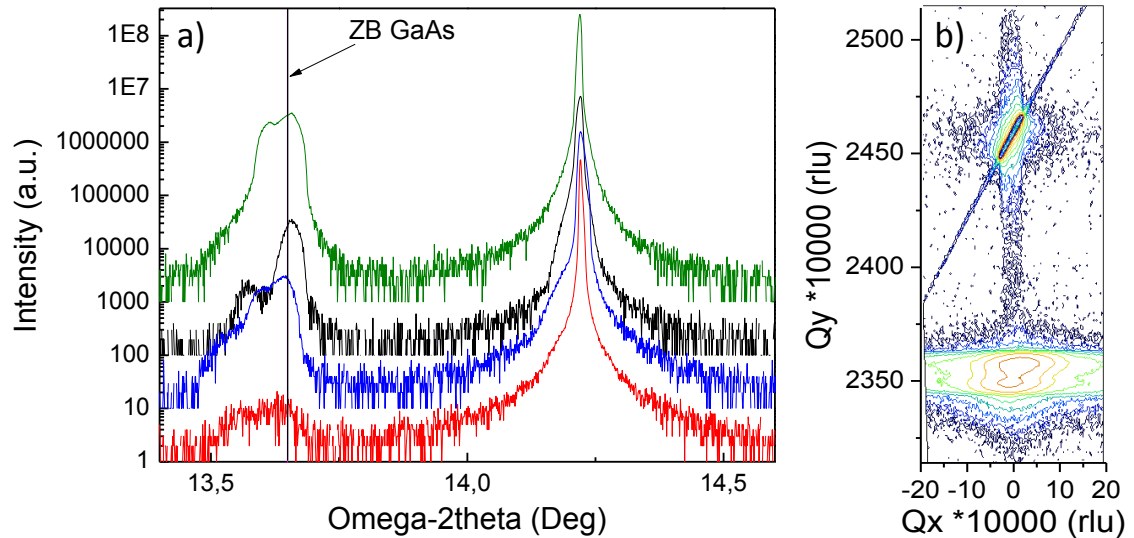


Figure 31. Open detector X-ray diffraction curves for samples 1 to 4 are presented in a) from bottom to top respectively. Also ZB GaAs diffraction angle according to [11] is marked. The intensity scale is logarithmic and spectra have been offset by factor of ten. Open detector RSM of sample 4 is seen in b). The detector streak broadens the Si(111) peak significantly.

Triple-axis measurements provide higher angular resolution with the expense of the intensity. As shown in Figure 32, ZB GaAs XRD peaks are exactly at the same angle for all samples, unlike in the measurements performed with the open detector (Figure 31). The diffraction angles are also consistent with the theoretical values of ZB GaAs lattice constant. Due to the weaker intensities compared to the open detector measurement, only small indications of WZ phases were found. A small separate peak can be seen in the curves of samples 2 and 3 in Figure 32. This is associated with WZ segments that are long enough to adopt the WZ lattice constant. Another indication of WZ is the broadening of the ZB GaAs peak to the WZ side of the peak. This broadening is on similar level in all of the curves and also seen in the RSMs in Figure 33. The broadening is probably related to stacking faults and other extremely narrow WZ segments that only slightly affect the lattice constant of almost phase pure ZB NWs [12; 123]. Also almost no GaAs peak is observed from NWs in the sample 1. Hence, determination of the WZ lattice constant was impossible based on these measurements.

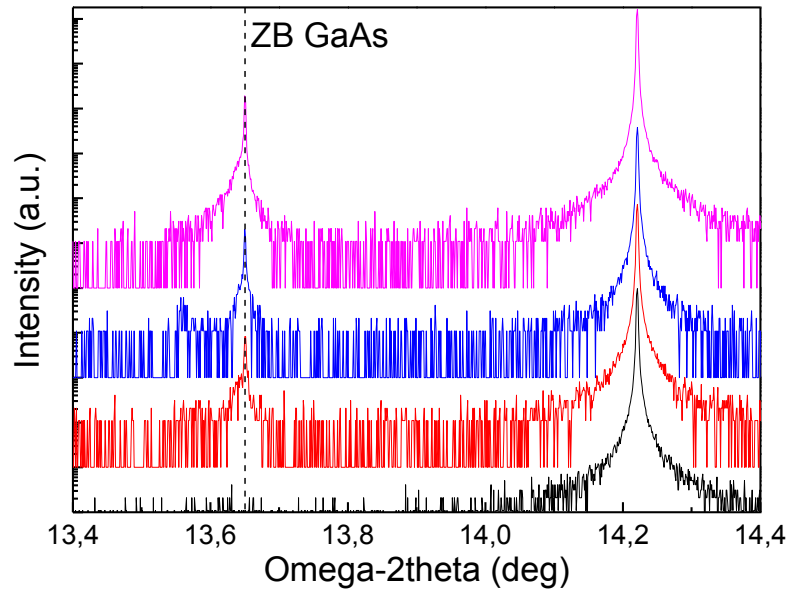


Figure 32. Triple axis XRD measurements of NW samples 1 to 4 from bottom to top respectively. No shift in ZB GaAs peak is detected with respect to the Si(111) peak. ZB GaAs diffraction marked according to [11]

The peaks in RSMs measured using open detector were significantly broadened as seen in Figure 31 b). Hence, RSMs of samples 1-4 were measured also using triple-axis scans (Figure 33). The triple-axis RSMs are calibrated to correspond the literature value of Si(111) reflection [11]. They show that the NW peaks are spread in the Q_x direction. This indicates mosaicity which is probably caused by slight random tilts of the NWs with respect to the substrate crystal. [119] In the RSM of sample 4 [Figure 33 a)] with preserved Ga droplets in the NW tips no WZ peak is observed. However, clear low intensity reflection in the region corresponding to WZ is seen on RSMs of samples 3 and 2 [Figure 33 b) and c)]. This indicates that the largest WZ segments are most likely created during the crystallization of Ga droplets as the local group V partial pressure increases. [122] Another possible explanation for different wurtzite composition is different growth conditions. Sample 4 is grown on a whole 2 inch substrate whereas samples 1 to 3 were grown on a scribed 1/6 2 inch substrate. In terms of the pyrometer reading and the V/III ratio, the growth conditions were identical, although the flux meter reading could not be completely trusted. Larger group V partial pressure, which might cause formation of stacking faults and WZ segments, should increase the NW growth rates. However, judging from the growth rates the growth conditions were almost identical for samples 1-3 and 4. Hence, the growth conditions are only slightly different and very unlikely the source of WZ phases seen in the RSMs of samples 1-3 [Figure käänteishil-kartta2 b)-d)]. [70; 71; 122]

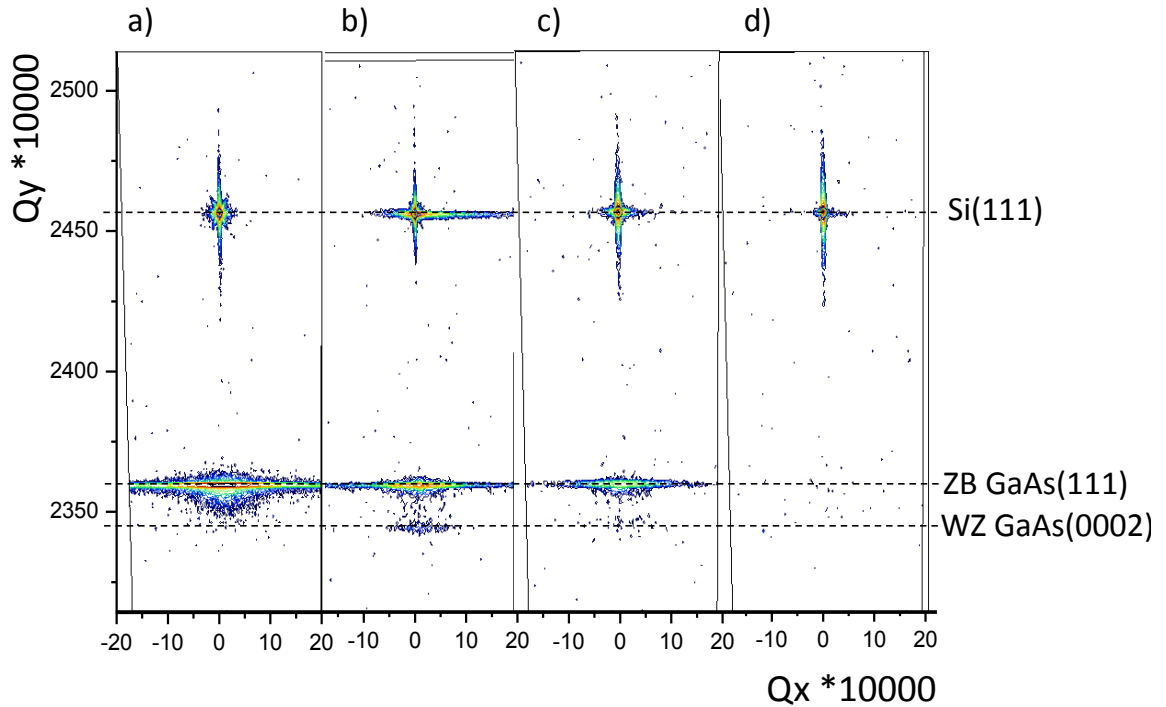


Figure 33. *Si(111), ZB GaAs(111) and WZ GaAs(0002) Bragg peaks are marked as dashed lines in the RSMs of samples 4-1 in a) to d) respectively. The RSM coordinates were adjusted to correspond the theoretical Si(111) Bragg peak.*

Lattice constant values for ZB and WZ GaAs were calculated from the calibrated values using Equations 9, 10 and 12 (Table 4). The ZB GaAs lattice constant differs from literature value [11] only by 0.015 %. The obtained WZ lattice constant value is 6.568875 Å. The closest theoretical literature value is 6.851 Å obtained in [132]. However, the WZ and ZB segments induce strain into consecutive segments which brings the ZB and WZ peaks closer to each other. As most of the WZ phases are presumed to be in the NW tips the ZB peak is seen in its expected location, whereas the WZ peak is probably seen in too large angle. This means that the WZ lattice constant is probably larger than the calculated value. [123]

Table 4. *Results obtained from RSMs presented with corresponding literature values (Si(111), ZB GaAs [11] and WZ GaAs [130], [131]).*

Bragg peak	Si(111)	ZB GaAs(111)	WZ GaAs(0002)
Q_y	0.25657	0.236034	0.234524
d_{hkl} (Å)	3.135589	3.263426	3.284438
a (Å)	5.431	5.652419	6.568875
a (Å), literature	5.431	5.65325	6.4070 - 6.67845

4.2.2 Room temperature photoluminescence

The room temperature (RT) PL was measured from the core-shell NW samples A and B and the reference sample 1 using Accent RPM2000 PL mapper. The PL spectra are presented in Figure 34. The same settings are used for all the spectra except for the scan rate. The PL intensity depends linearly on the scan rate, so it can be corrected with a scaling factor. The scan rate was 140 pts/s for samples A and B and 1 pts/s for sample 1. The room temperature PL spectra shown in Figure 34 demonstrate clearly the necessity of AlGaAs passivation shell in order to suppress the nonradiative surface recombination in the NWs and obtain high PL intensities. This is in good agreement with previous studies, for example the carrier lifetime measurements presented in [8] and [103]. Furthermore, different PL intensities are obtained for samples A and B with different passivation shell thicknesses. This shows that the 10 nm thickness of AlGaAs in sample B is not adequate in order to obtain highest possible PL intensities. This is also found in [133] and [103] where PL intensity increase was studied as a function of the AlGaAs passivation shell thickness. In prior the PL intensity was noticed to saturate when the thickness exceeds 20 nm, whereas the latter reports too thick (over 50 nm) AlGaAs layers to be detrimental for the NW emission properties. Despite of these results as thin as 5 nm [1; 2] and 10 nm [2] AlGaAs passivation shells are widely used in NWs aiming for applications.

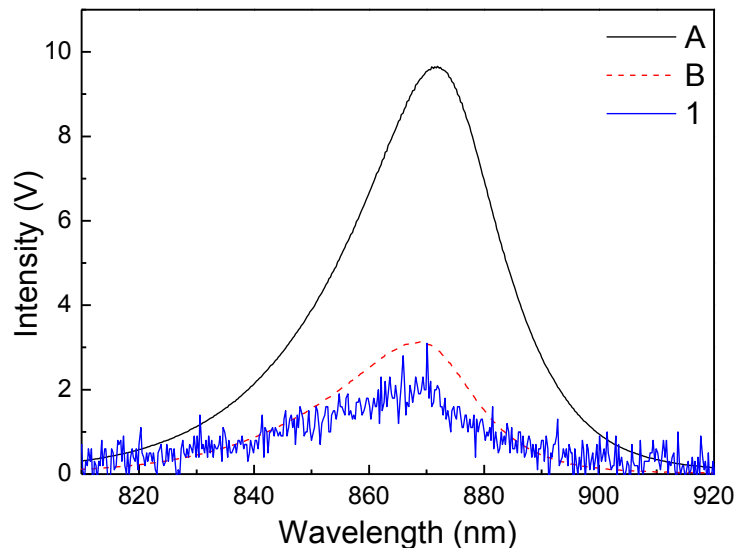


Figure 34. Room temperature PL spectra of samples A, B and 1 are presented from highest to lowest intensity, respectively. The spectrum of sample 1 scaled up with a factor of 14000 in order to obtain visible peak.

The PL spectra of core-shell NWs (samples A-B) were measured right after their growth and 15 months later in order to see the effect of aging on the photoluminescence intensity. The spectra were collected using wafer mapping as the PL intensities varied significantly in different locations on the samples. The PL weakening presented in Table 5 is

assumed to be caused by oxygen diffusion into the AlGaAs passivation shell. Oxygen creates deep level traps in AlGaAs which forms a path for nonradiative recombination for carriers in the NW core if the oxygen diffuses adequately deep in the shell layer [134]. Furthermore, AlGaAs oxidation is detected in preliminary X-ray photoelectron spectroscopy conducted on these samples. The PL weakening is larger for sample A with thicker AlGaAs shell. This is probably due to strain relaxation the AlGaAs shell [103]. Based on the oxidation effect, the 5 nm GaAs cap which is commonly used in order to prevent the oxidation of AlGaAs shell in core-shell NWs [1; 2] is not thick enough in order to protect the NWs from oxidation of the AlGaAs shell for long time periods. In contrast to NW growths regular 2D structures where the topmost layer of the structure is AlGaAs are typically capped with at least 10 nm GaAs. Hence, thicker GaAs capping should be used for GaAs/AlGaAs/GaAs core-shell NWs if they are intended to be used in any application.

Table 5. Results from PL maps measured right after and 10 to 12 months after the growth.

Sample	AlGaAs shell thickness (nm)	GaAs cap thickness (nm)	Intensity weakening (%)
A	25	5	20
B	10	5	13

4.2.3 Micro-photoluminescence of bare GaAs nanowires

Spectral images of samples 2, 3 and 4 are presented in Figure 35 a), b) and c) respectively. The images are taken in 5 K using pulsed 640 nm excitation laser with 300 μ W power on 20 μ m spot. The images are obtained using a 1024x256 pixel 2D CCD detector. As the light from the sample hits the monochromator grating the spectrum is spread over the x-axis of the image. Hence, the wavelength of the light is on the x-axis of the spectral images. The intensity of each wavelength is found on y-axis as a function of location. Hence the stripes seen in the spectral images are either single NWs or densely grown NW clusters. The tracks that are used for accumulating the spectra analyzed in this chapter are marked with dashed lines in Figure 39.

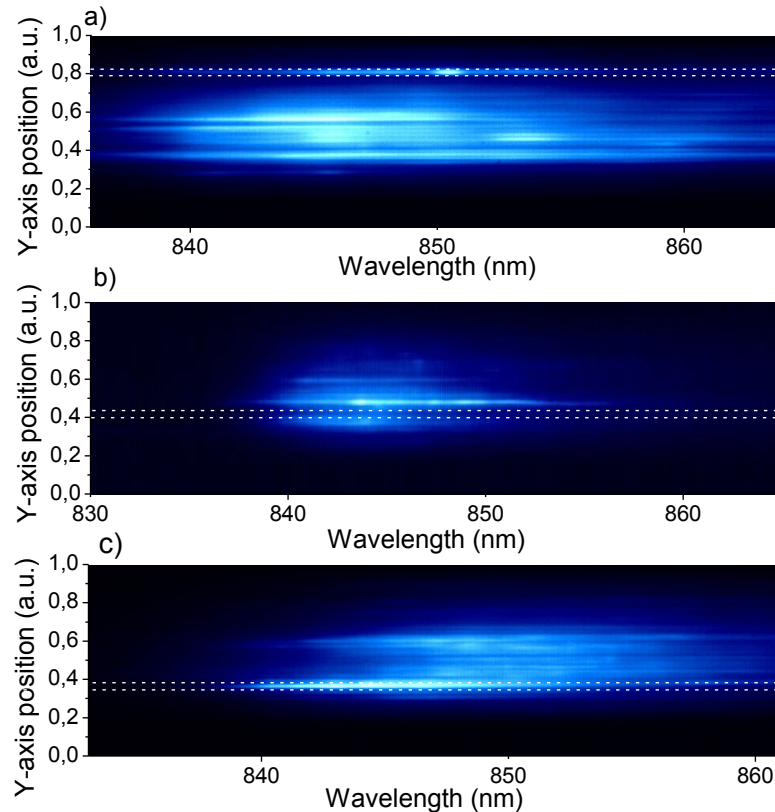


Figure 35. Spectral images of samples 2, 3 and 4 are presented in a) to c) respectively. Individual NWs are seen as different horizontal lines. The lines used in the measurements are marked with dashed lines.

The power dependent behavior of the PL spectra from samples 2-4 is presented in Figure 36. The spectra are obtained from the tracks marked in Figure 35. As the excitation power increases shorter wavelengths are emitted. The PL peak of sample 3 shifts from 850 nm to 830 nm while the excitation power is increased from 0.3 μW to 3000 μW . These powers correspond to power densities 0.01 W/cm^2 and 960 W/cm^2 . This blue shift is typical behavior for saturating localized defect emission, as observed for example for donor-acceptor pair emission. [22] In the lower excitation powers small carrier concentrations are able to diffuse into the localized and discrete defect and interface states and recombine there. The peak shifts to higher energies as the density of the excited carriers increases, the localized states start to saturate and the higher bulk-like energy states are populated. Based on literature, the long wavelength emission at low power densities and emergence of bulk GaAs emission peak at around 816 nm [11] under higher excitation power densities is observed for NWs that probably contain stacking faults. [62; 107] According to [135] the broad peaks around 830-850 nm might be created as the spectra of individual WZ/ZB interfaces are summed. Hence, it could be deduced that there are WZ/ZB stacking faults along the whole length of the NWs in samples 2-4 as suspected based on the XRD measurements presented in chapter 4.2.1 of this thesis. However, the large amount of fine structure in spectra of sample 2 in Figure 36 a) shows that also the droplet crystallization affects the spectra. In sample 2 the amount of WZ/ZB stacking is the most visible because the NW section formed during

the droplet crystallization is longer compared to the NW length than in sample 3. Hence, the fine structure observed in the long wavelength region using low excitation intensities probably originates from the WZ/ZB interfaces in the section of the NW formed during droplet crystallization. This observation is further supported by the separate WZ peak which is observed in the triple-axis RSMs of samples 2 and 3 but not in the RSM of sample 4 as presented in the chapter 4.2.1 of this thesis.

Another possible source of emission 830-850 nm range is unintended Si doping caused by Si solubility in the Ga droplet during the Ga wetting of the template. In the Ga wetting temperature of 640 °C the solubility of Si in Ga is about 1 atomic percent [136]. Silicon doping causes emission in 835 nm in bulk GaAs (4.2 K) [137]. Furthermore, ZB NWs grown on GaAs(111) substrate are observed to emit in ZB GaAs wavelengths [16] whereas NWs grown on Si(111) substrate exhibit a shoulder in their emission spectra in the same range as samples 2–4 even with high excitation powers [86]. Based on these studies it seems probable that the emission dominating in higher excitation powers (837-840 nm in samples 2-4) is caused by unintended Si doping, whereas the low excitation power emission with fine structure in longer wavelengths is caused by stacking faults. However, possibility of carbon impurity [103; 105] cannot be excluded based on these measurements.

Also the possibility of emission obtained from parasitic growth should be considered. From sample 1 PL was obtained only from very small spots scattered sparsely over the sample. This PL was attributed to larger mounds of parasitic growth because it was found scattered significantly more sparsely than NWs. The intensities obtained from these spots were extremely small. Furthermore, the depth resolution of the μ -PL system is very sharp (few hundred nm) meaning that the emission from the longer NWs is obtained from areas above the substrate surface. Hence, it can be concluded that the contribution of parasitic growth in the PL spectra of other samples is negligible.

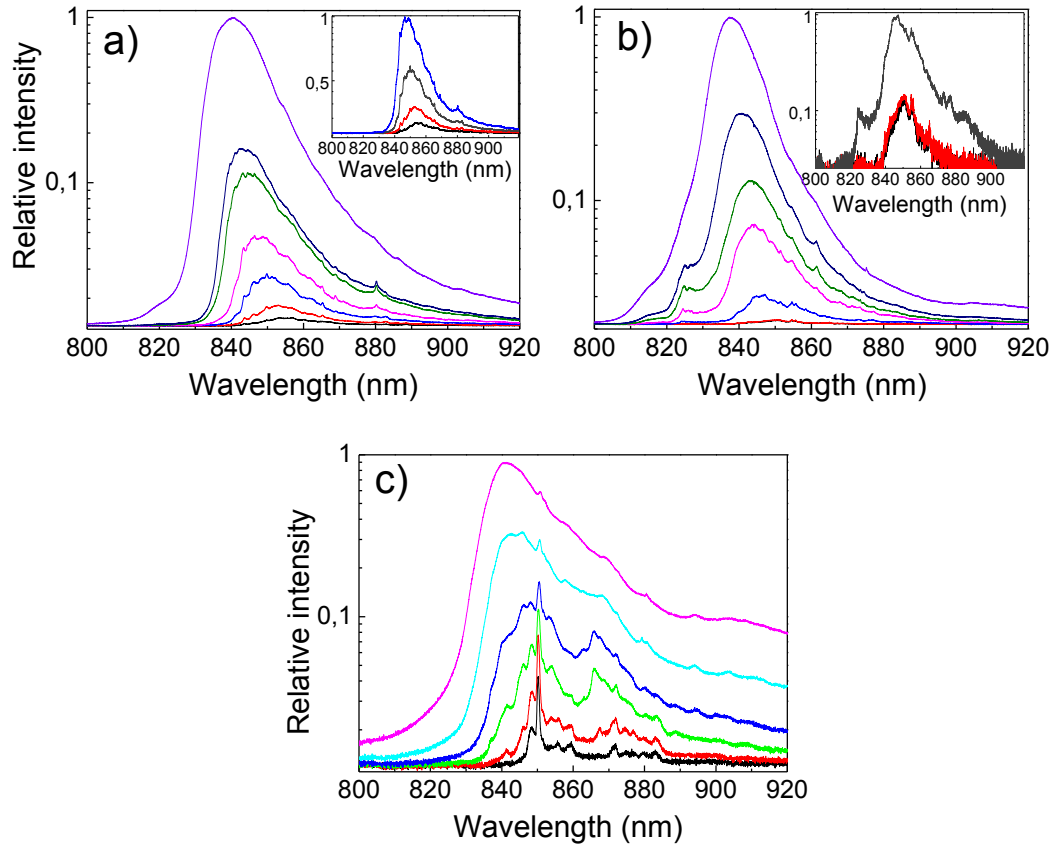


Figure 36. Power dependent spectra of NW samples 2, 3 and 4 are presented in a) to c) respectively. The power densities range from 3 to 960 W/cm^2 in a), 0.1 to 960 W/cm^2 in b) and 0.1 to 96 W/cm^2 in c). The insets in b) and c) show the low power spectra in order to visualize the fine structure in the PL emission.

The temperature dependent behavior of NWs is studied for samples 3 and 4 because detectable PL was obtained in relatively high (130 K) temperatures from these samples. Figure 37 shows typical temperature dependent behavior in samples 3 and 4 from the lines marked in Figure 35. The fine structure of the emission is not detectable as the excitation power was 300 μW (96 W/cm^2) in order to obtain emission in higher temperatures. The most significant effect in the temperature dependent behavior is the change of the emission peak. Initially longer wavelength peak seen in the power dependent measurements dominates the PL but at 40 K a shoulder on the short wavelength side emerges. At 70 K this peak reaches the initial longer wavelength peak in terms of intensity and eventually starts to dominate the emission. The short wavelength peak dominating in high temperatures is the bulk GaAs emission whereas the low temperature emission in longer wavelengths is probably caused by a combination of unintentional Si doping and stacking faults as discussed before. [135] In the higher temperatures the excited carriers have enough thermal energy to escape from the localized states and the emission is caused by free bulk GaAs excitons. This causes the change of emission peak and further confirms that the long wavelength peak dominating in low temperatures is caused by emission from localized states.

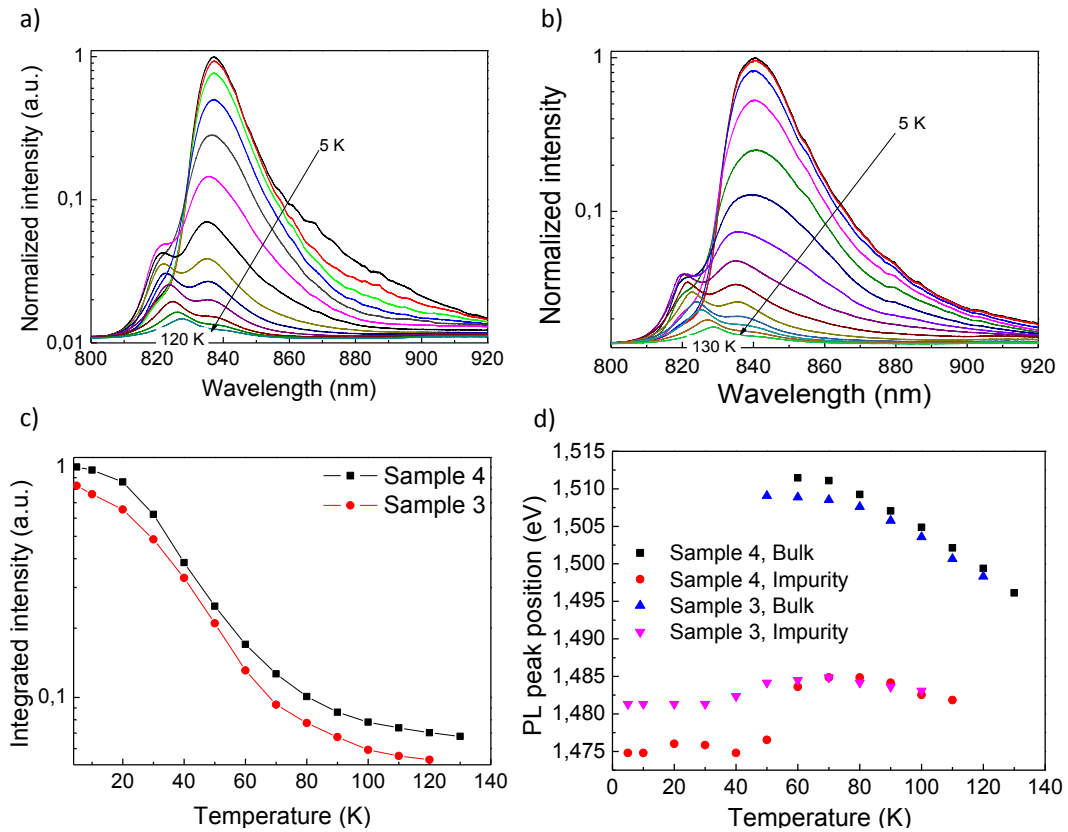


Figure 37. PL spectra of sample 3 and 4, in a) and b) respectively, are presented in temperatures between 5 and 130 K. Integrated PL intensity of samples 3 and 4 is presented in c) as a function of temperature. The PL peak positions of long and short wavelength peaks are presented in d).

The integrated PL intensity is presented in Figure 37 c) as a function of temperature. The integrated PL intensity of bulk GaAs quenches exponentially as a function of temperature already in the lowest temperatures. However, in samples 3 and 4 the integrated PL intensity starts to quench in about 20 K and saturates in low values at 100 K. Similar behavior is typical for disordered systems, for example quantum wells, although the quenching and saturation typically occurs in higher temperatures. [106] The fast PL quenching is explained by the carrier diffusion to the surface states in the NWs. As the carriers have enough thermal energy to escape from the localized states they are able to diffuse to the NW surface where they recombine nonradiatively.

The position of PL peak maxima for samples 3 and 4 are presented as a function of temperature in Figure 37 d). The long wavelength peak position is initially independent of temperature. In 40 K the peak blue shifts towards higher energies. In 70 K the peak energy starts to reduce. This is called S-shaped temperature dependence which is typical for disordered systems. [135] This further supports the presence of stacking faults, unintentional Si doping or C impurities in the NWs. The short wavelength peak follows the temperature dependent Varshni-like behavior of bulk materials presented in chapter 2.1.2 of this thesis [17]. This indicates that the short wavelength peak indeed is the bulk GaAs emission.

4.2.4 Micro-photoluminescence of GaAs/AlGaAs core-shell nanowires

Power and temperature dependent PL behavior of single GaAs/AlGaAs core-shell NW was measured. The NW from core-shell NW sample A was aligned horizontally on SiO₂ substrate with a metallic 10x10 grid as presented in Figure 38. The sample was imaged using SEM in order to locate NWs aligned parallel to the grid. Further, the sample was aligned in the setup so that these NWs were parallel to the monochromator slit and the y-axis of the CCD detector. Power dependent PL measurement was conducted for a single NW and seen in Figure 38. Also several other NWs were excited in order to ensure that they exhibit similar behavior regarding lasing.

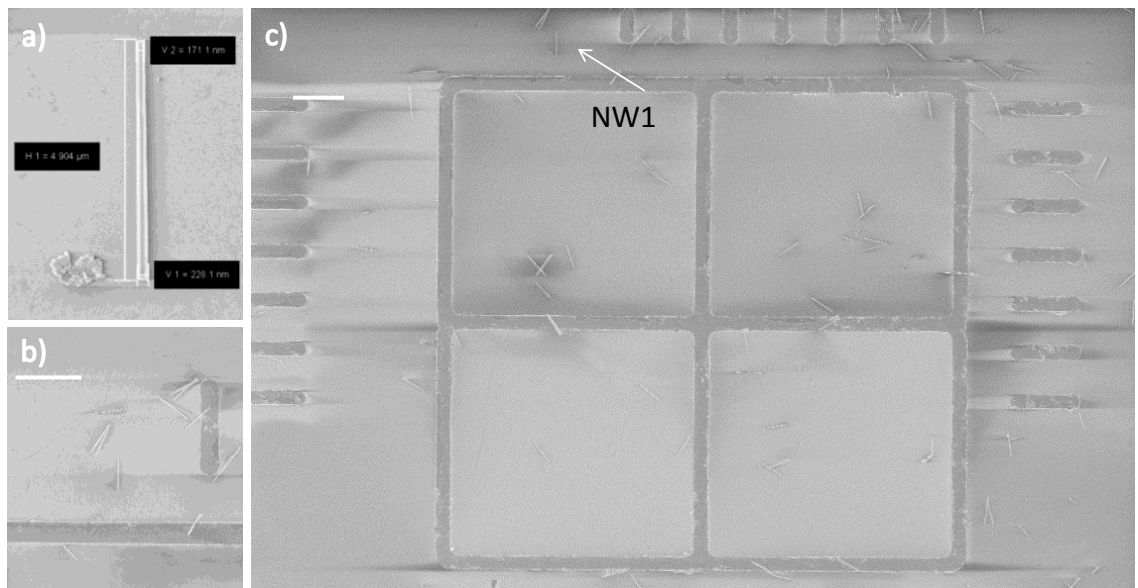


Figure 38. SEM images show the studied NW a) and its alignment on the grid b) and c). The coordinates (7, 7) of the grid are marked as lines in the upper and the right edge of c). The dimensions marked in the NW in a) are 171 nm, 4.9 μm and 228 nm from top to bottom respectively. The narrower end of the NW is originally the bottom of the NW.

The scale bars in b) and c) are 10 μm.

The NW length was 4.9 μm, tip diameter 228 and bottom diameter 171 nm. The temperature dependent μ-PL spectra of this NW are presented in Figure 40. They are accumulated over the whole NW length presented in Figure 39.

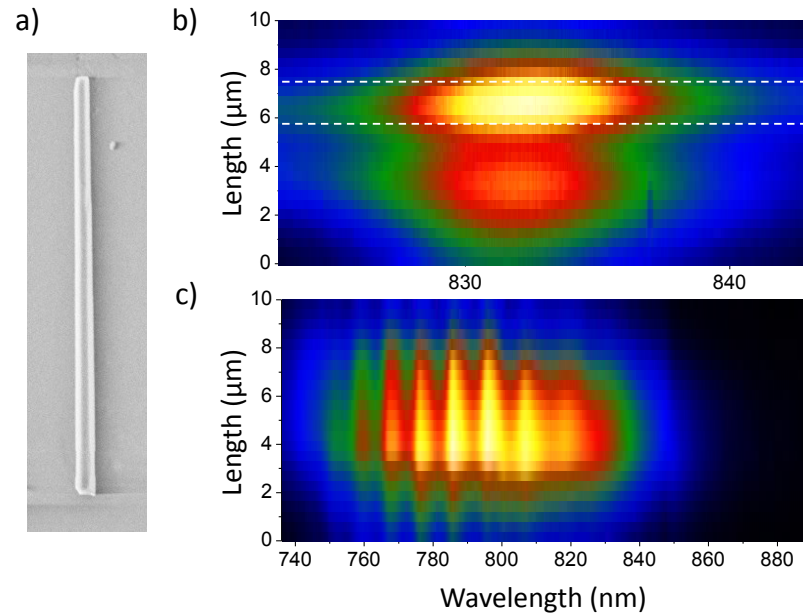


Figure 39. The core-shell NW (length 4.9 μm) used in the $\mu\text{-PL}$ measurements is presented in a). In b) and c) spectral images of the NW with 10 μW and 7000 μW excitation powers, respectively. The Length scale is an estimation based on the spectral images and the NW length.

The thermally induced PL-quenching is faster than for bare GaAs NWs. This is mainly caused by lower excitation intensity (30 μW). Also faster scan rates were used to prevent the detector saturation in lowest temperatures. The scan rate was held constant in order to be able to compare the intensities. The Bulk GaAs peak is visible in 5 K and it starts to dominate already in 50 K. The long wavelength emission peak is found in 5-7 nm smaller wavelengths than from bare GaAs NWs. The NW core is grown similarly to sample 4 although the droplets have been crystallized before the shell growth. Hence similar amount of Si and C impurities and stacking faults is expected in the NW core. Therefore, the differences in the spectra are probably caused by the AlGaAs passivation shell and the sample alignment. Even with lower excitation intensities the carrier concentration in the GaAs core is higher than in the bare NWs because nonradiative surface recombination is suppressed. Also the NW is excited through its whole length which induces more excited carriers than in the vertical alignment. The blue shift of long wavelength emission is probably caused by higher carrier concentrations which induce emission from higher energy states and hence the emission is blue shifted. [22] However, the bulk GaAs emission is red shifted to 824 nm. This is partially caused by tensile strain which is induced to the NW core by the AlGaAs passivation shell. [8] The shift to 824 nm fits well the 22 meV band bending presented in [103]. In addition to strain also surface state traps affect the red shift.

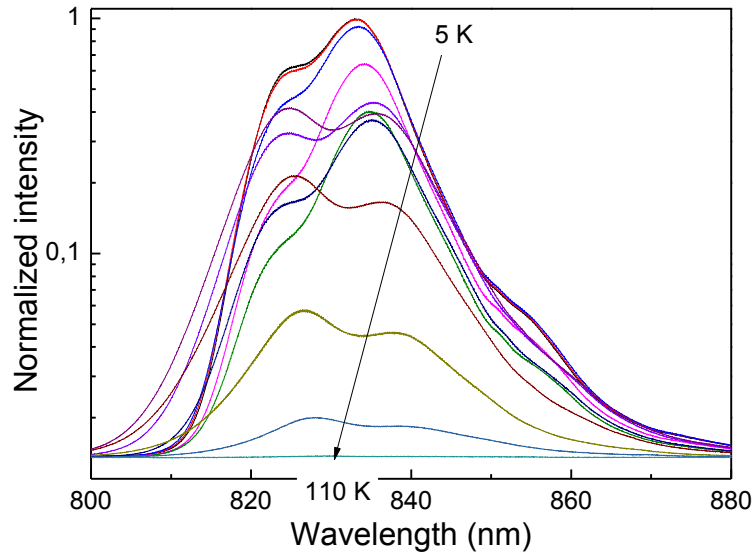


Figure 40. Temperature dependent PL-spectra of NW1 are presented from 5 to 110 K.

The power dependent μ -PL spectra in Figure 41 are measured from the single core-shell NW, from the track marked in Figure 39 b). The track is recognized as the tip of the NW based on the sample orientation. The emission occurs on shorter wavelengths and the bulk GaAs emission starts to dominate with relatively low excitation power, namely 30 μ W. This is caused by increased carrier concentrations in the NW core as discussed above. A small interface peak in 850 nm can be seen from the lowest excitation power spectra. This and other long wavelength emission is probably caused by indirect WZ/ZB transitions. The small amount of emission in this range indicates that there is only a small amount of stacking faults in this NW which are probably formed during droplet crystallization before the shell growth.

The photonic properties of the core-shell NW were investigated by measuring the PL at high power pulsed excitation. The NW PL spectra in Figure 41 b) show periodic modulation in high power regime. This modulation is caused by consecutive longitudinal Fabry-Pérot modes in the NW. In case of lasing, one of these modes would emit with several orders of magnitude higher intensity as other modes would suppress. No lasing is observed which is probably caused by low confinement factor. The confinement factor describes the fraction of the beam in the active layer. The part of the beam outside this region does not participate in stimulated emission. According to [1] the confinement factor for a NW with 200 nm diameter is approximately 0.35. The confinement factor increases with the NW diameter and lasing was observed in NWs with 340 nm diameter and confinement factor of 0.9 [1].

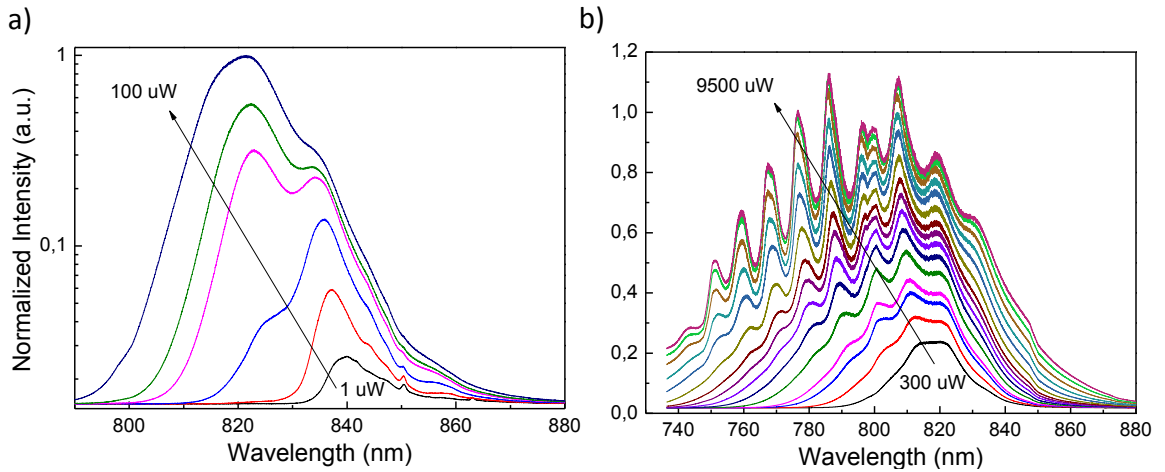


Figure 41. Power dependent μ -PL spectra of the core-shell NW are presented in a) and b) in low and high power regions. Notice the linear intensity scale in b). Dashed lines in b) mark three supported longitudinal modes calculated using free spectral range obtained from the same data.

The effective refractive group index n_{group} of the NWs is calculated using the free spectral range $\Delta\nu_{FSR}$ of the Fabry-Pérot (FP) modes seen in the power dependent measurements. The $\Delta\nu_{FSR}$ for a laser cavity can be calculated using equation

$$\Delta\nu_{FSR} = \frac{c}{2Ln_{group}}, \quad (14)$$

where c is the speed of light in vacuum and L is the length of the resonant cavity. [1] When the effective refractive group index is known the possible wavelengths of the principal longitudinal laser cavity modes can be calculated by

$$\lambda_k = \frac{2L_{OP}}{k}, \quad (15)$$

where L_{OP} is the optical length of the cavity and k is a positive integer describing how many half wavelengths of λ_k are present in the cavity.

The free spectral range $\Delta\nu_{FSR}$ of the cavity formed by the core-shell NW was 6.82 THz corresponding to 14.8 nm mode separation determined from the spectra in Figure 41. Using this value and Equation 14 the group refractive index n_{group} of the NW was calculated to be 4.48 for the mode present in the NW. In [1] the n_{group} of TE₀₁ mode was 4.85 for NWs with 360 nm diameter and n_{group} values were smaller for narrower NWs. Hence the value seems reasonable. Using Equation 15 and value $n_{group} = 4.48$ possible longitudinal modes were calculated. The mode wavelengths are presented in Table 6.

Table 6. Calculated λ_{cal} and the nearest measured λ_{meas} wavelengths for different Fabry-Pérot modes in the core-shell NW are presented as a function of the mode index k .

k	82	83	84	85	86	87	88	89
λ_{cal} (nm)	830.1	820.1	810.3	800.8	791.5	782.4	773.5	764.8
λ_{meas} (nm)	830	819	807	798	786	776	767	759

In shorter wavelengths a 6 nm offset accumulates between the observed and calculated FP mode locations. This difference is probably caused by non-ideality of the cavity. Especially the NW tapering affects the modes. [138] Also the effect of imperfect NW end facets should be considered.

5. CONCLUSIONS

The droplet epitaxy procedure was found to be rather challenging. Fortunately, suitable templates for NW growth on lithography-free oxides patterns were grown using droplet epitaxy. The successful samples grown in the 10-2 reactor did not reveal any certain pre-growth chemical treatment or substrate type that would have been better than others. Hence, the 10 s dip in 5 % aqueous HF was favored due to its simplicity. Also the p-type Si(111) substrates without thermally grown oxide shall be used in the future unless n-type doping is required.

The Si(111) surface of the used substrates was noticed to initially roughen in the 10-2 reactor and smoothen as the pre-growth annealing temperature was increased from 545 to 655 °C. The cause of the surface roughness is very likely unintentional Sb exposure from the Sb cracker and possibly the other parts of the 10-2 reactor. Probably due to the Sb exposure, predictable droplet epitaxy growths were obtained only in the V90 reactor which was not equipped with Sb source. The effect and primary source of Sb could be tested by growing a series of droplet epitaxy samples in the 10-2 reactor with closed manual shutter in front of the Sb cracker needle valve. Another matter that requires further investigations is the bimodal size distribution of the GaAs nanocrystals found in some of the droplet epitaxy samples. The formation of smaller GaAs nanocrystals could be prevented by crystallizing the Ga droplets in lower temperatures. Simultaneously, the possibility to obtain circular nanocrystals with small diameters could be tested by using smaller Ga coverages in these growths. Also the usage of a MBE reactor with no Sb source for the future droplet epitaxy growths on Si substrates is strongly advised.

The NWs grown via self-catalyzed method on lithography-free oxide patterns resulted in NWs with good although not complete ZB phase purity based on HR-XRD and μ -PL characterization. Larger WZ segments were observed by XRD only in the GaAs NWs with crystallized Ga droplets. However, indications of stacking faults and other minor WZ segments were seen as broadening of the ZB peak also in the NWs with preserved catalyst droplets. Furthermore, fine structure arising from localized emission was seen in the μ -PL measurements of the NWs whether or not the droplets were crystallized. However, the fine structure emission was the most prominent in the NWs where largest proportion of the NW volume was formed by the droplet crystallization.

The low temperature μ -PL spectra of the bare GaAs NWs were dominated by impurity related broad emission peak in 830-850 nm range. Possible sources of this emission are indirect recombination at WZ/ZB interfaces and localized recombination in stacking faults along with emission from carbon and silicon impurity sites. The presence of Si

impurity originating from the substrate will be confirmed as this could be a pathway into purely n-type Si doping in NWs which has been so far prevented by the amphoteric nature of Si causing p-type doping when it is incorporated to the NWs through the sidewalls [139]. On the other hand, in the unlikely situation where this emission was purely caused by stacking faults and polytypism, the presumably good phase purity of our NWs would be questionable. The NW structure will be further investigated by transmission electron microscopy (TEM). A reference for future XRD characterization of the NWs is obtained when the TEM results are combined with the ones presented above.

The room temperature PL measurements of core-shell and bare GaAs NWs demonstrated well the necessity of the NW sidewall passivation in order to prevent nonradiative surface recombination. The 25 nm thickness of the AlGaAs passivation shell was found adequate. However, degradation of the PL intensity over a period of 15 months indicated that the 5 nm GaAs cap was too thin to completely prevent the oxidation of the AlGaAs passivation shell. This should be noted, when core-shell NWs are grown in the future by growing at least 10 nm thick GaAs cap around the NWs. Another possible cause for the PL weakening is the strain between the AlGaAs shell and the Si substrate [103]. The effect of the AlGaAs shell thickness on the sample aging should be studied along with the effect of GaAs cap thickness in order to obtain core-shell NWs that endure aging induced both by oxidation and strain.

The μ -PL measurement of a single GaAs/AlGaAs/GaAs core-shell NW demonstrated clearly formation of longitudinal Fabry-Pérot modes under high excitation powers. However, the modes were observed only at wavelengths shorter than GaAs band edge emission and seen only by band filling under high excitation intensities. This was interpreted to be caused by the small (200 nm) diameter of the NW which was not adequate to confine modes in the GaAs band edge emission wavelengths. Based on this, thicker core-shell NWs should be grown in order to obtain lasing. Also growing tapered NWs for lasing would be extremely interesting as single mode lasing could be obtained [138]. However, the novelty of obtaining lasing from GaAs/AlGaAs/GaAs is rather low. Hence, NWs with radial quantum wells would be more interesting subject to study. Also other material systems might be an interesting topic as the characterization methods suitable for basic NW material research presented in this work could be further exploited.

All in all a lot of possibilities to obtain novel results based on our NWs is possible as presented above. Although, more work is required in order to fully understand the droplet epitaxy process in order to provide steady supply of templates for the NW growth. Also a lot was learnt about the versatile NW characterization method possibilities and their feasibility here at ORC.

REFERENCES

- [1] Mayer, B., Rudolph, D., Schnell, J., Morkötter, S., Winnerl, J., Treu, J., Müller, K., Bracher, G., Abstreiter, G., Koblmüller, G. & Finley, J.J. Lasing from individual GaAs-AlGaAs core-shell nanowires up to room temperature. *Nat Commun* 4 (2013).
- [2] Mayer, B., Janker, L., Loitsch, B., Treu, J., Kostenbader, T., Lichtmannecker, S., Reichert, T., Morkötter, S., Kaniber, M., Abstreiter, G., Gies, C., Koblmüller, G. & Finley, J.J. Monolithically Integrated High- β Nanowire Lasers on Silicon. *Nano Letters* 16 (2016) 1, pp. 152-156.
- [3] LaPierre, R.R. Theoretical conversion efficiency of a two-junction III-V nanowire on Si solar cell. *Journal of Applied Physics* 110 (2011) 1, pp. 014310.
- [4] Couteau C., Larrue A., Wilhelm C. & Soci C. Nanowire Lasers. *Nanophotonics* 4 (2015).
- [5] Wallentin, J., Anttu, N., Asoli, D., Huffman, M., Åberg, I., Magnusson, M.H., Siefert, G., Fuss-Kailuweit, P., Dimroth, F., Witzigmann, B., Xu, H.Q., Samuelson, L., Depert, K. & Borgström, M.T. InP Nanowire Array Solar Cells Achieving 13.8% Efficiency by Exceeding the Ray Optics Limit. *Science* 339 (2013) 6123, pp. 1057-1060.
- [6] Tomioka, K., Motohisa, J., Hara, S., Hiruma, K. & Fukui, T. GaAs/AlGaAs Core Multishell Nanowire-Based Light-Emitting Diodes on Si. *Nano Letters* 10 (2010) 5, pp. 1639-1644.
- [7] Dimakis, E., Jahn, U., Ramsteiner, M., Tahraoui, A., Grandal, J., Kong, X., Marquardt, O., Trampert, A., Riechert, H. & Geelhaar, L. Coaxial Multishell (In,Ga)As/GaAs Nanowires for Near-Infrared Emission on Si Substrates. *Nano Letters* 14 (2014) 5, pp. 2604-2609.
- [8] Hakkarainen, T.V., Schramm, A., Mäkelä, J., Laukkanen, P. & Guina, M. Lithography-free oxide patterns as templates for self-catalyzed growth of highly uniform GaAs nanowires on Si(111). *Nanotechnology* 26 (2015) 27, pp. 275301.
- [9] Meyers, H.P. & Myers, H.P. *Introductory Solid State Physics*, Second Edition. 1997, Taylor & Francis.
- [10] Vegard, L. Die Konstitution der Mischkristalle und die Raumfüllung der Atome. *Zeitschrift für Physik* 5 (1921) 1, pp. 17-26.
- [11] Ioffe Institute Ioffe Semiconductors. Ioffe Physico-Technical Institute. [cited 11.8.2015]. Available: <http://www.ioffe.ru/SVA/NSM/Semicond/index.html>.
- [12] Kriegner, D., Panse, C., Mandl, B., Dick, K.A., Keplinger, M., Persson, J.M., Caroff, P., Ercolani, D., Sorba, L., Bechstedt, F., Stangl, J. & Bauer, G. Unit Cell Structure of Crystal Polytypes in InAs and InSb Nanowires. *Nano Letters* 11 (2011) 4, pp. 1483-1489.

- [13] Greeves, N. ChemTube3D, Inorganic Chemistry. University of Liverpool. 2008, [cited 20.10.2015]. Available: <http://www.chemtube3d.com/solidstate/table.htm>.
- [14] Jones, R. Do we really understand dislocations in semiconductors? *Materials Science and Engineering: B* 71 (2000) 1–3, pp. 24-29.
- [15] Herman, M.A. & Sitter, H. *Molecular Beam Epitaxy: Fundamentals and Current Status*. 1996, Springer Berlin Heidelberg.
- [16] Spirkoska, D., Arbiol, J., Gustafsson, A., Conesa-Boj, S., Glas, F., Zardo, I., Heigoldt, M., Gass, M.H., Bleloch, A.L., Estrade, S., Kaniber, M., Rossler, J., Peiro, F., Morante, J.R., Abstreiter, G., Samuelson, L. & Fontcuberta, i.M. Structural and optical properties of high quality zinc-blende/wurtzite GaAs nanowire heterostructures. *Physical Review B* 80 (2009) 24, pp. 245325.
- [17] Vurgaftman, I., Meyer, J.R. & Ram-Mohan, L.R. Band parameters for III–V compound semiconductors and their alloys. *Journal of Applied Physics* 89 (2001) 11, pp. 5815-5875.
- [18] Cotal, H., Fetzer, C., Boisvert, J., Kinsey, G., King, R., Hebert, P., Yoon, H. & Karam, N. III-V multijunction solar cells for concentrating photovoltaics. *Energy & Environmental Science* 2 (2009) 2, pp. 174-192.
- [19] Schubert, E.F. *Light-Emitting Diodes*. 2006, Cambridge University Press.
- [20] Honsberg, C. & Bowden, S. PV education. [cited 25.1.2016]. Available: <http://www.pveducation.org/>.
- [21] Zhang, Y., Fluegel, B., Hanna, M.C., Mascarenhas, A., Wang, L., Wang, Y.J. & Wei, X. Impurity perturbation to the host band structure and recoil of the impurity state. *Physical Review B* 68 (2003) 7, pp. 075210.
- [22] Gfroerer, T.H. Photoluminescence in Analysis of Surfaces and Interfaces. In: Anonymous (ed.). *Encyclopedia of Analytical Chemistry*. 2006; 2000, John Wiley & Sons, Ltd.
- [23] Colli, A., Martelli, F. & Rubini, S. Chapter 3 - Growth of semiconductor nanowires by molecular beam epitaxy. In: Henini, M. (ed.). *Molecular Beam Epitaxy*. Oxford 2013, Elsevier. pp. 55-93.
- [24] Glas, F. Critical dimensions for the plastic relaxation of strained axial heterostructures in free-standing nanowires. *Physical Review B* 74 (2006) 12, pp. 121302.
- [25] Uccelli, E., Arbiol, J., Magen, C., Krogstrup, P., Russo-Averchi, E., Heiss, M., Mugny, G., Morier-Genoud, F., Nygård, J., Morante, J.R. & Fontcuberta, i.M. Three-Dimensional Multiple-Order Twinning of Self-Catalyzed GaAs Nanowires on Si Substrates. *Nano Letters* 11 (2011) 9, pp. 3827-3832.

- [26] Hobbs, R.G., Petkov, N. & Holmes, J.D. Semiconductor Nanowire Fabrication by Bottom-Up and Top-Down Paradigms. *Chemistry of Materials* 24 (2012) 11, pp. 1975-1991.
- [27] Dasgupta, N.P., Sun, J., Liu, C., Britzman, S., Andrews, S.C., Lim, J., Gao, H., Yan, R. & Yang, P. 25th Anniversary Article: Semiconductor Nanowires – Synthesis, Characterization, and Applications. *Advanced Materials* 26 (2014) 14, pp. 2137-2184.
- [28] Peng, K., Wu, Y., Fang, H., Zhong, X., Xu, Y. & Zhu, J. Uniform, Axial-Orientation Alignment of One-Dimensional Single-Crystal Silicon Nanostructure Arrays. *Angewandte Chemie International Edition* 44 (2005) 18, pp. 2737-2742.
- [29] Franchi, S. Chapter 1 - Molecular beam epitaxy: fundamentals, historical background and future prospects. In: Henini, M. (ed.). *Molecular Beam Epitaxy*. Oxford 2013, Elsevier. pp. 1-46.
- [30] Sanguinetti, S. & Koguchi, N. Chapter 4 - Droplet epitaxy of nanostructures. In: Henini, M. (ed.). *Molecular Beam Epitaxy*. Oxford 2013, Elsevier. pp. 95-111.
- [31] Morral, A.F. Gold-Free GaAs Nanowire Synthesis and Optical Properties. *Selected Topics in Quantum Electronics, IEEE Journal of* 17 (2011) 4, pp. 819-828.
- [32] Dubrovskii, V.G., Sibirev, N.V., Cirlin, G.E., Bouravleuv, A.D., Samsonenko, Y.B., Dheeraj, D.L., Zhou, H.L., Sartel, C., Harmand, J.C., Patriarche, G. & Glas, F. Role of nonlinear effects in nanowire growth and crystal phase. *Physical Review B* 80 (2009) 20, pp. 205305.
- [33] Garcia, I., Galiana, B., Rey-Stolle, I. & Algora, C. MOVPE Technology for the Growth of III-V Semiconductor Structures. *Electron Devices, 2007 Spanish Conference on*, 2007, pp. 17-20.
- [34] O'Steen, M., Readinger, E., Doran, M. & Hanser, D. Chapter 29 - Systems and technology for production-scale molecular beam epitaxy. In: Henini, M. (ed.). *Molecular Beam Epitaxy*. Oxford 2013, Elsevier. pp. 657-680.
- [35] Breuer, S., Pfüller, C., Flissikowski, T., Brandt, O., Grahn, H.T., Geelhaar, L. & Riechert, H. Suitability of Au- and Self-Assisted GaAs Nanowires for Optoelectronic Applications. *Nano Letters* 11 (2011) 3, pp. 1276-1279.
- [36] Chang, C., Chi, C., Yao, M., Huang, N., Chen, C., Theiss, J., Bushmaker, A.W., LaLumondiere, S., Yeh, T., Povinelli, M.L., Zhou, C., Dapkus, P.D. & Cronin, S.B. Electrical and Optical Characterization of Surface Passivation in GaAs Nanowires. *Nano Letters* 12 (2012) 9, pp. 4484-4489.
- [37] Lu, Z., Shi, S., Lu, J. & Chen, P. Photoluminescence of the single wurtzite GaAs nanowire with different powers and temperatures. *Journal of Luminescence* 152 (2014) pp. 258-261.

- [38] Heitsch, A.T., Fanfair, D.D., Tuan, H. & Korgel, B.A. Solution-Liquid-Solid (SLS) Growth of Silicon Nanowires. *Journal of the American Chemical Society* 130 (2008) 16, pp. 5436-5437.
- [39] Wang, F., Wayman, V.L., Loomis, R.A. & Buhro, W.E. Solution-Liquid-Solid Growth of Semiconductor Quantum-Wire Films. *ACS Nano* 5 (2011) 6, pp. 5188-5194.
- [40] Yuan, F. & Tuan, H. Supercritical Fluid-Solid Growth of Single-Crystalline Silicon Nanowires: An Example of Metal-Free Growth in an Organic Solvent. *Crystal Growth & Design* 10 (2010) 11, pp. 4741-4745.
- [41] Laocharoensuk, R., Palaniappan, K., Smith, N.A., Dickerson, R.M., Werder, D.J., Baldwin, J.K. & Hollingsworth, J.A. Flow-based solution-liquid-solid nanowire synthesis. *Nat Nano* 8 (2013) 9, pp. 660-666.
- [42] Fanfair, D.D. & Korgel, B.A. Bismuth Nanocrystal-Seeded III-V Semiconductor Nanowire Synthesis. *Crystal Growth & Design* 5 (2005) 5, pp. 1971-1976.
- [43] Li, A., Ercolani, D., Lugani, L., Nasi, L., Rossi, F., Salviati, G., Beltram, F. & Sorba, L. Synthesis of AlAs and AlAs-GaAs Core-Shell Nanowires. *Crystal Growth & Design* 11 (2011) 9, pp. 4053-4058.
- [44] Mohseni, P.K., Rodrigues, A.D., Galzerani, J.C., Pusep, Y.A. & LaPierre, R.R. Structural and optical analysis of GaAsP/GaP core-shell nanowires. *Journal of Applied Physics* 106 (2009) 12, pp. 124306.
- [45] Ohlsson, B.J., Björk, M.T., Magnusson, M.H., Deppert, K., Samuelson, L. & Wallenberg, L.R. Size-, shape-, and position-controlled GaAs nano-whiskers. *Applied Physics Letters* 79 (2001) 20, pp. 3335-3337.
- [46] Hou, X. & Choy, K.-. Processing and Applications of Aerosol-Assisted Chemical Vapor Deposition. *Chemical Vapor Deposition* 12 (2006) 10, pp. 583-596.
- [47] Stoycheva, T., Annanouch, F.E., Gràcia, I., Llobet, E., Blackman, C., Correig, X. & Vallejos, S. Micromachined gas sensors based on tungsten oxide nanoneedles directly integrated via aerosol assisted CVD. *Sensors and Actuators B: Chemical* 198 (2014) pp. 210-218.
- [48] Avit, G., Lekhal, K., André, Y., Bougerol, C., Réveret, F., Leymarie, J., Gil, E., Monier, G., Castelluci, D. & Trassoudaine, A. Ultralong and Defect-Free GaN Nanowires Grown by the HVPE Process. *Nano Letters* 14 (2014) 2, pp. 559-562.
- [49] Gil, E., Dubrovskii, V.G., Avit, G., André, Y., Leroux, C., Lekhal, K., Grecenkov, J., Trassoudaine, A., Castelluci, D., Monier, G., Ramdani, R.M., Robert-Goumet, C., Bideux, L., Harmand, J.C. & Glas, F. Record Pure Zincblende Phase in GaAs Nanowires down to 5 nm in Radius. *Nano Letters* 14 (2014) 7, pp. 3938-3944.
- [50] Ramdani, M.R., Gil, E., Leroux, C., André, Y., Trassoudaine, A., Castelluci, D., Bideux, L., Monier, G., Robert-Goumet, C. & Kupka, R. Fast Growth Synthesis of GaAs Nanowires with Exceptional Length. *Nano Letters* 10 (2010) 5, pp. 1836-1841.

- [51] Heurlin, M., Magnusson, M.H., Lindgren, D., Ek, M., Wallenberg, L.R., Deppert, K. & Samuelson, L. Continuous gas-phase synthesis of nanowires with tunable properties. *Nature* 492 (2012) 7427, pp. 90-94.
- [52] Wagner, R.S. & Ellis, W.C. Vapor-Liquid-Solid Mechanism of Single Crystal Growth. *Applied Physics Letters* 4 (1964) 5, pp. 89-90.
- [53] Dubrovskii, V.G., Cirlin, G.E., Soshnikov, I.P., Tonkikh, A.A., Sibirev, N.V., Samsonenko, Y.B. & Ustinov, V.M. Diffusion-induced growth of GaAs nanowhiskers during molecular beam epitaxy: Theory and experiment. *Physical Review B* 71 (2005) 20, pp. 205325.
- [54] Messing, M., Hillerich, K., Johansson, J., Deppert, K. & Dick, K. The use of gold for fabrication of nanowire structures. *Gold Bulletin* 42 (2009) 3, pp. 172-181.
- [55] Chen, L., Lu, W. & Lieber, C.M. Chapter 1 Semiconductor Nanowire Growth and Integration. In: Anonymous (ed.). 2015, The Royal Society of Chemistry. pp. 1-53.
- [56] Borgström, M., Wallentin, J., Trägårdh, J., Ramvall, P., Ek, M., Wallenberg, L.R., Samuelson, L. & Deppert, K. In situ etching for total control over axial and radial nanowire growth. *Nano Research* 3 (2010) 4, pp. 264-270.
- [57] Somaschini, C., Bietti, S., Trampert, A., Jahn, U., Hauswald, C., Riechert, H., Sanguinetti, S. & Geelhaar, L. Control over the Number Density and Diameter of GaAs Nanowires on Si(111) Mediated by Droplet Epitaxy. *Nano Letters* 13 (2013) 8, pp. 3607-3613.
- [58] Breuer, S., Hilse, M., Trampert, A., Geelhaar, L. & Riechert, H. Vapor-liquid-solid nucleation of GaAs on Si(111): Growth evolution from traces to nanowires. *Physical Review B* 82 (2010) 7, pp. 075406.
- [59] Cirlin, G.E., Dubrovskii, V.G., Samsonenko, Y.B., Bouravleuv, A.D., Durose, K., Proskuryakov, Y.Y., Mendes, B., Bowen, L., Kaliteevski, M.A., Abram, R.A. & Zeze, D. Self-catalyzed, pure zincblende GaAs nanowires grown on Si(111) by molecular beam epitaxy. *Physical Review B* 82 (2010) 3, pp. 035302.
- [60] Bar-Sadan, M., Barthel, J., Shtrikman, H. & Houben, L. Direct Imaging of Single Au Atoms Within GaAs Nanowires. *Nano Letters* 12 (2012) 5, pp. 2352-2356.
- [61] Tambe, M.J., Ren, S. & Gradečak, S. Effects of Gold Diffusion on n-Type Doping of GaAs Nanowires. *Nano Letters* 10 (2010) 11, pp. 4584-4589.
- [62] Titova, L.V., Hoang, T.B., Jackson, H.E., Smith, L.M., Yarrison-Rice, J.M., Kim, Y., Joyce, H.J., Tan, H.H. & Jagadish, C. Temperature dependence of photoluminescence from single core-shell GaAs–AlGaAs nanowires. *Applied Physics Letters* 89 (2006) 17, pp. 173126.
- [63] Collins, C.B., Carlson, R.O. & Gallagher, C.J. Properties of Gold-Doped Silicon. *Physical Review* 105 (1957) 4, pp. 1168-1173.

- [64] Hill, M., Lietz, M. & Sittig, R. Diffusion of Gold in Silicon. *Journal of the Electrochemical Society* 129 (1982) 7, pp. 1579-1587.
- [65] Fontcuberta i Morral, A., Colombo, C., Abstreiter, G., Arbiol, J. & Morante, J.R. Nucleation mechanism of gallium-assisted molecular beam epitaxy growth of gallium arsenide nanowires. *Applied Physics Letters* 92 (2008) 6, pp. 063112.
- [66] Matteini Federico, Dubrovskii, V.G., Ruffer, D., Tütüncüoğlu, G., Fontana, Y. & Fontcuberta, I.M.A. Tailoring the diameter and density of self-catalyzed GaAs nanowires on silicon. *Nanotechnology* 26 (2015) 10, pp. 105603.
- [67] Krogstrup, P., Popovitz-Biro, R., Johnson, E., Madsen, M.H., Nygård, J. & Shtrikman, H. Structural Phase Control in Self-Catalyzed Growth of GaAs Nanowires on Silicon (111). *Nano Letters* 10 (2010) 11, pp. 4475-4482.
- [68] Ramdani, M.R., Harmand, J.C., Glas, F., Patriarche, G. & Travers, L. Arsenic Pathways in Self-Catalyzed Growth of GaAs Nanowires. *Crystal Growth & Design* 13 (2013) 1, pp. 91-96.
- [69] Bastiman, F., Küpers, H., Somaschini, C. & Geelhaar, L. Growth map for Ga-assisted growth of GaAs nanowires on Si(111) substrates by molecular beam epitaxy. *Nanotechnology* 27 (2016) 9, pp. 095601.
- [70] Colombo, C., Spirkoska, D., Frimmer, M., Abstreiter, G. & Fontcuberta, i.M. Ga-assisted catalyst-free growth mechanism of GaAs nanowires by molecular beam epitaxy. *Physical Review B* 77 (2008) 15, pp. 155326.
- [71] Glas, F., Ramdani, M.R., Patriarche, G. & Harmand, J. Predictive modeling of self-catalyzed III-V nanowire growth. *Physical Review B* 88 (2013) 19, pp. 195304.
- [72] Bietti, S., Somaschini, C., Frigeri, C., Fedorov, A., Esposito, L., Geelhaar, L. & Sanguinetti, S. Self-assisted GaAs nanowires with selectable number density on Silicon without oxide layer. *Journal of Physics D: Applied Physics* 47 (2014) 39, pp. 394002.
- [73] Samsonenko, Y.B., Cirilin, G.E., Khrebtov, A.I., Bouravleuv, A.D., Polyakov, N.K., Ulin, V.P., Dubrovskii, V.G. & Werner, P. Study of processes of self-catalyzed growth of gaas crystal nanowires by molecular-beam epitaxy on modified Si (111) surfaces. *Semiconductors* 45 (2011) 4, pp. 431-435.
- [74] Hertenberger, S., Rudolph, D., Bolte, S., Döblinger, M., Bichler, M., Spirkoska, D., Finley, J.J., Abstreiter, G. & Koblmüller, G. Absence of vapor-liquid-solid growth during molecular beam epitaxy of self-induced InAs nanowires on Si. *Applied Physics Letters* 98 (2011) 12, pp. 123114.
- [75] Dimakis, E., Lähnemann, J., Jahn, U., Breuer, S., Hilse, M., Geelhaar, L. & Riechert, H. Self-Assisted Nucleation and Vapor-Solid Growth of InAs Nanowires on Bare Si(111). *Crystal Growth & Design* 11 (2011) 9, pp. 4001-4008.
- [76] Rudolph, D., Hertenberger, S., Bolte, S., Paosangthong, W., Spirkoska, D., Döblinger, M., Bichler, M., Finley, J.J., Abstreiter, G. & Koblmüller, G. Direct Observa-

tion of a Noncatalytic Growth Regime for GaAs Nanowires. *Nano Letters* 11 (2011) 9, pp. 3848-3854.

[77] Tuan, H., Lee, D.C., Hanrath, T. & Korgel, B.A. Germanium Nanowire Synthesis: An Example of Solid-Phase Seeded Growth with Nickel Nanocrystals. *Chemistry of Materials* 17 (2005) 23, pp. 5705-5711.

[78] Lu, X., Anderson, K.J., Boudjouk, P. & Korgel, B.A. Low Temperature Colloidal Synthesis of Silicon Nanorods from Isotetrasilane, Neopentasilane, and Cyclohexasilane. *Chemistry of Materials* 27 (2015) 17, pp. 6053-6058.

[79] Hertenberger, S., Rudolph, D., Bichler, M., Finley, J.J., Abstreiter, G. & Koblmüller, G. Growth kinetics in position-controlled and catalyst-free InAs nanowire arrays on Si(111) grown by selective area molecular beam epitaxy. *Journal of Applied Physics* 108 (2010) 11, pp. 114316.

[80] Heiss, M., Russo-Averchi, E., Dalmau-Mallorquí, A., Tütüncüoğlu, G., Matteini, F., Ruffer, D., Conesa-Boj, S., Demichel, O., Alarcon-Lladó, E. & Fontcuberta i Morral, A. III-V nanowire arrays: growth and light interaction. *Nanotechnology* 25 (2014) 1, pp. 014015.

[81] Hakkarainen, T. Site-Controlled Epitaxy and Fundamental Properties of InAs Quantum Dot Chains. Doctoral dissertation. 2014. Tampere University of Technology, Faculty of Natural Sciences, Optoelectronics Research Centre.

[82] Matteini, F., Tütüncüoğlu, G., Ruffer, D., Alarcón-Lladó, E. & Fontcuberta i Morral, A. Ga-assisted growth of GaAs nanowires on silicon, comparison of surface SiO_x of different nature. *Journal of Crystal Growth* 404 (2014) pp. 246-255.

[83] Giang, L.T.T., Bougerol, C., Mariette, H. & Songmuang, R. Intrinsic limits governing MBE growth of Ga-assisted GaAs nanowires on Si(111). *Journal of Crystal Growth* 364 (2013) pp. 118-122.

[84] Munshi, A.M., Dheeraj, D.L., Fauske, V.T., Kim, D.C., Huh, J., Reinertsen, J.F., Ahtapodov, L., Lee, K.D., Heidari, B., van Helvoort, A. T. J., Fimland, B.O. & Weman, H. Position-Controlled Uniform GaAs Nanowires on Silicon using Nanoimprint Lithography. *Nano Letters* 14 (2014) 2, pp. 960-966.

[85] Mandl, B., Stangl, J., Hilner, E., Zakharov, A.A., Hillerich, K., Dey, A.W., Samuelson, L., Bauer, G., Deppert, K. & Mikkelsen, A. Growth Mechanism of Self-Catalyzed Group III-V Nanowires. *Nano Letters* 10 (2010) 11, pp. 4443-4449.

[86] Rudolph, D., Schweickert, L., Morkötter, S., Loitsch, B., Hertenberger, S., Becker, J., Bichler, M., Abstreiter, G., Finley, J.J. & Koblmüller, G. Effect of interwire separation on growth kinetics and properties of site-selective GaAs nanowires. *Applied Physics Letters* 105 (2014) 3, pp. 033111.

[87] Mandl, B., Dey, A.W., Stangl, J., Cantoro, M., Wernersson, L., Bauer, G., Samuelson, L., Deppert, K. & Thelander, C. Self-seeded, position-controlled InAs nanowire

growth on Si: A growth parameter study. *Journal of Crystal Growth* 334 (2011) 1, pp. 51-56.

[88] Plissard, S., Dick, K.A., Larrieu Guilhem, Godey Sylvie, Addad Ahmed, Wallart, X. & Caroff Philippe Gold-free growth of GaAs nanowires on silicon: arrays and polytypism. *Nanotechnology* 21 (2010) 38, pp. 385602.

[89] Ma, Y., Guo, X., Wu, X., Dai, L. & Tong, L. Semiconductor nanowire lasers. *Advances in Optics and Photonics* 5 (2013) 3, pp. 216-273.

[90] Björk, M.T., Ohlsson, B.J., Sass, T., Persson, A.I., Thelander, C., Magnusson, M.H., Deppert, K., Wallenberg, L.R. & Samuelson, L. One-dimensional Steeplechase for Electrons Realized. *Nano Letters* 2 (2002) 2, pp. 87-89.

[91] Krogstrup, P., Jorgensen, H.I., Heiss, M., Demichel, O., Holm, J.V., Aagesen, M., Nygard, J. & Fontcuberta, i.M. Single-nanowire solar cells beyond the Shockley-Queisser limit. *Nat Photon* 7 (2013) 4, pp. 306-310.

[92] Rudolph, D., Funk, S., Döblinger, M., Morkötter, S., Hertemberger, S., Schweickert, L., Becker, J., Matich, S., Bichler, M., Spirkoska, D., Zardo, I., Finley, J.J., Abstreiter, G. & Koblmüller, G. Spontaneous Alloy Composition Ordering in GaAs-AlGaAs Core-Shell Nanowires. *Nano Letters* 13 (2013) 4, pp. 1522-1527.

[93] Heiss, M., Gustafsson, A., Conesa-Boj, S., Peiró, F., Morante, J.R., Abstreiter, G., Arbiol, J., Samuelson, L. & Fontcuberta i Morral, A. Catalyst-free nanowires with axial In_xGa_{1-x}As / GaAs heterostructures. *Nanotechnology* 20 (2009) 7, pp. 075603.

[94] Priante, G., Patriarche, G., Oehler, F., Glas, F. & Harmand, J. Abrupt GaP/GaAs Interfaces in Self-Catalyzed Nanowires. *Nano Letters* 15 (2015) 9, pp. 6036-6041.

[95] Müßener, J., Teubert, J., Hille, P., Schäfer, M., Schörmann, J., de, i.M., Arbiol, J. & Eickhoff, M. Probing the Internal Electric Field in GaN/AlGaN Nanowire Heterostructures. *Nano Letters* 14 (2014) 9, pp. 5118-5122.

[96] Paek, J., Yamaguchi, M. & Amano, H. MBE-VLS growth of catalyst-free III-V axial heterostructure nanowires on (1 1 1)Si substrates. *Journal of Crystal Growth* 323 (2011) 1, pp. 315-318.

[97] Ahtapodov, L., Todorovic, J., Olk, P., Mjåland, T., Slåttnes, P., Dheeraj, D.L., van Helvoort, Antonius T. J., Fimland, B. & Weman, H. A Story Told by a Single Nanowire: Optical Properties of Wurtzite GaAs. *Nano Letters* 12 (2012) 12, pp. 6090-6095.

[98] Jabeen, F., Grillo, V., Martelli, F. & Rubini, S. InGaAs/GaAs Core-Shell Nanowires Grown by Molecular Beam Epitaxy. *Selected Topics in Quantum Electronics, IEEE Journal of* 17 (2011) 4, pp. 794-800.

[99] Chen, Braidy, N., Couteau, C., Fradin, C., Weihs, G. & LaPierre, R. Multiple Quantum Well AlGaAs Nanowires. *Nano Letters* 8 (2008) 2, pp. 495-499.

- [100] Paek, J.H., Nishiwaki, T., Yamaguchi, M. & Sawaki, N. Structural and optical properties of a catalyst-free GaAs/AlGaAs core-shell nano/microwire grown on (1 1 1)Si substrate. *Physica E: Low-dimensional Systems and Nanostructures* 42 (2010) 10, pp. 2722-2726.
- [101] Jabeen, F., Rubini, S., Grillo, V., Felisari, L. & Martelli, F. Room temperature luminescent InGaAs/GaAs core-shell nanowires. *Applied Physics Letters* 93 (2008) 8, pp. 083117.
- [102] Paek, J.H., Nishiwaki, T., Yamaguchi, M. & Sawaki, N. Catalyst free MBE-VLS growth of GaAs nanowires on (111)Si substrate. *physica status solidi (c)* 6 (2009) 6, pp. 1436-1440.
- [103] Songmuang, R., Giang, L.T.T., Bleuse, J., Den Hertog, M., Niquet, Y.M., Dang, L.S. & Mariette, H. Determination of the Optimal Shell Thickness for Self-Catalyzed GaAs/AlGaAs Core-Shell Nanowires on Silicon. *Nano Letters* (2016).
- [104] Alekseev, P.A., Dunaevskiy, M.S., Ulin, V.P., Lvova, T.V., Filatov, D.O., Nezhdanov, A.V., Mashin, A.I. & Berkovits, V.L. Nitride Surface Passivation of GaAs Nanowires: Impact on Surface State Density. *Nano Letters* 15 (2015) 1, pp. 63-68.
- [105] Scolfaro, L.M.R., Pintanel, R., Gomes, V.M.S., Leite, J.R. & Chaves, A.S. Impurity levels induced by a C impurity in GaAs. *Physical Review B* 34 (1986) 10, pp. 7135-7139.
- [106] Shakfa, M.K., Wiemer, M., Ludewig, P., Jandieri, K., Volz, K., Stolz, W., Baranovskii, S.D. & Koch, M. Thermal quenching of photoluminescence in Ga(AsBi). *Journal of Applied Physics* 117 (2015) 2, pp. 025709.
- [107] Mukherjee, A., Ghosh, S., Breuer, S., Jahn, U., Geelhaar, L. & Grahn, H.T. Spatially resolved study of polarized micro-photoluminescence spectroscopy on single GaAs nanowires with mixed zincblende and wurtzite phases. *Journal of Applied Physics* 117 (2015) 5, pp. 054308.
- [108] Holm, J.V., Jørgensen, H.I., Krogstrup, P., Nygård, J., Liu, H. & Aagesen, M. Surface-passivated GaAsP single-nanowire solar cells exceeding 10% efficiency grown on silicon. *Nat Commun* 4 (2013) pp. 1498.
- [109] Larrue, A., Wilhelm, C., Vest, G., Combrié, S., De Rossi, A. & Soci, C. Monolithic integration of III-V nanowire with photonic crystal microcavity for vertical light emission. *Optics Express* 20 (2012) 7, pp. 7758-7770.
- [110] Tatebayashi, J., Kako, S., Ho, J., Ota, Y., Iwamoto, S. & Arakawa, Y. Room-temperature lasing in GaAs nanowires embedding multi-stacked InGaAs/GaAs quantum dots. *Lasers and Electro-Optics (CLEO), 2015 Conference on, 2015*, pp. 1-2.
- [111] Ruda, H.E. & Shik, A. Polarization-sensitive optical phenomena in semiconducting and metallic nanowires. *Physical Review B* 72 (2005) 11, pp. 115308.

- [112] Gale, G.W., Small, R.J. & Reinhardt, K.A. 4 - Aqueous Cleaning Surface Conditioning Processes. In: Kern, K.A.R. (ed.). Handbook of Silicon Wafer Cleaning Technology (Second Edition). Norwich, NY 2008, William Andrew Publishing. pp. 201-265.
- [113] Komeda, T., Morita, Y. & Tokumoto, H. Surface roughening and metastable superstructures on wet-processed Si(111) surface induced by hydrogen desorption. Surface Science 348 (1996)1–2, pp. 153-160.
- [114] Binnig, G., Quate, C.F. & Gerber, C. Atomic Force Microscope. Physical Review Letters 56 (1986) 9, pp. 930-933.
- [115] Dimension TM 3100 Manual. C ed. 2003, Digital Instruments Veeco Metrology Group.
- [116] Horcas, I., Fernández, R., Gómez-Rodríguez, J.M., Colchero, J., Gómez-Herrero, J. & Baro, A.M. WSXM: A software for scanning probe microscopy and a tool for nanotechnology. Review of Scientific Instruments 78 (2007) 1, pp. 013705.
- [117] Ryland, R.G., Hasegawa, S. & Williams, E.D. Silicon motion during antimony deposition on Si(111). Surface Science 345 (1996) 1–2, pp. 222-234.
- [118] Sigma TM Field Emission Scanning Electron Microscope Instruction Manual. In: Operator's user guide. 2011, Carl Zeiss NTS - Nano Technology Systems Division.
- [119] Birkholz, M. Thin film analysis by X-ray scattering. 2006, John Wiley & Sons.
- [120] PANalytical X'Pert PRO X-ray Diffraction System User's Guide. 2007, PANalytical B.V.
- [121] Bauer, G., Li, J. & Koppensteiner, E. X-ray reciprocal space mapping of Si-Si_{1-x}Ge_x heterostructures. Journal of Crystal Growth 157 (1995) 1–4, pp. 61-67.
- [122] Krogstrup, P., Hannibal Madsen, M., Hu, W., Kozu, M., Nakata, Y., Nygård, J., Takahashi, M. & Feidenhans'l, R. In-situ x-ray characterization of wurtzite formation in GaAs nanowires. Applied Physics Letters 100 (2012) 9, pp. 093103.
- [123] Schroth, P., Köhl, M., Hornung, J., Dimakis, E., Somaschini, C., Geelhaar, L., Biermanns, A., Bauer, S., Lazarev, S., Pietsch, U. & Baumbach, T. Evolution of Polytypism in GaAs Nanowires during Growth Revealed by Time-Resolved *in situ* x-ray Diffraction. Physical Review Letters 114 (2015) 5, pp. 055504.
- [124] Olmstead, M.A., Bringans, R.D., Uhrberg, R.I.G. & Bachrach, R.Z. Arsenic overlayer on Si(111): Removal of surface reconstruction. Physical Review B 34 (1986) 8, pp. 6041-6044.
- [125] Bozso, F. & Avouris, P. Adsorption of phosphorus on Si(111): Structure and chemical reactivity. Physical Review B 43 (1991) 2, pp. 1847-1850.

- [126] Somaschini, C., Bietti, S., Koguchi, N., Montalenti, F., Frigeri, C. & Sanguinetti, S. Self-assembled GaAs islands on Si by droplet epitaxy. *Applied Physics Letters* 97 (2010) 5, pp. 053101.
- [127] Chi, J.Y. & Katkov, A.V. Chapter 10 - Effect of antimony coverage on InAs/GaAs (001) heteroepitaxy. In: Henini, M. (ed.). *Molecular Beam Epitaxy*. Oxford 2013, Elsevier. pp. 189-202.
- [128] Heyn, C., Stemmann, A., Schramm, A., Welsch, H., Hansen, W. & Nemcsics, Á. Faceting during GaAs quantum dot self-assembly by droplet epitaxy. *Applied Physics Letters* 90 (2007) 20, pp. 203105.
- [129] Yu, I., Chang, C., Yang, C., Lin, C., Ma, Y. & Chen, C. Characterization and density control of GaN nanodots on Si (111) by droplet epitaxy using plasma-assisted molecular beam epitaxy. *Nanoscale Research Letters* 9 (2014) 1, pp. 1-6.
- [130] Cheiwchanchamnangij, T. & Lambrecht, W.R.L. Band structure parameters of wurtzite and zinc-blende GaAs under strain in the GW approximation. *Physical Review B* 84 (2011) 3, pp. 035203.
- [131] Strauch, D. GaAs: lattice parameters. In: Rössler, U. (ed.). 2011, Springer Berlin Heidelberg. pp. 169-172.
- [132] Cui Hong-Ling, Chen Xiang-Rong, Ji Guang-Fu & Wei Dong Structures and Phase Transition of GaAs under Pressure. *Chinese Physics Letters* 25 (2008) 6, pp. 2169.
- [133] Hocevar, M., Thanh Giang, L.T., Songmuang, R., den Hertog, M., Besombes, L., Bleuse, J., Niquet, Y. & Pelekanos, N.T. Residual strain and piezoelectric effects in passivated GaAs/AlGaAs core-shell nanowires. *Applied Physics Letters* 102 (2013) 19, pp. 191103.
- [134] Akimoto, K., Kamada, M., Taira, K., Arai, M. & Watanabe, N. Photoluminescence killer center in AlGaAs grown by molecular-beam epitaxy. *Journal of Applied Physics* 59 (1986) 8, pp. 2833-2836.
- [135] Graham, A.M., Corfdir, P., Heiss, M., Conesa-Boj, S., Uccelli, E., Fontcuberta, i.M. & Phillips, R.T. Exciton localization mechanisms in wurtzite/zinc-blende GaAs nanowires. *Physical Review B* 87 (2013) 12, pp. 125304.
- [136] Keck, P.H. & Broder, J. The Solubility of Silicon and Germanium in Gallium and Indium. *Physical Review* 90 (1953) 4, pp. 521-522.
- [137] van, d.V., Hartmann, W.J.A.M. & Giling, L.J. Photoluminescence studies of defects and impurities in annealed GaAs. *Journal of Applied Physics* 60 (1986) 10, pp. 3735.
- [138] Röder, R., Sidiropoulos, T.P.H., Buschlinger, R., Riediger, M., Peschel, U., Oulton, R.F. & Ronning, C. Mode Switching and Filtering in Nanowire Lasers. *Nano Letters* 16 (2016) 4, pp. 2878-2884.

[139] Hilse, M., Ramsteiner, M., Breuer, S., Geelhaar, L. & Riechert, H. Incorporation of the dopants Si and Be into GaAs nanowires. *Applied Physics Letters* 96 (2010) 19, pp. 193104.